UNIVERSITÄT
BERN

Graduate School for Cellular and Biomedical Sciences

University of Bern

The spiral shape of the cochlea

Transverse flow visualizations and emerging phenomena in idealized models

PhD Thesis submitted by

Noëlle Claudia Harte

for the degree of

PhD in Biomedical Engineering

Supervisors

Prof. Dr. Wilhelm Wimmer
Department of Otorhinolaryngology,
TUM School of Medicine, Klinikum rechts der Isar,
Technical University of Munich

Prof. Dr. Dominik Obrist
ARTORG Center for Biomedical Engineering Research
Faculty of Medicine of the University of Bern

Co-advisor

Prof. Dr. Marco Domenico Caversaccio
Department of Otolaryngology, Head and Neck Surgery, Inselspital
Faculty of Medicine of the University of Bern

Accepted by the Faculty of Medicine, the Faculty of Science and the Vetsuisse Faculty of the University of Bern at the request of the Graduate School for Cellular and Biomedical Sciences

Bern, Dean of the Faculty of Medicine

Bern, Dean of the Faculty of Science

Bern, Dean of the Vetsuisse Faculty Bern

"*But I've never seen the Icarus story as a lesson about the limitations of humans. I see it as a lesson about the limitations of wax as an adhesive.*"

Randall Munroe

ACKNOWLEDGMENTS

This Ph.D. thesis covers parts of the work carried out during the last (nearly) four years in the Hearing Research Laboratory at the ARTORG Center for Biomedical Engineering Research in collaboration with the Inselspital in Bern and the University of Twente in Enschede. I was very fortunate to have great supervisors and brilliant minds involved in my project, without whom the presented work would not have been possible.

My exceptional thanks go to Prof. Dr. Wilhelm Wimmer, first of all, for entrusting me with this intriguing project and giving me the opportunity to collaborate with researchers from various fields and places. Thank you for all the motivating (and also entertaining) discussions and your creative ideas, which not seldom came from a completely new perspective. And last but not least, thank you for your understanding of my lack of presence on windy and stormy days. Prof. Dr. Dominik Obrist's invaluable contribution from the fluid mechanics side was particularly meaningful to me. Thank you for explaining the complex phenomena in simple terms and, not less, also for making me aware of the fluid dynamics surrounding us. And finally, thank you for introducing me to your team and inviting me to the group events, from which many unforgettable memories remain. My sincere thanks also go to the members of my Ph.D. expert committee: I am grateful to Prof. Dr. med. Marco Caversaccio for co-advising this project. I appreciate all his inputs, ideas and advice, which were a precious contribution. I would like to thank Prof. Dr. Mauricio Reyes for mentoring the Ph.D. project over the last four years and my external co-referee, Prof. Dr. Tobias Reichenbach, for examining my work. I am very grateful for his expert feedback and valuable suggestions.

From our collaborators at UT, my special thanks go to Asst. Prof. Dr. Guillaume Pierre René Lajoinie, without whom the experimental part would not have been feasible. Thank you for finding simple solutions to all my challenging problems. I learned a lot from you during the (fast-paced) lab life. Thank you not only for sharing your knowledge, but also for being a wonderful host! Along with Guillaume, I would also like to thank Prof. Dr. Michel Versluis for welcoming me as a guest student at UT and for his continuous support and interest in the project. Many thanks also to the people from the POF team that I had the pleasure of meeting during my short stays. Besides helping me out in the lab, they also made me feel at home abroad. I remember the eventful time with pleasure.

Many thanks also to the colleagues from ARTORG and Inselspital. I am very grateful for the inputs and ideas from the clinical side from Prof. Dr. med. Georgios Mantokoudis, Dr. med. Miranda Morrison, Prof. Dr. med. Stefan Weder, Prof. Dr. med. Lukas Anschütz, and Dr. med. Athanasia Korda. Many thanks also to the CVE group, who helped out with my (sometimes very urgent) questions. Thank you also for the great memories from outside the office. And of course, I would like to thank the wonderful (present and former) hearing lab team for making this journey as enjoyable as it was, for the many discussions, and the delightful rooftop beers. Thank you, Aleksandra, Alexandra, András, Benjamin,

Christoph, David, Diana, Emile, Esther, Filip, Julian, Klaus, Luca, Nathalie, Nino, Philipp, Pia, Raphael, Stefan, Suyi, Tim, Tobias, Tom! On this occasion, I would also like to specially thank Dr. Philipp Aebischer for his time and effort in proofreading this thesis and for his helpful suggestions, as well as David Sprecher, whose professional experience and thorough approach were of great importance to the measurement success.

Special thanks go to my friends for enriching my life outside of work. In particular, thanks to Ellen, Sebastian, and Tobias for unforgettable sunset sessions on the water. Finally, I would like to express my deep gratitude to my family. I would like to thank my parents, Alexander and Isabelle, for their unwavering support, be it studies, music or windsurfing. Furthermore, I thank my sister Corinne, my brother Thierry and my grandmother Marietta for always being there for me. Last but most important: Thank you, Janos, for being by my side throughout this Ph.D., your moral support, and invaluable love.

ABSTRACT

The cochlea, our auditory organ, has a unique spiral shape and is fluid-filled. The physiological role of its shape remains, to a great extent, elusive and is the subject of ongoing research and debate. The curvature and torsion of the cochlear duct are most pronounced toward the apex, and therefore the low frequencies processed there are particularly interesting. Flow in the radial direction in the cochlea, i.e., transverse flow, is of relevance because of the cochlea's microanatomy. This thesis aims to investigate the interplay between geometry and fluid flow, especially transverse flows, using numerical and experimental methods.

In the first part, computational fluid dynamics (CFD) simulations are performed in helical square ducts with curvature and torsion, similar to the ones observed in human cochleae. Transverse flows are examined under a harmonically oscillating axial flow for frequencies covering infrasound and low-frequency hearing, with a mean inlet velocity amplitude representing sound pressure levels from normal conversation up to the threshold of pain. Torsion significantly increases transverse flow, especially when the influence of curvature drops to negligible amounts. Interestingly, the combined effect of curvature and torsion is larger than expected from a superposition of the two.

The cochlea's thin membranes, some as little as two cell layers thick, make the study of shear stresses, which are exerted by the fluid on the walls, interesting. Subsequently, the effect of geometry on wall shear stresses and pressure fluctuations is examined numerically. The helical shape experiences the most pronounced wall shear stresses at the inner wall of the curve, and its maximal transverse wall shear stresses are higher than the sum of the ones in toroidal and twisted ducts.

The second part addresses the visualization of transverse flows in millimetric ducts using an in-house developed scanning particle image velocimetry (PIV) system to capture the full flow field in a volume. Our system is adapted to small-scale oscillatory flows and allows for precise measurements of both time-resolved and net velocities. The experimental outcomes align well with the CFD simulations. The developed PIV system offers means for studying multi-scale periodic flows in micro- to millimeter-scale models across a variety of applications, including biological systems like the inner ear.

The observed transverse flow phenomena offer new insights into cochlear fluid dynamics, with potential implications for metabolite transport. Further research is needed to elucidate their impact on cochlear mechanics.

CONTENTS

Abstract **ix**

1 Introduction **1**
1.1 Motivation . . . 2
1.2 Anatomy and physiology of the human ear . . . 4
1.3 Cochlear modeling . . . 11
1.4 Effects of geometry on fluid flow at low Reynolds numbers . . . 15
1.5 Thesis objectives and overview . . . 24

2 Transverse flow under oscillating stimulation in helical square ducts with cochlea-like geometrical curvature and torsion **25**
Submitted as: Harte N.C., Obrist D., Caversaccio M.D., Lajoinie G.P.R. and Wimmer W. Transverse flow under oscillating stimulation in helical square ducts with cochlea-like geometrical curvature and torsion.
2.1 Abstract . . . 26
2.2 Introduction . . . 27
2.3 Methods . . . 28
2.4 Results . . . 32
2.5 Discussion . . . 38
2.6 Acknowledgements . . . 39
2.7 Supplement . . . 40

3 Wall shear stress and pressure fluctuations under oscillating stimulation in helical square ducts with cochlea-like geometrical curvature and torsion **45**
Published in: Harte N.C., Obrist D., Caversaccio M.D., Lajoinie G.P.R. and Wimmer W. Wall shear stress and pressure fluctuations under oscillating stimulation in helical square ducts with cochlea-like geometrical curvature and torsion. *IEEE Engineering in Medicine and Biology Society* 2023;
3.1 Abstract . . . 46
3.2 Introduction . . . 47
3.3 Methods . . . 47
3.4 Results . . . 48
3.5 Discussion . . . 52

4 Second order and transverse flow visualization through 3D PIV in complex millimetric ducts **55**
To be submitted as: Harte N.C., Obrist D., Versluis M., Groot Jebbink E., Caversaccio M.D., Wimmer W. and Lajoinie G.P.R. Second order and transverse flow visualization through 3D PIV in complex millimetric ducts.
4.1 Abstract . . . 56
4.2 Introduction . . . 57
4.3 Material and methods . . . 59

4.4 Results . . . 67
4.5 Discussion . . . 77
4.6 Conclusion . . . 79
4.7 Acknowledgement . . . 79
4.8 Appendix . . . 80

5 Conclusions and outlook **85**
5.1 CFD visualizations and wall shear stresses . . . 86
5.2 3D-PIV visualizations and complex cross-sections . . . 87
5.3 Potential physiological implications . . . 88
5.4 Outlook and future work . . . 89
5.5 Summary . . . 90

List of tables **91**

List of figures **93**

References **95**

List of publications **105**

Declaration of originality **107**

ACRONYMS

2D two-dimensional

3D three-dimensional

3D3C three-dimensional three-component

ABS acrylonitrile-butadiene-styrene

AWSS axial wall shear stress

CFD computational fluid dynamics

PDMS polydimethylsiloxane

PET polyethylen terephthalat

PIV particle image velocimetry

PTV particle tracking velocimetry

SNR signal-to-noise ratio

SPL sound pressure level

TWSS transverse wall shear stress

WHO World Health Organization

CHAPTER 1

INTRODUCTION

A brief introduction on the anatomy and physiology of the human ear is given. This is followed by an overview of cochlear modeling, with special emphasis on the effect of the cochlea's spiral geometry on flow processes. Next, the effect of geometry on transverse and axial flows is discussed and the state of the art on methods to visualize them is reviewed. Particle image velocimetry, a technique for deriving flow velocities in experimental setups, is then described. The introduction concludes with the objectives and an overview of the thesis.

1.1 Motivation

According to the World Health Organization (WHO), more than five percent of the world's population — 430 million people worldwide — live with a hearing impairment [1]. This reduces their quality of life as it affects safety, communication, access to information and leisure activities. If the hearing loss is unaddressed, it can lead to exclusion from education and to unemployment. The WHO estimates that unaddressed hearing loss causes costs equivalent to 870 billion Swiss Francs every year [1]. Especially in today's world, hearing is an important topic as we are increasingly exposed to auditory stimuli like city noise, noise in public transportation (planes, cars), and technology related sounds. The WHO [1] estimates that by 2050 nearly twice as many — 700 million people — will have disabling hearing loss[1]. The frequency of hearing loss increases with age, with over one in four people over 60 experiencing disabling hearing loss [1]. As life expectancy increases in many countries, age-related hearing loss is a major contributor to this upward trend, in addition to other factors such as noise-induced hearing loss, the use of ototoxic medication, and viral infections [2, 3].

Treatment for age-related hearing loss often involves the use of hearing aids or, in more severe cases, middle ear implants or cochlear implants, in which an electrode is inserted into a fluid-filled cochlea. Such devices directly influence or alter the cochlear mechanics. Improved understanding of the flow phenomena in the cochlea can thus lead to better hearing aid technology and design. Fluid simulations in models of the cochlea can further enhance our understanding of cochlear mechanics.

While there is no net flow in the cochlea, studies, using computational fluid dynamics simulations, showed that there are steady streaming effects [4, 5]. Steady streaming in the axial direction, along the cochlear scalae, could be interesting for drug delivery, as the two major entry points for drugs into the inner ear are at the base of the cochlea [6]. Commonly applied drugs to the inner ear include cortisone (glucocorticoid) against acute hearing loss and ototoxic antibiotics (gentamicin) to treat Ménière's disease [7, 8]. The latter treats vertigo (caused by Ménière's disease) by targeting the vestibular hair cells causing it [9]. Radial streaming effects may facilitate metabolite transport within the cochlea.

Since its descriptions by Bartholomeus Eustachius and Gabriele Fallopius in the 16th century, we know that the cochlea is spiral-shaped in humans [11]. Surprisingly, however, it is still partly unknown why it takes on this particular shape. In birds and reptiles the sensory hearing organ is formed by a slightly bent or twisted duct, it does not wind around a central axis as in marsupials and placental mammals (Fig. 1.1) [10, 12–14]. The complex evolution of the auditory organs underscores the importance of hearing for survival [10]. It seems that during evolution, the cochlear duct length as well as its coiling increased [15]. For example, monotremes like the platypus and echidna indigenous to Australia and New Guinea have a coiled apex of the membranous cochlear duct but an uncoiled bony cochlear canal [16]. Jurassic mammals already had the beginning of coiling (three-quarters of a complete turn) [16]. As shown in Fig. 1.2, a fully coiled cochlea is, however, only found in humans and all other therian mammals (i.e., placental mammals and marsupials) [12].

[1] 'Disabling' hearing loss refers to hearing loss greater than 35 decibels in the better hearing ear [1].

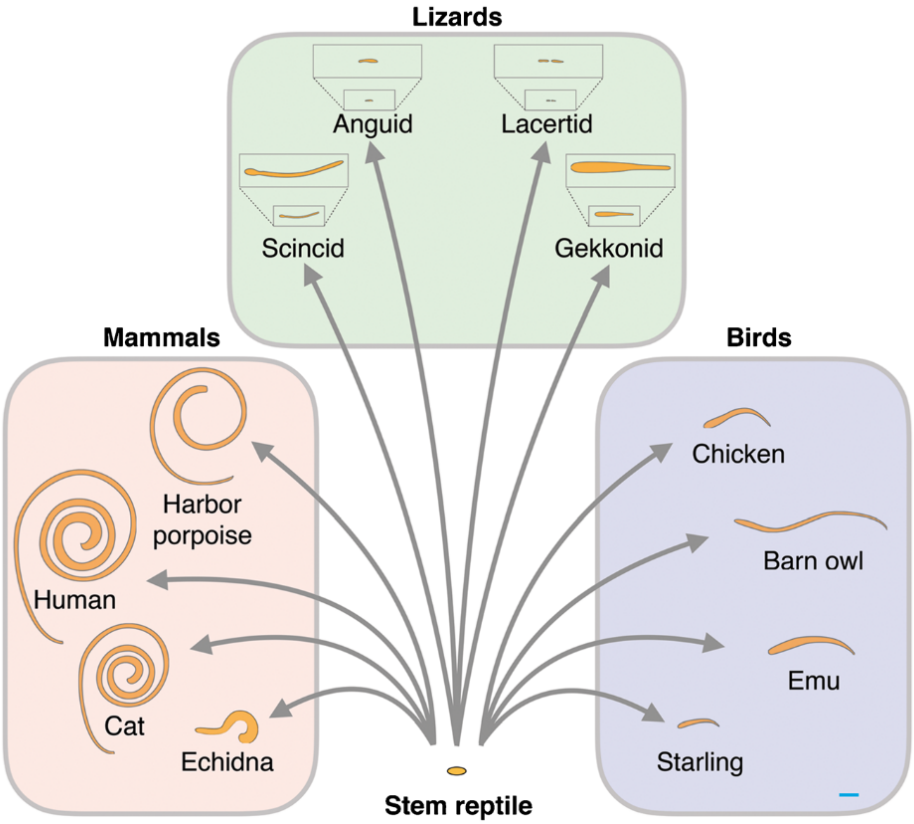

Fig. 1.1. Phylogenetic radiation of the form of the auditory papilla in amniote vertebrates (the scale bar on the bottom right is 1 mm). *Not included in the Creative Commons Attribution 4.0 International License. Reprinted with permission from the publisher Springer Nature [10].*

While there are some obvious benefits of coiling such as the efficient packing of the cochlear duct within the petrous bone [17] and access for nerves and blood vessels via the modiolus, the effects of coiling, in particular on fluid mechanics and related physiological phenomena are not yet fully understood [15]. The hearing range of coiled cochleae is extended to frequencies that are higher and lower compared to uncoiled cochleae [18–20]. The broad frequency range of coiled cochleas cannot be explained by their longer cochlear duct alone [21]. This leads to controversial discussions on whether the physiological advantages could arise from the coiled cochlear morphology. So far, the literature is inconclusive.

Therefore, this work aims to investigate the effect of geometrical features, in particular curvature and torsion, on fluid mechanics. To this end, computational fluid dynamics (CFD) simulations were performed to understand fundamental properties under oscillatory stimulation (transverse flow induced by geometry). Then, secondary flow phenomena were investigated (i.e., transverse wall shear stress, Lagrangian streaming). Finally, for validation, an experimental method was developed that is suitable for real scale measurements in in-vitro models of cochlear size.

The following sections provide background on human hearing, with an emphasis on corresponding fluid phenomena. The effect of geometry on fluid motion is discussed in the

context of cochlear modeling but also more generally on flow in helical ducts. With this information, the reader can put the chapters presented in this thesis into context.

1.2 Anatomy and physiology of the human ear

The ear is a complex and highly organized organ that enables us to detect and experience sounds waves and to maintain our balance. It has a remarkable precision regarding both the range in frequency (approximately ten octaves) and in sound pressure level (approximately 120 dB, or a factor of 1'000'000 between the softest and loudest sounds[2] [22]). Frequencies between 20-20'000 Hz are commonly considered in the human hearing range, but the limit is not strict and hearing at 10 Hz and less has been reported for high enough sound pressure levels [23]. The ear consists of three main parts which can be categorized based on their function in the hearing process: the outer, middle and inner ear.

Air conduction and bone conduction are the two main pathways for hearing. Air conduction denotes hearing based on sound waves that enter through the ear canal and are

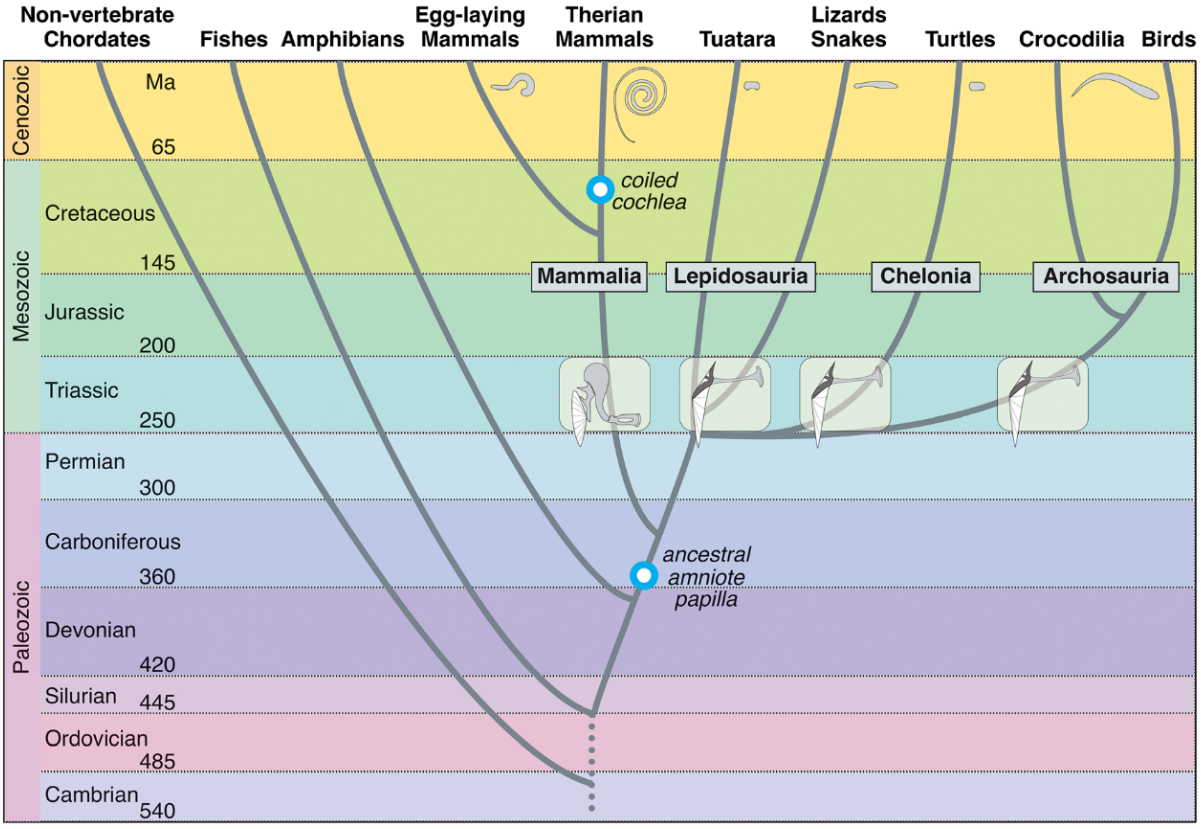

Fig. 1.2. Amniote phylogenetic tree over 500 million years to illustrate the approximate time of origin of particular features of auditory systems. *Not included in the Creative Commons Attribution 4.0 International License. Reprinted with permission from the publisher Springer Nature [10].*

[2]that it can capture without permanent damage

transmitted via the ossicles to the inner ear. Bone conduction is the pathway through vibrations of the skull bone to the inner ear via separate mechanisms [26]: through inertial forces on the ossicles and the inner ear fluids; through movements of the tissue surrounding the ear canal; through the compression and expansion of the cochlear space; and through sound pressure transmission from the skull interior. These mechanisms result in a similar basilar membrane motion as air conduction [26, 27]. We will focus on air conduction in the following (Fig. 1.3), as it is expected to be dominant in normal hearing subjects [28, 29].

Outer and middle ear

The outer ear consists of the pinna and the ear canal. It is the only part of our ear that is visible from outside. The pinna collects and directs sound pressure waves from the environment into the ear canal and to the tympanic membrane, i.e., the eardrum. The eardrum separates the outer from the middle ear. Behind the eardrum is an air-filled cavity

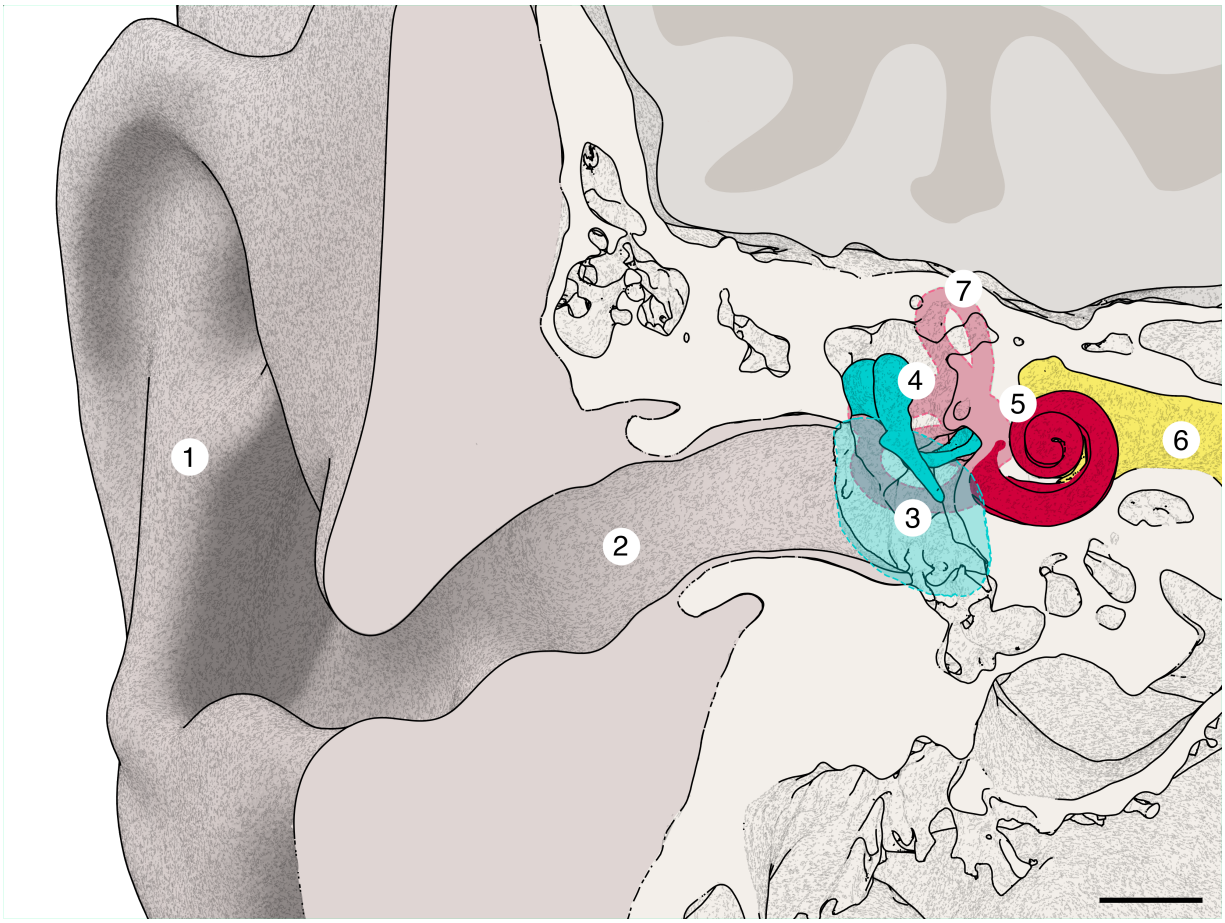

Fig. 1.3. Coronal section through a right ear. Sounds arriving at the pinna (1) are reflected into the ear canal (2), move the tympanic membrane (3), are passed by the ossicles (4) to the cochlea (5), from where nerve impulses travel along the cochlear nerve (6) to the brain. The vestibular system (7) is sensitive to motion and inertia-induced fluid movement. The scale bar measures 5 mm. *Image rendered from CT data [24]. Adapted and reprinted with permission from the author [25].*

that contains the three ossicles (Fig. 1.4): the malleus (hammer), incus (anvil), and stapes (stirrup), which is the smallest bone in the human body. They are arranged in a chain and the malleus connects to the eardrum, while the stapes borders the inner ear at the oval window. Sound pressure waves move the eardrum, and the ossicles efficiently transmit and amplify the vibrations from the eardrum to the inner ear.

The major function of the middle ear is to overcome the higher acoustic impedance of the fluid-filled inner ear compared to the air-filled outer ear [30]. The impedance mismatch at an air-water interface would usually lead to reflection of almost all pressure waves [31]. In the middle ear, the reflection is reduced in part by the lever action of the ossicles and by the reduction of the area on which the force is concentrated, from the tympanic membrane (around 60 mm^2 [32]) to the oval window (around 3 mm^2 [33]). The sound transfer through the middle ear is characterized by a frequency-dependent function, the middle ear transfer function.

Middle ear transfer function

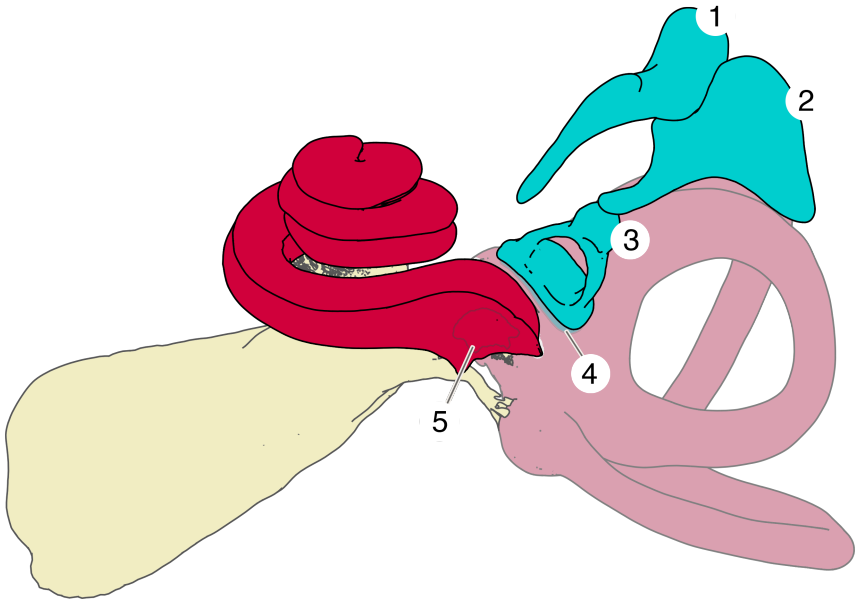

Fig. 1.4. Left inner ear with the three ossicles: malleus (1), incus (2), and stapes (3). The oval window (4) and the round window (5) are sealed by two elastic membranes that allow for fluid motion inside the cochlea. *Image rendered from micro computed tomography data [24, 34]. Adapted and reprinted with permission from the author [25].*

The middle ear transfer function can be defined as the ratio of the sound pressure at the tympanic membrane (the ear canal sound pressure) and the sound pressure in the cochlea [35]. The sound pressure level in the ear canal is typically given in relation to the sound pressure in air of 20 μPa. For example, 1 Pa ear canal sound pressure can be considered equivalent to 94 dB sound pressure level (SPL). The middle ear transfer function

is usually either modeled with finite elements [36–39] or measured with, e.g., a laser Doppler vibrometer using temporal bone specimens [35, 40–43]. As sound pressure measurements in the cochlea are challenging, the velocity or displacement of the stapes are often used instead [35]. The transfer function with respect to the stapes *velocity* reaches its resonance at about 1 kHz, with a mean slope of approximately 6 dB per octave up to 1 kHz (and decreases with approximately -6 dB above 1 kHz) [35, 42].

Measuring the stapes velocity is complex because of the three-dimensional (3D) vibration modes of its footplate: angular motion (rocking, tilting) and translational motion (piston-like) [43, 44]. At low frequencies, the piston-like motion is dominant, while the rocking stapes motion gains importance for higher frequencies (above 4 kHz) [43]. Moreover, Edom et al. [45] showed that the piston-like movement evokes higher basilar membrane amplitudes than the rocking motion, especially at low frequencies. We therefore assumed a piston-like, translational motion for the boundary condition in our simulations, because we focus on low frequencies.

The following provides figures for the displacement of the eardrum, the velocity of the stapes, and the intracochlear pressure. For a sound pressure level (SPL) of 80 dB in the auditory ear canal, the displacement of the eardrum (at the umbo, which is the most depressed part of the conical-shaped eardrum) is about 20 nm at 600 Hz, and higher than the one of the stapes (of about 11 nm) [43]. For frequencies above 6 kHz the umbo displacement falls below 1 nm [43].

Between the thresholds of hearing and pain, the stapes velocity ranges from nanometers to micrometers per second. At 512 Hz, 94 dB SPL corresponds to a velocity of approximately 100 μm/s (piston-like stapes motion) [44]. A reduction of 20 dB SPL leads to an approximately ten times smaller velocity. Below 1000 Hz, decreasing frequencies correspond to increasing equivalent sound pressure levels for the same stapes velocity. For example, at 32 Hz, a stapes velocity of 200 μm/s can be expected for an ear canal pressure of approximately 125 dB SPL [40]. At 256 Hz, the same stapes velocity corresponds to an acoustic stimulus with roughly 107 dB SPL.

At 512 Hz, 94 dB SPL corresponds approximately to a scala vestibuli pressure amplitude of 5 Pa, and a scala tympani pressure of 2 Pa, which were measured at a distance of 100 μm from the round and oval windows into the cochlea [40].

Inner ear

Despite its small size, the inner ear plays a central role in the auditory process. It is a cavity which is enclosed in and protected by the densest bone in the human body, the petrous — Latin for "stone-like" — part of the temporal bone. It consists of the bony labyrinth and a membranous labyrinth which is situated within the bony labyrinth.

Functionally, the inner ear can be divided into two structures: the cochlea, which is responsible for hearing, and the vestibular system, which provides balance and spatial orientation. Depending on the frequency of incoming pressure waves, the processing occurs in one of these structures [46]. Frequencies above 20 Hz are considered in the human hearing range, while slower motions are processed by the vestibular system (hair cells in the semicircular canals are not stimulated by frequencies above 15 Hz because of viscous blocking [46]). In the following, we will focus on the cochlea.

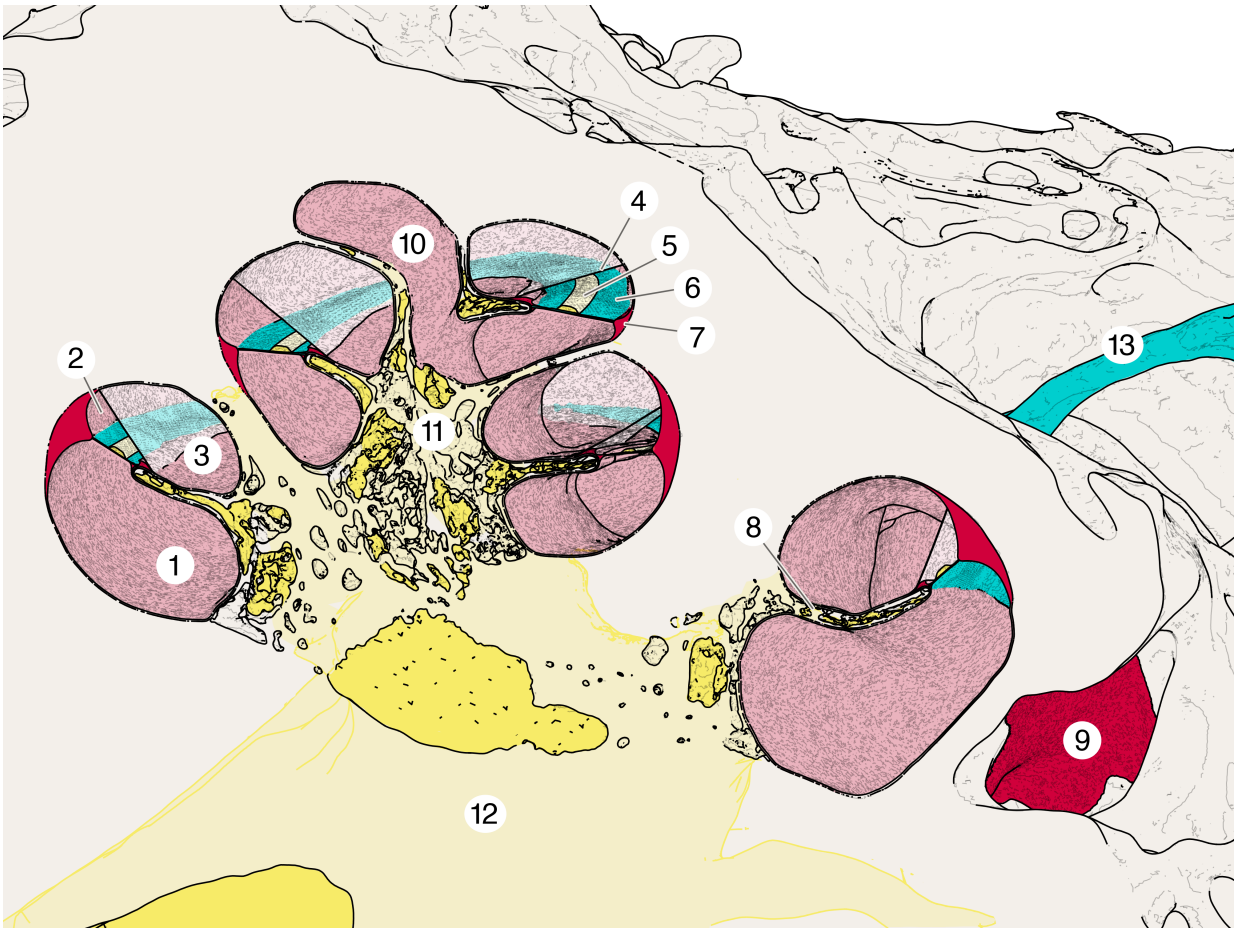

Fig. 1.5. Axial section through a left cochlea. Scala tympani (1), scala media (2), scala vestibuli (3), Reissner's membrane (4), organ of Corti (5), basilar membrane (6), spiral ligament with the stria vascularis (7), osseous spiral lamina (8), round window membrane (9), helicotrema (10), modiolus (11), cochlear nerve (12), and stapes (13). *Image rendered from micro computed tomography data [34]. Reprinted with permission from the author [25].*

The cochlea — named after its spiral shape — contains three fluid-filled chambers: the scala vestibuli, the scala tympani and the scala media (Fig. 1.5). These chambers coil conically around the modiolus, the central axis of the cochlea, spanning approximately 2.4 to 2.8 turns [47, 48]. The overall length of the (uncoiled) cochlear duct, i.e., the scala media, measures approximately 36 mm [49]. The scala media contains endolymph and houses sensory hair cells for hearing in the organ of Corti (Fig. 1.6). The scala vestibuli and scala tympani are filled with perilymph and connected at the apex of the cochlea, the helicotrema. Both fluids exhibit mechanical properties similar to water at body temperature [50]. Fig. 1.4 shows the oval and the round window, two openings in the bony labyrinth, which are sealed by elastic membranes. While the oval window opens into the scala vestibuli, the scala tympani is enclosed by the round window at the base. The scalae are separated by two elastic partitions: the Reissner's membrane, composed of only two layers of cells [51], and the more solid basilar membrane. Towards the modiolus, the basilar membrane is attached to the osseous spiral lamina, and it separates the scala media from the scala tympani. The Reissner's membrane separates the scala vestibuli from the scala media.

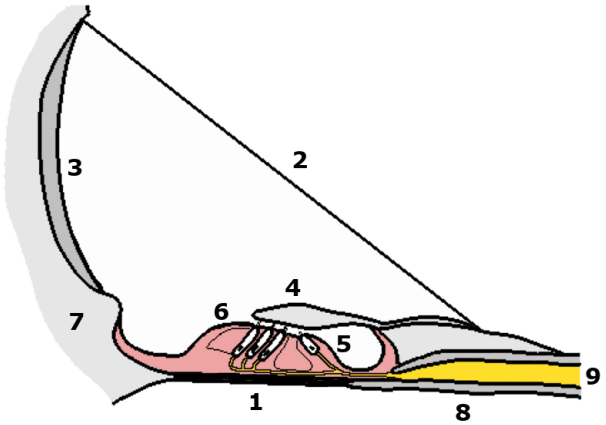

Fig. 1.6. Cross-section of the scala media and the organ of Corti (shaded red). Basilar membrane (1), Reissner's membrane (2), stria vascularis (3), tectorial membrane (4), inner hair cell (5), outer hair cells (6), spiral ligament (7), osseous spiral lamina (8), spiral ganglion fibers (9). *Figure based on histological image. Reprinted with permission from the author [52].*

When sound enters, the stapes vibrates at the oval window, which is in contact with the perilymph within the scala vestibuli, causing the fluid in the cochlea to oscillate. The round window at the base of the scala tympani can bulge in response to the increased fluid pressure from the stapes movement (Fig. 1.4). The differences in fluid pressure cause a wave (traveling wave [53]) on the basilar membrane that travels along its length, from the cochlear base to the helicotrema [54]. The traveling wave peaks at a resonance point, the characteristic place whose position depends on the sound frequency. There, the axial wave motion is transformed into a transverse basilar membrane motion [46, 55]. Thus, the organ of Corti, which rests on top of the basilar membrane and runs along its entire length, is moved the most at this location. Fig. 1.6 shows the organ of Corti with one row of inner hair cells and three rows of outer hair cells. Outer hair cells are connected to the tectorial membrane, while the stereocilia of inner hair cells stand free. Inner hair cells are considered the primary sensory tissue [46, 56]. A shearing motion between the tectorial membrane and the basilar membrane deflects outer hair cell stereocilia. and creates a shear flow. Outer hair cells actively amplify the response to sound waves by changing their length [57–60]. The stereocilia of inner hair cells are thought to be deflected by fluid flow [56, 61]. Interestingly, inner hair cells have high resistance to cross flow, while the resistance of the outer hair cells is much lower and depends on the flow direction [61]. Through mechanical and voltage-gated ion channels, a receptor potential is formed in the inner hair cells. This generates an action potential in the spiral ganglion cells which is transmitted to the auditory cortex of the brain. The brain then processes and interprets these signals, allowing us to perceive and understand the sounds we hear.

The properties of the basilar membrane change along its length and determine the characteristic place of resonance for different frequencies. At the base, the membrane has a dense core with high stiffness but in the apical turn it only consists of a thin layer of cells (which reduces the stiffness) [62]. Furthermore, its width increases towards the apex. Therefore, low frequencies are processed at the apical turn of the cochlea, while higher frequencies are processed closer to the base, which is referred to as tonotopy. Fig. 1.7

shows the tonotopic organization of the cochlea, which was already suggested by Hermann van Helmholtz in the 19th century [11]. Warren et al. [62] experimentally investigated the basilar membrane motion at the apex of Guinea pig cochleae, where low frequencies are perceived. Notably, they found that its behavior at the apex was different from the one at the base. The motion amplitude showed a nearly exponential decay with the radial distance [62].

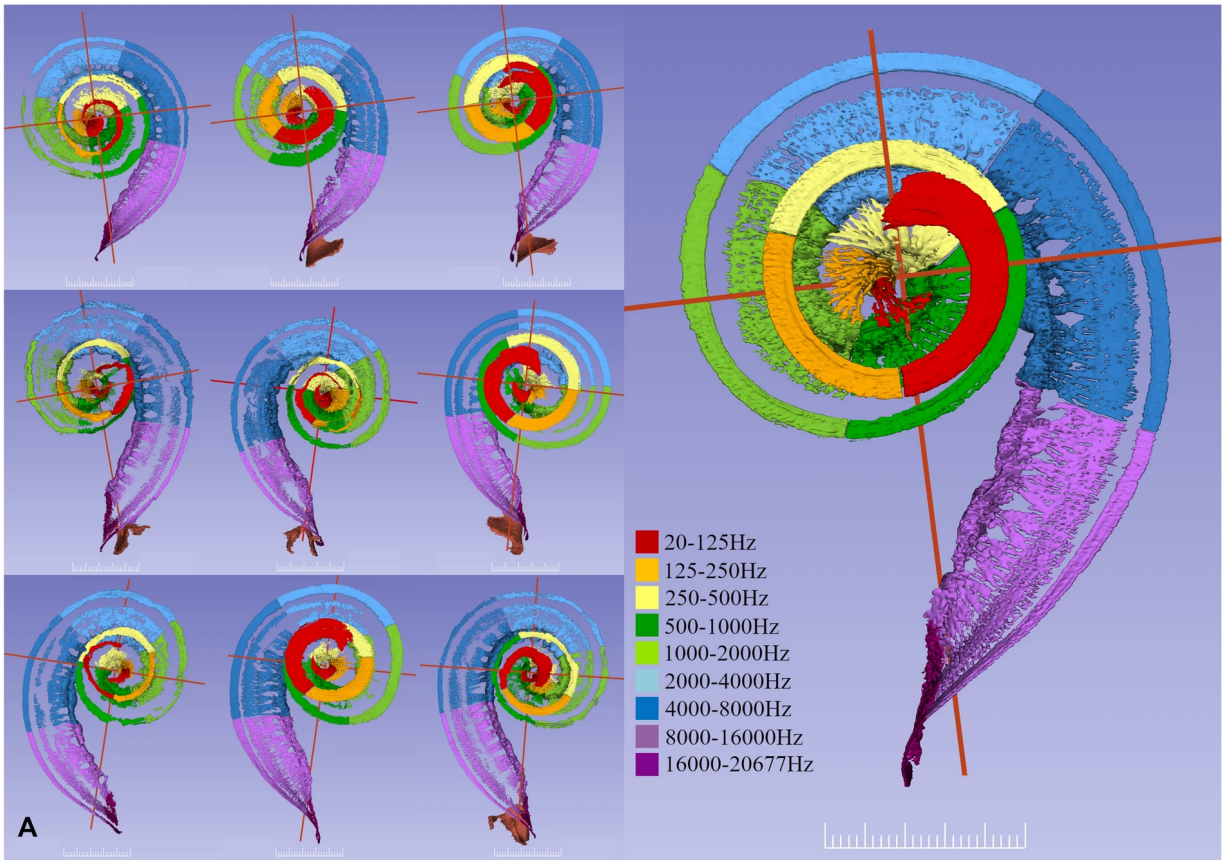

Fig. 1.7. Segmentations of soft tissues from ten cochleae shown in orthographic 3D view. Frequency maps of the basilar membrane were developed according to Greenwood [63]. Corresponding dendrites were traced to the spiral ganglion and corresponding octave bands are outlined. The scale bar is 2.5 mm. *Reprinted with permission from the publisher [64], under the Creative Commons CC BY license.*

The ion content between the perilymph (scala vestibuli and scala tympani) and the endolymph (scala media) differs, which is critical for the proper function of hair cells. Two structures are believed to play a key role in maintaining the endocochlear potential: the stria vascularis and the Reissner's membrane. The stria vascularis is a highly vascularized tissue lining and contains the blood-labyrinth barrier, which regulates the transfer of molecules from the capillary network to the endolymph [65]. It further produces and maintains the endocochlear potential by regulating the ion content between the perilymph and endolymph [66–68]. The Reissner's membrane is thought to be responsible for the sodium homeostasis of cochlear endolymph [69].

1.3 Cochlear modeling

Experimental studies of the cochlea are challenging due to limited access and its small size. Therefore, studies often rely on numerical simulations, analytical methods, or experiments in artificial models to gain insights into its function.

We will touch on some important relevant literature with a focus on coiled models and the effect of their spiral geometry, and place our work in the mentioned literature. More information about the broad field of cochlear mechanics can be found in Obrist [46], Reichenbach & Hudspeth [58], Paolis et al. [70], and Obrist [71].

Peterson & Bogert [72]'s model showed that the effect of compressible fast waves can be neglected compared to incompressible slow waves. In addition, the wavelengths of compressible waves are longer than the inner ear[3], thus the important effects are usually considered to be the incompressible ones, and the perilymph and endolymph are assumed to be incompressible [46, 73]. Exceptional contributions to auditory research were made by Georg von Békésy, who received the Nobel Prize in Medicine in 1961, inter alia, for his discovery of the traveling wave on the basilar membrane [11, 15].

One-dimensional transmission-line models provide an initial explanation for the traveling wave observed by von Békésy, and are based on incompressible flow that interacts with a compliant basilar membrane [72]. Lesser & Berkley [73] extended the one-dimensional model to a two-dimensional inviscid model, which reproduced the traveling wave and revealed particle trajectories near the characteristic place. Steele & Taber [74] used the Wentzel–Kramers–Brillouin method to describe viscous flow phenomena in the vicinity of the characteristic place in a three-dimensional (3D) uncoiled cochlea model. They pointed out that the fluid motion is fully three-dimensional. Based on the Wentzel–Kramers–Brillouin method, several more studies were performed in straight models [75, 76].

These models capture the key characteristics of the traveling wave and can explain the tonotopic organization of the cochlea, but there are many more processes to explore. Among the numerous emerging areas in cochlear modeling are steady streaming, active mechanisms, and anatomically more detailed or comprehensive models (involving the middle ear).

Steady streaming

Steady streaming effects in the cochlea were first pointed out by von Békésy [15], as so-called Békésy eddies, and later taken up by Lesser & Berkley [73] and Ranke [77]. Lighthill [55] suggested that the traveling wave generates streaming motions in the cochlea, which are highest near the characteristic place, and he approximated the mean streaming flow. He hinted that streaming mechanisms may stimulate inner hair cells.

Steady streaming describes the time-averaged net motion in an oscillating velocity field with zero mean flow [5, 78]. Different forms of steady streaming are, for example, described in Riley [78], and in context of the inner ear in Obrist [46] and Lighthill [55].

Several studies characterized steady streaming in the inner ear [4, 5, 79, 80]. Edom et al. [5] found high steady streaming velocities near the characteristic place and discussed

[3]For example, wavelengths from $\lambda = c_w/f = 0.075\,\mathrm{m}$ to $75\,\mathrm{m}$ correspond to frequencies ranging from $f = 20$ to $20'000\,\mathrm{Hz}$, assuming a speed of sound in water of about $c_w = 1500\,\mathrm{m/s}$ [73].

its potential for inner hair cell stimulation, metabolite transport, and drug delivery applications. Sumner et al. [4] further showed that steady streaming significantly extends in the longitudinal direction under suitable multi-frequency stimulation and tracked small massive particles for targeted drug delivery applications. Edom et al. [5] reported steady streaming velocities up to 300 μm/s for an acoustic stimulus of 94 dB at 1000 Hz. Sumner et al. [4] found streaming velocities of about 0.3 μm/s for 20′000 Hz at 80 dB sound pressure level (SPL). They explained the difference in the reported velocities (for comparable SPL) by the higher frequency.

Active mechanisms

Gold & Gray suggested that the cochlea not only acts as a passive instrument where basilar membrane displacements are detected, but that it actively increases signals [81, 82]. Kemp [83] later confirmed its active amplification by measuring acoustic emissions from the cochlea, i.e., otoacoustic emissions. The amplification of the basilar membrane motion is realized by the outer hair cells in the organ of Corti [84], which not only increase the sensitivity to a specific frequency, but also our ability to distinguish between two close frequencies [58, 85]. The fluid motion in the organ of Corti or in the subtectorial gap has recently gained importance for examining active processes involving hair cells [61, 86–90]. Still, many open questions remain regarding active mechanisms and inner hair cell stimulation in the cochlea [91].

Three-dimensional coiled models

Some researchers simulated the interaction between the cochlear fluids and the coiled basilar membrane (and the organ of Corti) in realistic three-dimensional (3D) geometries [92, 93], while others provide insight based on idealized geometries [27, 94–103]. Some examples will be named in the following.

Böhnke & Arnold [93] were the first to use a realistic 3D finite element model, with fluid-structure interactions, to model inviscid and compressible flow. Another finite element model based on a realistic geometry was later proposed by Givelberg & Bunn [92], who modeled viscous, incompressible flow. Both works reproduced the basic (passive) cochlear mechanisms. Furthermore, they suggested that their models could serve as a basis for further studies and be extended to include active processes once refined models are available.

An early study by Loh [95] applied the multiple scale analysis to reproduce the behavior of the traveling wave in an idealized curved model. Initially, the 3D model was based on a helical centerline with both curvature and torsion. For simplification reasons, the torsion was omitted eventually. An idealized, single-chamber model of the cochlea and vestibule was presented by Ren et al. [99]. In a follow-up study, the finite element model was extended to two cochlear chambers to compare the traveling wave mechanism under air and bone conduction [27]. Zhang & Gan [104] proposed a comprehensive idealized cochlear model including for the first time the ear canal, middle ear and spiral cochlea with three chambers as well as the basilar and Reissner's membranes. A similar model was recently applied to study blast wave transmission [105, 106].

To the best of the authors' knowledge, no follow-up studies to Givelberg & Bunn [92] and Böhnke & Arnold [93] were conducted, that include active processes in realistic models. Zhao et al. [102], however, included outer hair cells in an idealized cochlear model, under the assumption that the cilia are arranged in a straight line and stand free. Nonetheless, they proposed that the radial flow field deflects hair cell stereocilia most at the apex. An earlier study in an idealized spiral model with three chambers suggested that the shape of the cochlea impacts the radial pressure field distribution on the basilar membrane using a combined analytical and numerical approach [101]. Yao et al. [100] used a cochlear model including the osseous spiral lamina and the basilar membrane to numerically study the time-domain. Their model showed that the cochlea's spiral shape can induce asymmetrical mechanical behavior of the basilar membrane and cause cochlear fluid to move radially. Ultimately, all three studies suggested a potential benefit for low-frequency hearing [100–102].

Influence of coiling

Current research suggests that the spiral shape of the cochlea results from space constraints within the petrous bone during its development [17]. While the advantages of compactly packing a long organ are widely accepted, understanding the influence of the cochleas spiral shape on hearing remains challenging [107–109].

Most cochlear models simplify the cochlea as a straight duct, neglecting its curvature due to the low Reynolds number and Dean number [46]. Curvature and torsion are described in the context of the cochlea in the next section and more generally in Chapter 2. Several studies stated that curvature can be neglected [53, 94–96]. von Békésy [53] studied the travelling wave in a straight and a curved enlarged cochlear model and did find no effect of curvature on the travelling wave [53]. This was reconfirmed by Ren et al. [99] and Cai et al. [110]. von Békésy [15] however, suggested that coiling could be beneficial for the organ of Corti and, e.g., improve bending capabilities of the tectorial membrane. Huxley [111] proposed that curvature might cause the sharp resonant vibrations of the basilar membrane, von Békésy and Loh, however, observed no such effect in their work. More recent studies are investigating the effect of coiling on hair cells [102, 110]. Loh [95] left out torsion for simplification, but suggests that it might be relevant to include.

Other studies in 3D geometries described the effects of coiling on the pressure and the velocity fields [96, 99–101, 112]: De Paolis et al. [112] showed that the maximum velocities are shifted toward the inner wall of the cochlear scalae, Ren et al. [99] found that the spiral shape induced a tilt in the pressure gradient with lower pressures on the inner side of the curve.

Moreover, several studies describe an effect of curvature and coiling and the spiral shape on hearing, especially on low-frequency hearing. Curvature enhances the movement of hair cell stereocilia at the apex, benefitting low frequency hearing [110]. In addition, Zhao et al. [102] suggested that radial flow displaces hair cells stereocilia the most at the apex. Manoussaki et al. [107] proposed that the low-frequency hearing threshold in different species correlates with a radii ratio of the cochlear turns. Pietsch et al. [17] could however not confirm their findings. In an earlier study, Manoussaki et al. [97] showed that the spiral

shape redistributes wave energy along the radial direction — similar to a "whispering gallery effect" — altering the radial vibration profile of the various cochlear structures and potentially benefiting low-frequency hearing.

While it is generally agreed that the spiral shape results from space constraints, there may still be an additional benefit of coiling for hearing. The effect of the spiral shape on fluid mechanics within the cochlea remains elusive and requires further research.

Abstracting cochlear geometry

The kinematic surface fitting algorithm by Wimmer et al. [113] gives an intuitive explanation of the natural growth process of the cochlea. It can be, inter alia, used to determine shape parameters (rotation, translation, scaling) from surface data of the cochlea. These shape parameters mathematically describe the cochlear geometry by a spiral velocity field. We used this field to define a spiral centerline going from the base to the apex. Subsequently, the Frenet-Serret frame (see section 2.3) was applied to define the curvature and torsion at each point along the centerline. The torsion τ of a twisted duct is a measure of its twist; the distance required for one full turn equals $2\pi/\tau$ in an only twisted duct, see e.g., [114]. In a toroidal duct, the radius of curvature equals the inverse of the curvature κ. Low curvature thus implies a large radius of curvature, and low torsion a slowly twisting duct. Kinematic surface fitting showed, that the torsion as well as curvature increase towards the apex of the cochlea. The latter is a consequence of the decreasing radius of curvature towards the helicotrema.

To be able to study the effect of curvature and torsion separately, we used four models: A straight duct, a twisted duct, a toroidal duct and a helical duct. The twisted duct has a centerline torsion of $\tau = 1/8\,\mathrm{mm}^{-1}$ (i.e., a distance of approximately 50 mm for one turn) and the toroidal duct has a centerline curvature of $\kappa = 1/3\,\mathrm{mm}^{-1}$ (i.e., a radius of curvature of 3 mm). The helical duct exhibits, both, a non-zero curvature and a torsion and is described in section 2.3.

Classification of the square duct models

In this thesis, the effect of geometry, i.e., curvature and torsion, on fundamental phenomena is studied in abstracted helical square duct models, which were described in the previous section. We place our work in the corner of abstract 3D coiled models. Because of the complex morphology of the cochlea and its sophisticated mechanisms and processes, no study can yet include every detail. The characteristics of the models in this thesis are:

- helical with curvature and torsion
- single chamber
- rigid walls
- no basilar membrane, thus no travelling wave

- passive
- incompressible, viscous Newtonian fluid
- unsteady Navier-Stokes equations including nonlinear effects

These simplifications allow us to study and visualize transverse flow phenomena and their associated effects (such as wall shear stresses and Lagrangian streaming).

1.4 Effects of geometry on fluid flow at low Reynolds numbers

Geometry profoundly influences fluid dynamics. The interplay between geometry and flow at low Reynolds numbers is for example used in microfluidic devices to separate cells and particles [115, 116], to improve mixing performance [117], or to enhance the efficiency of heat exchange devices [118]. Low Reynolds number flows are also crucial to blood flow in small vessels [119, 120] and to organs in our bodies, like the cochlea. The broad literature on pipe flows at low Reynolds numbers can be categorized according to the following criteria:

- governing equations (steady, unsteady)
- flow development (transient, fully developed)
- duct geometry (e.g., toroidal, twisted, helical)
- cross-section shape (e.g., elliptical, round, rectangular)

Herein, the focus lies on fully developed flows of an incompressible Newtonian fluid at low Reynolds numbers (entry length effects or transient developing flows are not addressed). Furthermore, for unsteady flows, only purely oscillatory cases are considered because of their relevance to cochlear flow.

The relevant dimensionless numbers, the Reynolds number Re (proportional to the fluid velocity) and Womersley number α (proportional to the square root of the frequency) are defined in Chapter 2. They describe the transient inertial force as well as the inertial force with respect to the viscous force, respectively. Finally, the Dean number, used to describe flow in toroidal ducts, is proportional to the Reynolds number $De = Re\sqrt{d_h/(2R)}$, where d_h is the hydraulic diameter of the pipe and R is the radius of curvature.

The following sections introduce axial and transverse flows, describe the effect of geometry on the fluid motion, and review techniques to derive or visualize them.

Definition of axial and transverse flow

Secondary flow is a relatively weaker flow pattern superimposed on a stronger primary flow. Primary flow is often defined as the exact flow solution to simplified governing equations (e.g., potential flow), while secondary flows are phenomena that deviate from this assumed theory in practice (e.g., flow with vorticity) [121]. In pipes, secondary flows are usually

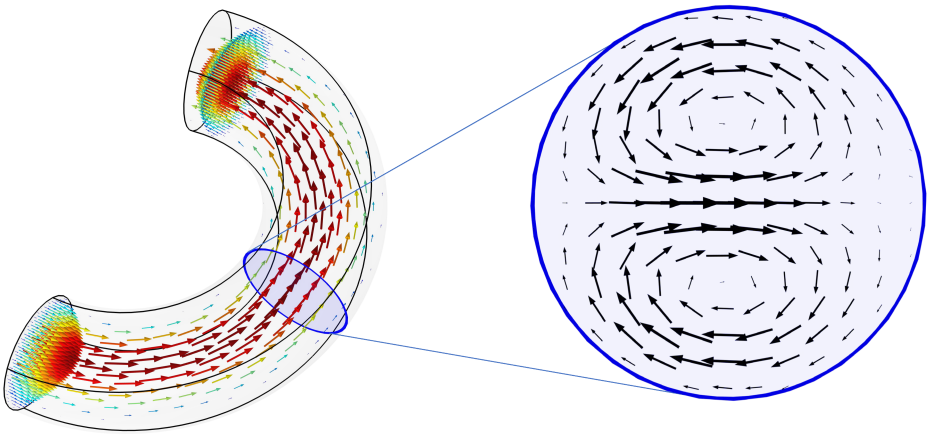

Primary flow (axial) Secondary flow (transverse)

Fig. 1.8. Primary and secondary flows in a curved pipe. The colored arrows indicate the primary flow magnitude.

defined as a motion perpendicular to the longitudinal axis (see Fig. 1.8). In this thesis, the term "transverse flows" is used to refer to secondary flows, as they are in the cross-section of the pipe, transverse to the primary, axial flow.

The importance of secondary flows can be highlighted by the many areas where they occur, including biological systems (in our bodies e.g., the vascular system [123, 124], the lymph system in the inner ear [55, 61]), atmospheric winds and the tea-leaf paradox [125, 126], and industrial applications (e.g., brewing industry [127]). In a curved river, secondary flows can pull water from the top part of the river (in the cross-section) toward the outside of the bend, while at the bottom of the river they are mostly directed towards the inner curve [122, 125]. These secondary flows transport sediments and are partly responsible for the occurrence of sandbars along the inside of the bend, as shown in Fig. 1.9.

Fig. 1.9. Meandering River. Secondary flows in a curved river can contribute to the formation of sediment deposition at the inner bank [122]. *Not included in the Creative Commons Attribution 4.0 International License. Reprinted from Coral_Brunner, image no. 272183592 - stock.adobe.com*

Effect of geometry on axial flow

As a steady flow goes around a bend, curvature alters its axial velocity profile. At low Reynolds numbers, it shifts the maximum of velocity towards the inner wall [128]. An explanation for this observation is given in Chapter 2. In contrast, fluid flows faster near the outer wall at higher Reynolds, see e.g., Liu & Masliyah [129] and Zabielski & Mestel [130].

Torsion has only a small impact on the axial velocity profile in square ducts at low Reynolds numbers [131, 132]. For high torsion values, the velocity profile becomes similar to that of a straight circular tube, as fluid flows mainly through the "straight, untwisted regions". Since the twist in the cochlear scalae is low [94, 133], no significant change in the axial velocities is expected because of torsion [132].

In helical ducts, also the combined effect of torsion and curvature resembles the one of curvature alone at low Reynolds number [130]. The highest axial velocities are thus expected close to the modiolus in the cochlea [112].

Oscillating flow is characterized by the Womersley number. For higher frequencies, i.e., higher Womersley numbers, it shows a "plug flow" profile with steep gradients at the walls

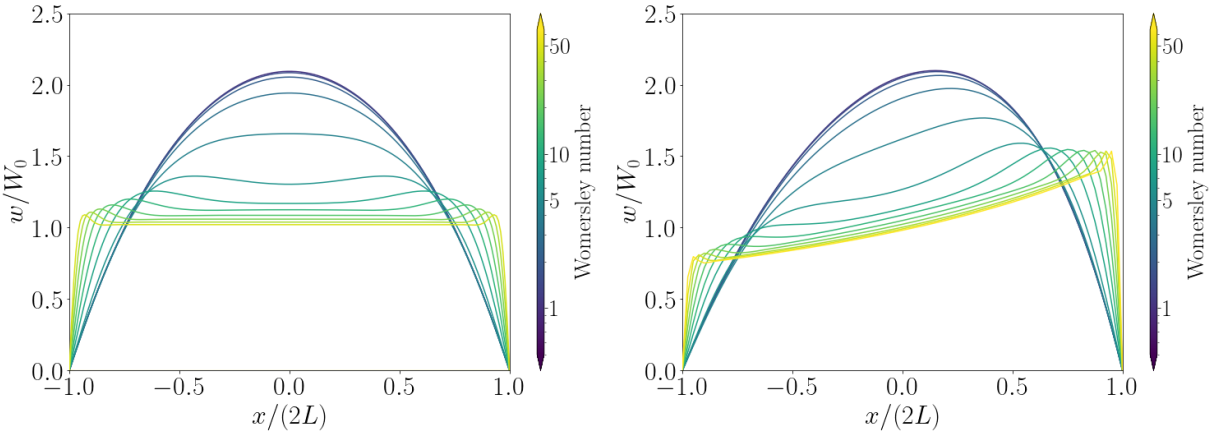

Fig. 1.10. Womersley flow profiles for different Womersley numbers in a straight (left) and a toroidal duct (right) with a curvature of $\kappa = 1/3$. In the toroidal duct, for a Reynolds number of 0.58, the velocity profile is skewed towards the inner wall of the curve (towards the right). Lower oscillation frequencies result in a quasi-stationary profile resembling steady Poiseuille flow, while higher oscillation frequencies exhibit a plug flow profile.

(Fig. 1.10) [134]. The spatial distribution of the flow amplitude is similarly affected as in steady flows. In unsteady, oscillating flows, an interesting phenomenon is the time-averaged net flow, i.e., steady streaming. There are no significant axial Eulerian streaming velocities because of curvature alone, as there is no preferred direction for flow in a toroidal duct [135]. Torsion on the other hand leads to axial streaming in helical ducts. An upward net motion can be found at the top of the cross-section and a downward net motion at the bottom [135].

Effect of geometry on transverse flow

The geometry of a toroidal duct causes pairs of rotating flow cells in the transverse plane, known as Dean cells (Fig. 1.8 and Fig. 1.12) [136]. They arise because of centripetal forces, and their strength depends on the square of the Reynolds number in steady flows [137].

In twisted ducts, the transverse flow pattern strongly depends on the cross-sectional geometry. In ducts with an elliptical cross-section, torsion leads to a so-called "saddle flow" structures (Fig. 1.11) [138]. A similar structure arises in ducts of rectangular [137] and square cross-sections [131, 132]. The maximal strength of the saddle flow structure depends linearly on the Reynolds number and the torsion in steady flows [137]. For high torsion, a circulatory motion, a "swirl", is additionally induced [131, 132]. For the torsion of the cochlear scalae [94, 133], however, the saddle flow structure is expected to be dominant [137].

A combination of both effects occurs in the helical duct. For lower Reynolds numbers, the transverse flow pattern in square cross-sections exhibits a saddle flow, see e.g., Bolinder [137]. Liu & Masliyah [129] and Zabielski & Mestel [130] found a one vortex structure in circular cross-sections at low Reynolds numbers, which is thought to originate from torsion effects [130]. For higher Reynolds numbers, both effects are taken over by two Dean cells (as their strength increases quadratically with the Reynolds number) [130]. In square ducts,

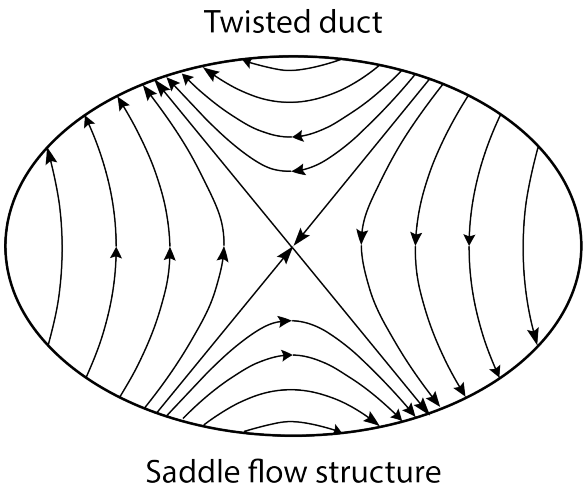

Fig. 1.11. Schematic of saddle flow structure in a twisted duct. Looking into the page plane, the twisted duct turns clockwise and the axial velocity is inflowing.

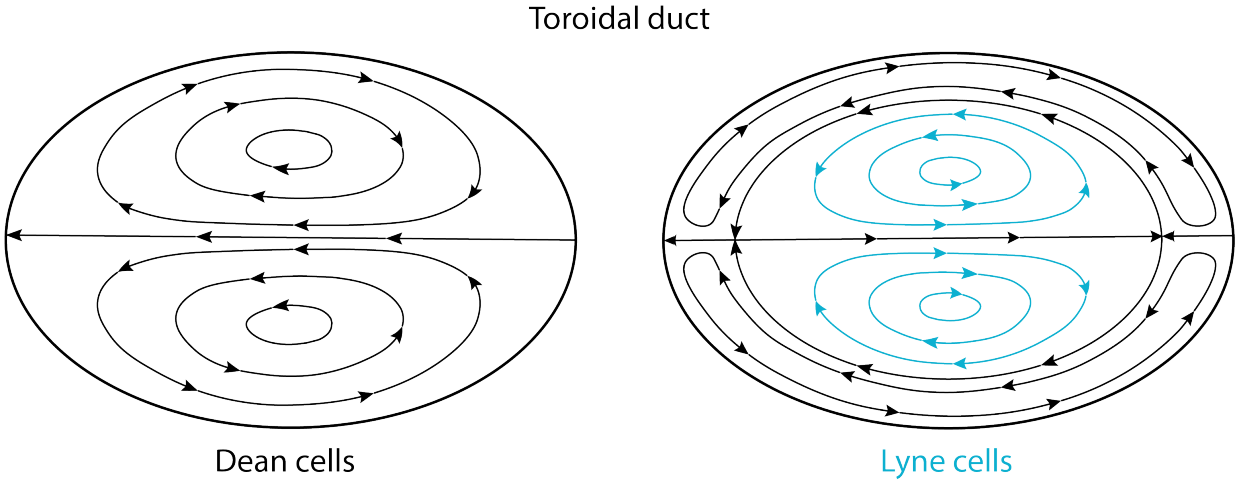

Fig. 1.12. Schematics of Dean cells (left) and Lyne cells (right, in blue) in a toroidal duct. Lyne cells are a second pair of rotating vortices that form in the center of the cross-section for high enough Womersley numbers. Their direction is opposite to that of Dean cells. The outer wall of the curve is to the left.

for equal values of torsion and curvature, curvature becomes more important for Reynolds numbers of roughly nine and above [137]. In ducts with a cross-section with an aspect ratio of two, torsion has an even stronger influence [137]. This observation is particularly interesting considering the irregular cross-section of the cochlea.

Unsteady flows in toroidal ducts exhibit Dean cells, similar to the steady case. For sufficiently high Womersley numbers or frequencies, an additional pair of counter rotating cells forms in the center of the cross-section, which rotate in the opposite direction to the Dean cells, see Fig. 1.12 [139]. More information on the different types of recirculating vortices in toroidal ducts for different Dean numbers (proportional to the Reynolds number)

and Womersley numbers are described by Sudo et al. [140]. When the axial flow changes direction, Dean cells do not. They are uniform for inflowing and outflowing velocities because of their inertial nature. Transverse Eulerian streaming in curved and helical ducts occurs as steady Dean cells [135]. According to Zabielski & Mestel [135], the torsion of the helix has only a limited effect on Eulerian streaming in the cross-section.

State-of-the-art axial and transverse flow quantification methods

Researchers have studied axial and transverse flow in curved ducts analytically, numerically, and experimentally. Except for simple geometries, e.g., a straight square duct [141], these flows can't be solved analytically. While the previous sections addressed the flow phenomena, this section is focused on the techniques applied to obtain them. The first part discusses mainly analytical and numerical studies in toroidal, twisted and helical geometries, while the second part gives an overview of experimental techniques.

The history of secondary flow studies in toroidal ducts extends from Dean's pioneering work, nearly a century ago, to the present and is still actively researched [136, 142, 143]. Dean performed an analytical analysis under the assumption that the pipe diameter of the toroidal duct is much smaller than the radius of curvature, in the following referred to as small curvature, and characterized a pair of rotating vortices. This secondary, i.e., transverse flow is known as Dean flow [136]. Dean cells were studied in great depth, and an overview is given in a comprehensive review article by Berger et al. [144]. Dean flow under oscillating stimulation was studied extensively by Lyne [139], Sudo et al. [140], and Siggers & Waters [145] in toroidal circular ducts. Lyne [139] described the occurrence of a second pair of rotating cells for higher Womersley numbers. He performed a perturbative expansion in the inverse of the Womersley number and derived asymptotic theories, inter alia, for high oscillation frequencies. Sudo et al. [140] summarized different types of Dean cells depending on the Dean and Womersley numbers using numerical and experimental studies. Performing a perturbation in small curvatures, Norouzi & Biglari [146] presented an analytical solution for incompressible flow in curved ducts with a rectangular cross-section.

Transverse flows in twisted ducts were studied under steady conditions for rectangular and elliptical cross-sections by Masliyah & Nandakumar [131] and Kheshgi [132] and Germano [138], Chang et al. [147], and Tuttle [148], respectively. The results were obtained either by numerical simulations in twisted ducts or as an analytical limit of the more general case of a helical duct, see e.g., [138].

The helical coordinate system is non-orthogonal (see e.g., [149, 150]) and therefore requires either tensor analysis (using covariant and contravariant vectors, which are related by the metric tensor) to express the governing equations, or needs to be transformed into an orthogonal system. Germano [151] proposed a coordinate transformation that yields an orthogonal system. Tuttle [148] later showed that the results from both approaches, non-orthogonal and orthogonal coordinate systems, are equivalent, when correctly interpreting covariant and contravariant vectors. Another orthogonal coordinate system, which is based on helical symmetry, was proposed by Zabielski & Mestel [130]. Unlike the previous approaches, their method does not require the assumption $a\kappa \ll 1$, where a is the pipe radius and κ the curvature.

Helical duct flow was studied in great detail under laminar steady flow [129, 130, 137, 138, 148, 151–157]. Two works on helical flow will be introduced in more detail because of their relevance to this thesis.

Bolinder [137] studied steady laminar flow in rectangular ducts analytically and numerically for industrial application. He did a perturbative expansion in small curvature and torsion and compared first order solutions to the ones obtained with the full Navier-Stokes equations. His findings assess the maximum magnitude of secondary flows in curved and twisted ducts as a function of the Reynolds number and for various curvature and torsion values. His first order results, however, neglect nonlinear terms. They do therefore not capture the shift in the axial velocity profile because of the helical pitch.

A comprehensive and detailed study for steady and unsteady helical flows was presented by Zabielski & Mestel who examined transverse flows analytically and numerically [130, 135]. Their method reduces the problem to two dimensions, by applying helical symmetry, and is carried out for arbitrary constant values of curvature and torsion. While they only discuss circular and square cross-sections, their method is applicable to other constant cross-sections as well. They analytically extended the asymptotic theory derived by Lyne for high oscillation frequencies to helical ducts. The results are mostly discussed for higher Reynolds numbers and a Womersley number of 20 (for blood flow). Nonetheless, a small part is devoted to low Reynolds numbers and some results for square cross-sections are presented. Furthermore, Eulerian streaming effects and wall shear stresses are addressed.

Studies often directly compared their analytical approximations (perturbation method, asymptotic theories, etc.) either with numerical results obtained from the full Navier-Stokes equations or with experimental data. A variety of experimental techniques were applied to measure or visualize axial and transverse flows in toroidal and helical ducts.

Flow visualizations were, for example, done with dye injection [139, 158–161]. Highly resolved transverse flow patterns were obtained by Krishna et al. [161], who injected fluorescein dye to visualize flow separation and transverse flow vortices, and by Timité et al. [160], who studied the development of secondary flows in toroidal ducts. Boiron et al. [159] combined fluorescein injections with velocity measurements from pointwise hot-film anemometry.

Sudo et al. [140] visualized Dean flows in toroidal ducts by capturing photographs of suspended nylon particles. They characterized the obtained net motion into five different patterns. Multiple studies combined such secondary flow visualization techniques with laser Doppler velocimetry measurements [160, 162, 163]. For example, Bolinder & Sundén [163] used laser Doppler velocimetry to validate velocity profiles from numerical calculations in a helical duct. To visualize the flow patterns, they dispersed polystyrene particles in the fluid, illuminated the transverse plane with a laser sheet and photographed it with a camera.

Perhaps the most frequently used experimental technique for transverse flows at present is particle image velocimetry (PIV). Highly resolved transverse flow patterns were obtained by stereo PIV [164] or by two-dimensional (2D) PIV, applied directly on the transverse plane with a single camera. The latter has been used in several related studies for applications addressing flows in the arteries [165–169]. Besides laser PIV, also ultrasonic particle image velocimetry, EchoPIV, was applied to study axial flows in a toroidal duct [170] and transverse flows in helical stent models (in-vitro) [124, 171].

Coutinho et al. [172] applied 3D defocusing particle tracking to a toroidal artery model with a radius of 0.8 mm to visualize transverse and axial flows. Since the setup was built for smaller dimensions, they shifted the focal plane in steps of 300 μm to cover the full pipe diameter. They used Reynolds numbers of 480 and therefore the transverse flows are much higher with respect to the axial flows than at low Reynolds number.

Most mentioned studies visualized transverse flows in pipes with larger diameters (12-35 mm) than the scale of the cochlear scalae [161, 164–167]. This is because they are often geared towards flow in the arteries. To perform real scale measurements in millimetric models, e.g., the scales of the inner ear, experimental techniques with high spatial resolution are needed. More importantly, these techniques need to be able to capture small axial flow displacements and even smaller transverse flows. EchoPIV is noninvasive and does not need optically transparent models, and recent advances allow for 3D velocity measurements [173]. But the spatial resolution and signal-to-noise ratio are rather low [173, 174]. 3D defocusing particle tracking is effective and can be applied to small dimensions. However, it requires an elaborate calibration and is limited in particle densities because overlapping of particles in the acquired images introduces uncertainties [175, 176]. Laser PIV is promising for the study of low Reynolds number transverse flows, as it offers high accuracy and does not require sparse particle densities.

Particle image velocimetry to measure transverse flows

Particle image velocimetry (PIV) is a measurement technique that derives a velocity field by analyzing images of tracer particles suspended in a moving fluid. It can be observed in a simplified form in natural phenomena. Adrian [177] described an example similar to what can be encountered on Lake Thun in the spring. The lake's surface accumulates pollen. One can then take two images of the lake's surface and compare the position of the pollen pattern in the two images. Dividing the difference in their positions by the time between the images allows us to determine the velocity of the pollen and therefore the flow at the surface. The pollen effectively serves as tracers to capture the motion of the lake's water.

In its technical form, PIV usually involves a laser, an optically transparent test section, at least one high-speed camera, and tracer particles which are suspended in the fluid to be measured. The tracer particles are typically fluorescent and small enough to move at the same velocity as the fluid. For neutral buoyancy, they should have the same density as the fluid. A laser sheet is used to illuminate a thin plane within the fluid where the flow is to be measured. The laser light excites the tracer particles, which then emit light at a lower wavelength. A camera captures the illuminated plane in a fast series of images. Based on the cross correlation of sub-regions in successive images, PIV algorithms calculate the velocity vectors at discrete points within the captured image. A textbook by Raffel et al. [178] provides a detailed introduction to the concepts and techniques of PIV and more details can also be found in Adrian [177], Etminan et al. [179], and Rohacs et al. [180].

PIV in its traditional form is 2D, but several extensions were developed to measure a full velocity field in a volume, referred to as three-dimensional three-component (3D3C) techniques. These include, for example, holographic PIV [181, 182], tomographic PIV [183–185], and scanning PIV. We will focus on scanning PIV in the following, because of its relevance to Chapter 4.

In scanning PIV, fast successive scans of a laser sheet through a volume of interest are recorded with a single high-speed camera [186, 187]. The camera is synchronized with the laser to ensure accurate timing of the images. The height of the test section, that can be scanned, is set by the depth of field of the camera system, i.e., the whole test section needs to be in reasonable good focus. The time to scan the volume should be much shorter than the timescale of the flow of interest, as the different heights are captured sequentially [178, 188]. This requires that the scanning frequency of the laser is much higher than the flow frequency. In addition, the high camera frame rates are needed to obtain the desired temporal resolution. This limits its application for fast flows [178], while flows in millimetric and micrometric applications are often slow enough to allow sequential, step-wise scanning. David et al. [189] applied a scanning laser sheet with a tomography technique, and based the PIV analysis on the cross-correlation between successive volumes. The advantages of scanning PIV include very high accuracy, which is mainly limited by the camera features. As cameras continue to improve in resolution, sensitivity, and frame rate, the importance of scanning PIV increases.

1.5 Thesis objectives and overview

This thesis aims to investigate the effect of cochlear morphology on secondary flow phenomena in an effort to improve our understanding of cochlear mechanics. The cochleas spiral shape is particularly curved and twisted towards the apex, where low frequencies are processed. Moreover, several studies suggested that the spiral shape of the cochlea may enhance on low-frequency hearing [97, 100–102]. This motivates our main hypothesis that torsion facilitates low-frequency hearing, in particular, by causing transverse flow. Consequently, the following work is focused on low frequencies (up to 256 Hz). For this purpose, the effects of geometric curvature and torsion on fluid motion are quantified in abstracted geometries. Since the objective is to investigate passive mechanical effects of shape on transverse flow, active cochlear mechanisms will not be addressed. This thesis summarizes the emerging flow phenomena in three chapters.

During the hearing process, the stapes vibrates at the oval window and causes subtle oscillation in the cochlear fluids. In **Chapter 2**, axial and transverse flow patterns are studied under oscillatory stimulation in toroidal, twisted, and helical square ducts. The effect of curvature and torsion on the strength of transverse flows is discussed for a variety of frequencies, covering both infrasound and low frequency hearing, and flow magnitudes (corresponding to different sound pressure levels). Shifts in the spatial position of maximum axial flow were observed in the ducts for different Womersley numbers. The effect of geometry on phase differences between pressure and axial as well as transverse flow velocities were examined as well.

Transverse flows are intricately coupled with pressure fluctuations in the cross-section and can be, both, cause and effect of them. In addition, axial and transverse flows cause wall shear stresses. Pressure fluctuations as well as shear stresses are presented in **Chapter 3**. The wall shear stress is decomposed into an axial and a transverse component to quantify its relative strength in the transverse direction. Based on the dominant force, we described two regimes of maximum wall shear stresses and pressure variations with respect to the Womersley number (i.e., oscillation frequency). While the low frequency regime is dominated by non-linear, viscous effects, the higher one demonstrates an onset of transient inertial forces, particularly in the presence of torsion.

Chapter 4 builds on the findings of Chapter 2, and introduces a new three-dimensional particle image velocimetry (PIV) technique to visualize the subtle oscillating flows. The setup is tested on a custom-built straight, twisted, and toroidal flow channel with a diameter of approximately 2 mm. The technique allows for measuring both time-resolved axial and transverse flows, as well as net motions (Lagrangian streaming). The PIV results are compared to simulations in the measurement samples and to simulations in the idealized models from Chapter 2. Cross-sectional streaming is discussed as a potential mixing mechanism.

And finally, in **Chapter 5**, the presented work is summarized, its limitations are discussed, and potential directions for the future of the project are outlined.

CHAPTER 2

TRANSVERSE FLOW UNDER OSCILLATING STIMULATION IN HELICAL SQUARE DUCTS WITH COCHLEA-LIKE GEOMETRICAL CURVATURE AND TORSION

This chapter is submitted as:
Harte N.C., Obrist D., Caversaccio M.D., Lajoinie G.P.R. and Wimmer W. Transverse flow under oscillating stimulation in helical square ducts with cochlea-like geometrical curvature and torsion.

Axial and transverse flows in a straight, a twisted, a toroidal and a helical square duct are presented for a range of frequencies and velocity amplitudes. A scaling of the maximum transverse flows with Womersley number and Reynolds number is established based on the studied parameter ranges. A significant increase in maximum transverse flow is demonstrated in the helical geometry compared to exclusively twisted or toroidal ducts.

Author contribution: Conceptualization and methodology, mesh generation, numerical simulations, data analysis, manuscript writing and data visualization.

2.1 Abstract

The cochlea is our fluid-filled organ of hearing with a unique spiral shape. The physiological role of this shape remains unclear. Previous research has paid only little attention to the occurrence of transverse flow in the cochlea, in particular in relation to the cochlea's shape. To better understand its influence on fluid dynamics, this study aims to characterize transverse flow due to harmonically oscillating axial flow in square ducts with curvature and torsion, similar to the shape of human cochleae. Four geometries were investigated to study curvature and torsion effects on axial and transverse fluid flow components. Twelve frequencies from 0.125 Hz to 256 Hz were studied, covering infrasound and low-frequency hearing, with mean inlet velocity amplitudes representing levels expected for normal conversations or louder situations. Our simulations show that torsion contributes significantly to transverse flow in unsteady conditions, and that its contribution increases with increasing oscillation frequencies. Curvature has a small effect on transverse flow, which decreases rapidly for increasing frequencies. Strikingly, the combined effect of curvature and torsion on transverse flow is greater than expected from a simple superposition of the two effects, especially when the relative contribution of curvature alone becomes negligible. These findings could be relevant to understand physiological processes in the cochlea, including metabolite transport and wall shear stresses. Further studies are needed to investigate possible implications on cochlear mechanics.

2.2 Introduction

The cochlea, our organ of hearing, is a fluid-filled structure with a peculiar spiral shape. Despite its importance, the physiological role of its shape in sound transmission from the cochlear fluids to the sensory epithelium remains unclear. Performing experimental investigations is challenging because of the limited access to the cochlea and its small size. Therefore, existing literature is based on numerical simulations or theoretical studies. For example, researchers have simulated the interaction between the cochlear fluids and the basilar membrane (or the organ of Corti) in realistic geometries [92, 93, 110], while others provide theoretical insight based on idealized geometries [94–97]. Manoussaki et al. [107] showed that the spiral shape redistributes wave energy along the radial direction, altering the radial vibration profile of the various cochlear structures and affecting low-frequency hearing. However, geometry-related secondary flow phenomena, especially the occurrence of transverse flow (i.e., flow in the cross-section of the cochlea) have received little attention.

Since the physiology of the ear is fundamentally coupled to fluid dynamic processes, a more detailed understanding of the influence of geometric properties on the flow field is desirable. In this context, possible mechanisms could be secondary phenomena introduced by transverse flow. The combination of oscillating axial flow and transverse flow caused by geometry leads to steady streaming effects and net transport of particles [78]. Therefore, cross-sectional mixing and longitudinal streaming caused by transverse flow could be relevant for the transport of metabolites in the cochlea [190]. In the context of medical treatment, intracochlear fluid-borne mass transport (drug delivery) is an active area of research [4, 46]. Moreover, transverse flow can generate wall shear stresses and pressures that could reach magnitudes that may be considered physiologically relevant in the cochlea.

Curvature and torsion are elementary properties that can be used to describe duct geometries by the centerline. Relatively simple shapes can generate complex transverse flow patterns. The geometry of a toroidal duct, only exhibiting curvature, causes pairs of rotating flow cells oriented in the transverse plane, known as Dean flow [136]. Inside twisted straight ducts, which only contain torsion, saddle flow patterns are generated depending on the cross-section of the duct [132, 138]. More complex phenomena arise in helical ducts with curvature and torsion combined, as has been extensively studied by Bolinder [137] and others [130, 148, 152, 154] under laminar steady flow conditions. Transverse flow occurring under oscillatory stimulation in toroidal circular ducts was studied by Lyne [139], Sudo et al. [140], and Siggers & Waters [145]. An elegant solution for oscillating helical flows was presented by Zabielski & Mestel [135], who examined transverse flows in helical rectangular and circular ducts analytically and numerically. We did not use their semi-analytic method for our application, as we wanted to keep the option open for future inclusion of more complex geometries (including tapering and fluid-membrane interactions). Recently, the study of helical flows has also gained attention in the context of the arterial vasculature [157, 166, 191–193].

Motivated by the question of the physiological role of the cochlear shape, the aim of this study is to fundamentally characterize transverse flow phenomena under harmonic oscillation in square ducts with curvature and torsion reflecting the shape of human cochleae. Computational fluid dynamics (CFD) is used to simulate flow at oscillation frequencies within the infrasonic and low-frequency hearing range of humans because the apical region

of the cochlea, characterized by a high degree of curvature and torsion, is particularly sensitive to these frequencies. The results of this study include axial velocity profiles, transverse flow patterns, relative transverse flow magnitudes and phase differences between pressure and velocity. Interestingly, we find that torsion remains the dominant contributor to transverse flow under oscillating stimulation, similar to its role under steady flow conditions. Additionally, we observe that the combined contribution of curvature and torsion to transverse flow is larger than expected based on a simple superposition of the two effects.

2.3 Methods

Duct geometries

To characterize the contributions of curvature and torsion to the flow field, we simulated fluid flow in four different geometries (Fig. 2.1). We defined the geometries using established methods [114, 137], which are summarized here. The centerlines of the geometries are described by the position vector $\mathbf{r} = \mathbf{r}(s)$ and parametrized with the arc length s. To facilitate the decomposition into axial and transverse flow components later on, we use the orthonormal Frenet-Serret frame consisting of the tangent ($\widehat{\mathbf{t}}$), normal ($\widehat{\mathbf{n}}$), and binormal ($\widehat{\mathbf{b}}$) unit vectors:

$$\widehat{\mathbf{t}} = \mathbf{r}', \quad \widehat{\mathbf{n}} = \frac{\widehat{\mathbf{t}}'}{\|\widehat{\mathbf{t}}'\|}, \quad \text{and} \quad \widehat{\mathbf{b}} = \widehat{\mathbf{t}} \times \widehat{\mathbf{n}}, \tag{2.1}$$

where the prime indicates the derivative with respect to the arc length s. The curvature κ and torsion τ of the centerline are defined as

$$\kappa = \left\|\widehat{\mathbf{t}}'\right\| \quad \text{and} \quad \tau = \widehat{\mathbf{n}}' \cdot \widehat{\mathbf{b}}. \tag{2.2}$$

For the helical centerline, we obtain

$$\kappa = \frac{R}{K^2 + R^2} \quad \text{and} \quad \tau = \frac{K}{K^2 + R^2} \quad , \tag{2.3}$$

where R is the radius and $2\pi K$ is the pitch of the helix, i.e., the height of a complete helical turn. The toroidal duct (Fig. 2.1b) has a centerline with zero torsion and a curvature of $1/R$. In contrast, the centerline of the twisted duct (Fig. 2.1c) has zero curvature and a torsion of $1/K$. For our geometries, the centerline curvature and torsion were chosen as $\kappa = 1/3\,\mathrm{mm}^{-1}$ and $\tau = 1/8\,\mathrm{mm}^{-1}$, respectively, to match average properties observable in human cochleae [94, 133]. However, it should be pointed out that certain values for curvature and torsion would be inadmissible, as the duct would intersect itself. A typical radius for the basal turn of the cochlea is around 3 mm and the radius decreases to approximately 1 mm for the apical turn [47, 48, 133]. The total height of the cochlea measures typically about 4 mm and the height difference per turn is around 1 mm. The value for K may be estimated as 0.1 mm at the base and as 0.05 mm at the apex.

To save computational cost, we reduced the total arc length of the centerline for all models to $s_{max} = 10\,\text{mm}$, which is shorter than a human cochlea (37 mm) [194]. The models have a $2\,\text{mm} \times 2\,\text{mm}$ cross-section to capture typical dimensions of the cochlear cross-section [195].

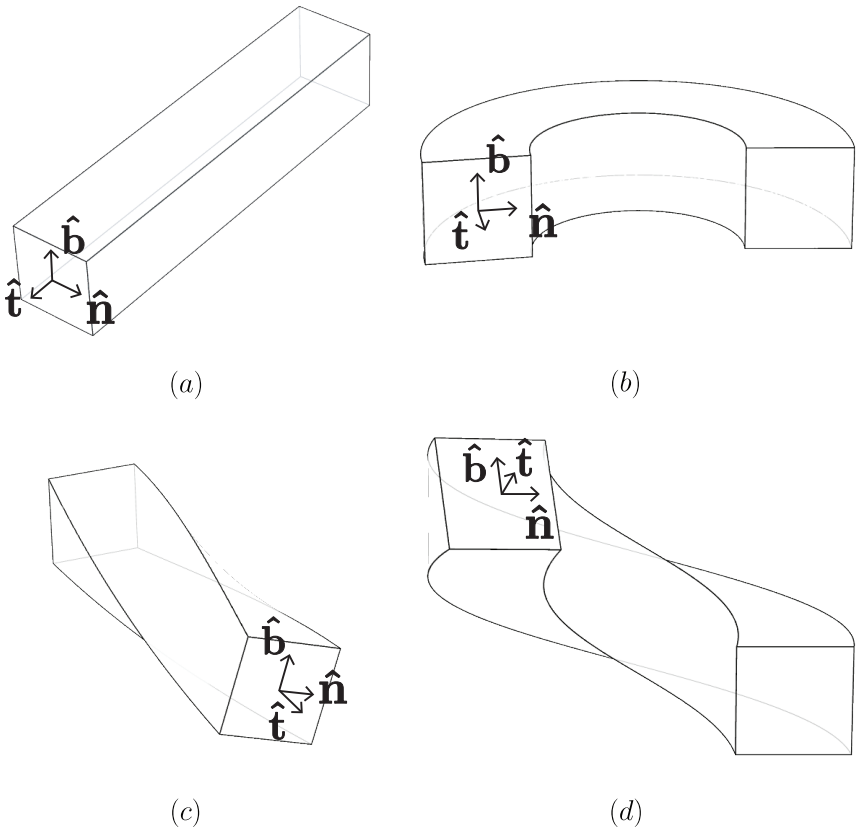

Fig. 2.1. The geometries with corresponding curvature κ and torsion τ. (a) Straight duct with $\tau = \kappa = 0\,\text{mm}^{-1}$, (b) toroidal duct with $\tau = 0\,\text{mm}^{-1}$ and $\kappa = 1/3\,\text{mm}^{-1}$, (c) twisted duct with $\tau = 1/8\,\text{mm}^{-1}$ and $\kappa = 0\,\text{mm}^{-1}$, and (d) helical duct with $\kappa = 1/3\,\text{mm}^{-1}$ and $\tau = 1/8\,\text{mm}^{-1}$.

Model implementation

The perilymph flow in the cochlea is modelled as flow of an incompressible Newtonian fluid [50], by the Navier-Stokes equations

$$\begin{aligned} \nabla \cdot \mathbf{u} &= 0 \quad \text{and} \\ \rho \frac{\partial \mathbf{u}}{\partial t} + \rho(\mathbf{u} \cdot \nabla)\mathbf{u} &= -\nabla p + \mu \Delta \mathbf{u}, \end{aligned} \tag{2.4}$$

where $\mathbf{u} = \mathbf{u}(x, y, z, t)$ and $p = p(x, y, z, t)$ are the velocity and pressure fields at time t represented in an Eulerian reference frame. The dynamic viscosity and the fluid density

are denoted by μ and ρ, respectively (Table 2.1). At the inlet and outlet surfaces, the pressure p_{out} and p_{in} were set to

$$p_{\text{in}}(t) = P_0 \cos(2\pi f t) \quad \text{and} \quad p_{\text{out}}(t) = 0, \tag{2.5}$$

with the oscillation frequency f and the pressure amplitude P_0. No-slip boundary conditions were imposed on the walls. We performed simulations at 12 frequencies ranging from 0.125 Hz to 256 Hz in powers of two. This frequency range corresponds to infrasound (< 16 Hz) and the human low-frequency hearing regime (16 Hz to 256 Hz) and covers quasi-steady (0.125 Hz) to unsteady inertial flows for which the associated Womersley number is greater than unity (Table 2.1). The Womersley number α measures the ratio between the pulsatile or unsteady inertial forces in relation to the viscous forces [134]. We chose this frequency range for the following reasons. First, the low stimulation frequencies enable us to verify our results in quasi-steady-state scenarios with the known solutions of Bolinder [137]. Second, low frequencies are perceived in the apical region of the cochlea, which exhibits the strongest geometric curvature and torsion. Third, higher frequencies (> 256 Hz) require refined meshes due to steeper velocity gradients that would make the calculations prohibitively expensive.

Table 2.1. Model parameters. The viscosity and density are taken from water at 37°C (body temperature). The inlet pressure amplitude P_0 was chosen such that a desired mean velocity amplitude W_0 (averaged over the cross-section) was obtained.

Parameter	**Value**
Dynamic viscosity μ	0.69 mPa s [50]
Density ρ	993 kg/m^3 [50]
Hydraulic diameter d_h	2 mm [195]
Mean velocity amplitude W_0	$2 - 200$ µm/s [35, 40, 42]
Reynolds number $Re = d_h W_0 \rho / \mu$	$0.0058 - 0.58$
Oscillation frequency f	$0.125 - 256$ Hz
Womersley number $\alpha = \frac{d_h}{2}\sqrt{2\pi f \rho / \mu}$	$1 - 48$
Strouhal number $St = \frac{2\alpha^2}{\pi Re} = \frac{f d_h}{W_0}$	$1.25 - 256000$

Numerical model

For the simulations, we used the finite element solver COMSOL Multiphysics® (COMSOL AB, Stockholm, Sweden). Structured meshes were generated by sweeping a square cross-section (Fig. 2.2) along the ducts' centerlines. The cross-sectional mesh was aligned along the centerline with $\widehat{\mathbf{t}}$, $\widehat{\mathbf{n}}$, and $\widehat{\mathbf{b}}$. Grid stretching was applied. The number of nodes was chosen based on a convergence analysis, resulting in 26×26 nodes in the cross-section and a total of 77 500 hexahedral elements per geometry. We used Lagrange elements of order two and one for the velocity and pressure (P2P1), respectively. For the time-dependent solver, the implicit backward differentiation formula method of variable order (between 1 and 5) was used. We chose 100 steps per oscillation period of the pressure boundary condition. The

inlet pressure amplitude P_0 was found iteratively such that the axial velocity amplitude averaged over the cross-section W_0 remained the same across the stimulation frequency range for the different geometries. P_0 is approximately proportional to the oscillation frequency and to the Reynolds number. The Reynolds number measures the ratio between the inertial forces and the viscous forces [196].

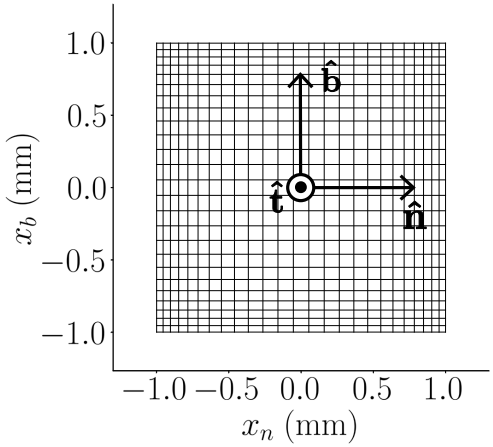

Fig. 2.2. Cross-sectional mesh with 26×26 nodes along the normal $\widehat{\mathbf{n}}$ and binormal $\widehat{\mathbf{b}}$ direction (Frenet-Serret frame).

Based on reported data [35, 40, 42], we chose three mean inlet velocity amplitudes averaged over the cross-section: 2 µm/s, 20 µm/s, and 200 µm/s. For a constant velocity amplitude W_0, decreasing frequencies correspond to increasing equivalent sound pressure levels at the ear drum. The characteristic middle ear transfer function (i.e., the stapes velocity versus the sound pressure at the ear drum) reaches its resonance at about 1 kHz, with a mean slope of approximately 6 dB per octave up to 1 kHz [35, 42]. For example, at 32 Hz, a stapes velocity of 200 µm/s can be expected for an external auditory canal pressure of $\sim$ 125 dB sound pressure level (SPL). At 128 Hz, the same stapes velocity would correspond to an acoustic stimulus with $\sim$ 113 dB SPL. Velocity amplitudes of 20 µm/s and 2 µm/s match pressure levels that are 20 dB and 40 dB lower, respectively. The selected stapes velocities approximately cover the range of sound pressure levels occurring during normal conversations (2 µm/s), shouted conversations (20 µm/s), and near to the threshold of pain at 256 Hz (200 µm/s). The selected parameters result in Reynolds numbers Re well below unity, implying that the fluid phenomena are in the Stokes regime. From the Womersley number and Reynolds number, one can also compute the Strouhal number, which is above unity in our case, see Table 2.1. The Strouhal number represents the ratio of the transient inertial forces due to unsteady acceleration to the inertial forces due to the advective acceleration [197].

To shorten the duration of the initial transient state, the amplitude of the inlet pressure P_0 was ramped up smoothly over the first few cycles. To ensure that the initial transient is washed out, we retrieved results after a sufficient number of cycles, e.g., after 21 cycles at 256 Hz. The results were evaluated at the central cross-section ($s = 5$) to exclude development length effects from the inlet and outlet boundary. We defined the maximum transverse flow velocities found in the straight duct simulations as the numerical noise

floor, which provides a lower bound on accuracy (see Fig. 2.6). The computations were performed on a computing cluster with AMD Epyc2 processors. The typical turnaround times for the computations that were running with 16 tasks and 32 GB RAM per CPU on one node varied from one day for 0.125 Hz, to seven days for 256 Hz.

Axial and transverse flow

We apply the Frenet-Serret frame to decompose the velocity field $\mathbf{u}$:

$$\mathbf{u} = u\widehat{\mathbf{n}} + v\widehat{\mathbf{b}} + w\widehat{\mathbf{t}}, \tag{2.6}$$

and define the velocity component along the tangent as axial flow $w = \mathbf{u} \cdot \widehat{\mathbf{t}}$, while the components in the normal and binormal directions, $u = \mathbf{u} \cdot \widehat{\mathbf{n}}$ and $v = \mathbf{u} \cdot \widehat{\mathbf{b}}$, constitute the transverse flow.

2.4 Results

Axial flow

Figure 2.3 shows the axial velocity contours in the geometries for different oscillation frequencies taken at the peak amplitude. For the straight duct, the results are in good agreement with the exact solution by Tsangaris & Vlachakis [141]. The relative velocity error, averaged in the cross-section, is 0.09% at 0.125 Hz and increases to 0.25% at 64 Hz and 1.25% at 256 Hz. It is known that Womersley flow develops steep velocity gradients with increasing Womersley numbers and that the thickness of the Stokes boundary layer scales with $1/\alpha$. We verified that the velocity gradient at the wall increases linearly with α in the straight duct for Womersley numbers greater than approximately 4. The axial velocity in the twisted duct hardly differs from the one in the straight duct (relative mean difference of 0.39%). Also, the flow profile in the helical ducts differ only little from the toroidal duct profiles (0.51%). Figure 2.4a shows the locations of the maximum axial flow in the cross-section for different frequencies and geometries. With increasing Womersley numbers α, these locations converge toward the corners in the straight and the twisted ducts. The maximum axial velocities in the toroidal and helical geometry are shifted to the inner wall corners for low Reynolds numbers and the present curvature, as also observed by Pantokratoras [198] and Murata et al. [128].

In the straight and twisted ducts, the axial velocity profile has a central symmetry with respect to the normal and binormal directions. The axial velocity profiles in toroidal ducts are symmetrical about the horizontal axis at $x_b = 0$, while in the helical duct a small deviation is introduced by the non-zero pitch.

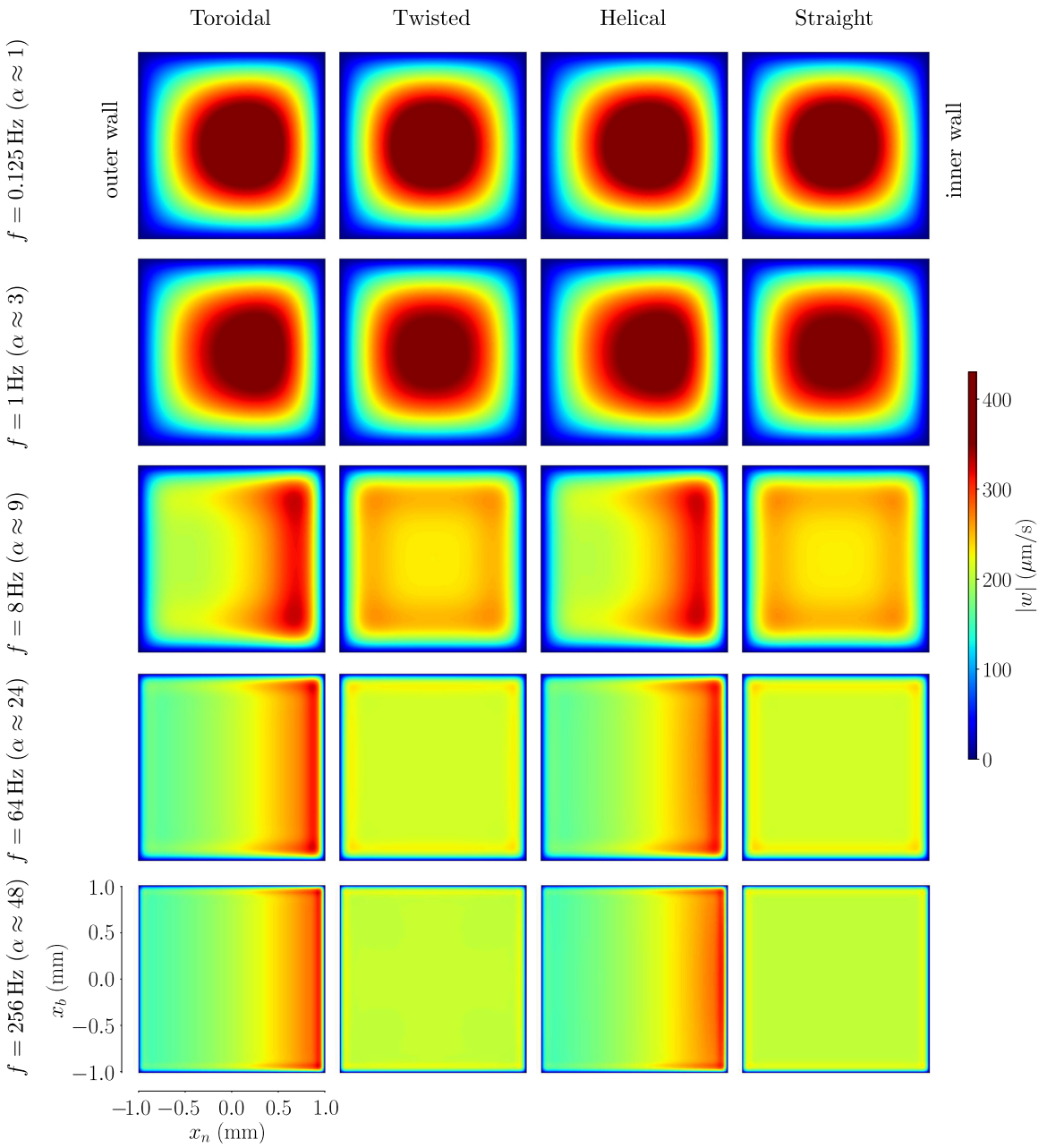

Fig. 2.3. Axial flow magnitude for different frequencies and geometries shown at the peak amplitude ($W_0 = 200\,\mu\mathrm{m/s}$).

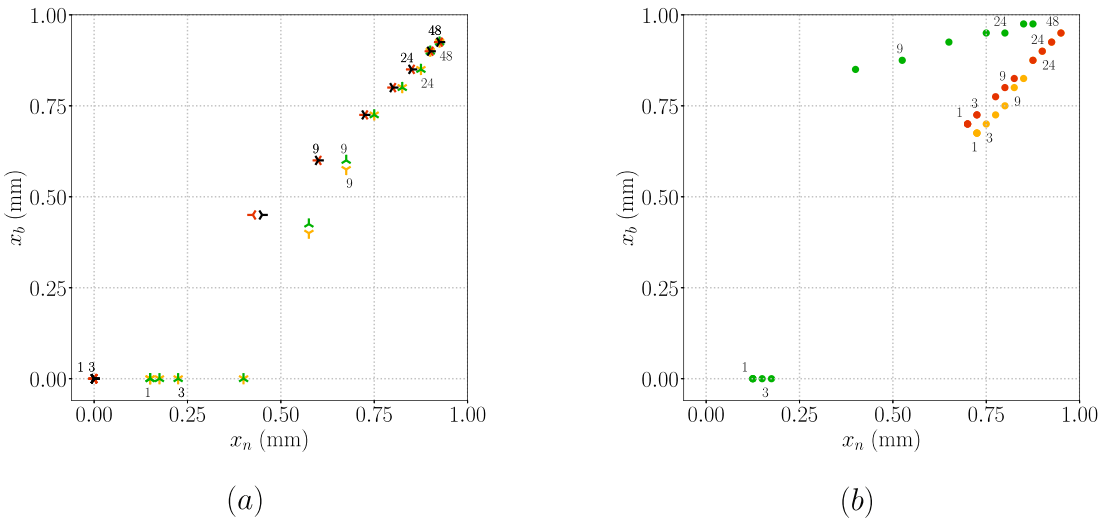

Fig. 2.4. Location of maximum axial (a) and transverse flow (b) in the toroidal (green), twisted (red), helical (yellow) and straight (black) ducts for Womersley numbers ranging from 1 to 48 and a mean velocity amplitude of $W_0 = 200\,\mu\text{m/s}$. Only the first quadrant of the cross-section is shown.

Transverse flow

Figure 2.5 shows transverse flow patterns for selected oscillation frequencies (additional figures are provided in the Supplemental Material at [URL will be inserted by publisher]). In the quasi-steady situation (i.e., 0.125 Hz), we found similar patterns as described by Bolinder [137], who studied transverse flow in steady conditions. In a pipe with circular cross-section, in contrast, Zabielski & Mestel [130] found a one-vortex structure in the cross flow of steady helical flows at low Reynolds numbers.

In the toroidal duct, two counter-rotating Dean cells form, caused by inertial forces that push the fluid along the middle line ($x_b = 0$) from the inner towards the outer wall [136]. This effect leads to unidirectional transverse flow, regardless of the direction of the axial flow. As the oscillation frequency increases, the Dean cells separate and concentrate on the walls. At 32 Hz ($\alpha \approx 17$) and higher frequencies, an additional pair of vortices, called Lyne instabilities, can be observed in the center of the channel, rotating opposite to the Dean cells [139].

The torsion of the twisted duct causes saddle flow in the corners of the cross-section, alternating with the direction of the axial flow. The observed pattern stays relatively stable over the simulated frequency range. The transverse flow pattern in the helical duct shows a similar structure as in the twisted duct, except that the transverse flow is focussed toward the inner wall, where the axial flow is stronger as well.

In general, for all geometries, the location of the maximum transverse flow approaches the corners (of the inner wall, in helical and toroidal ducts) for increasing Womersley numbers (Fig. 2.4b). In toroidal ducts, the maximum transverse flow has a sharp spatial transition from near the center of the cross-section to the upper and lower walls at $\alpha \approx 5.5$.

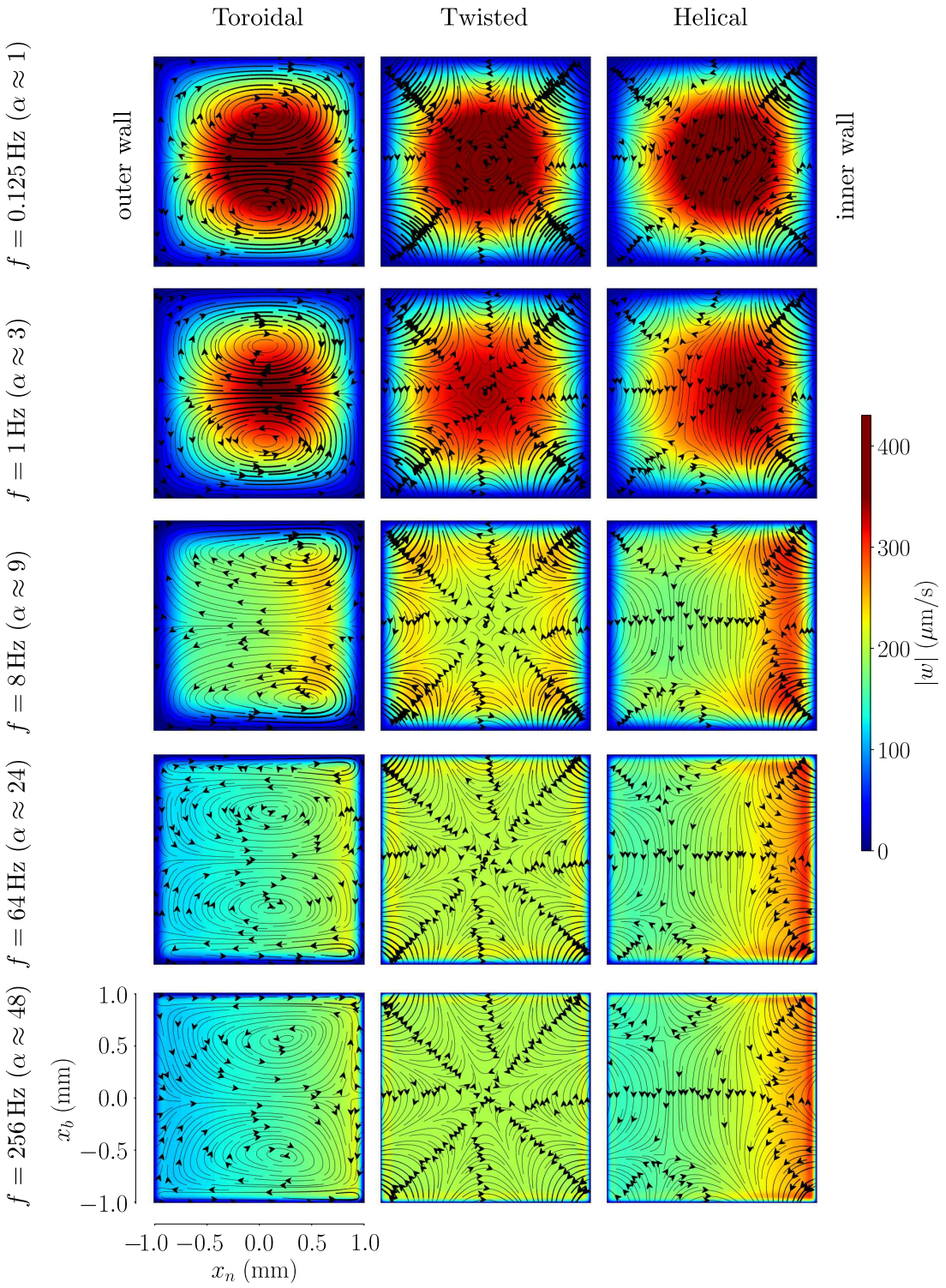

Fig. 2.5. Axial (colored contours) and transverse flow (streamlines) for different frequencies and geometries shown at the time of maximum transverse flow ($W_0 = 200\,\mu\mathrm{m/s}$). Looking into the page plane, the twisted duct turns clockwise and the axial velocity is inflowing.

This discontinuous change is a characteristic of the maximum function, which may jump between different local maxima in the cross-section. For Womersley numbers greater than approximately 5.5 the local maxima closer to the side walls become higher than the central one. Figure 2.6 summarizes the maximum transverse velocity magnitude versus Womersley number in our geometries. As expected for the toroidal duct, the transverse flow magnitudes because of curvature are small compared to the axial velocity (below 1% of the axial velocity magnitude). This is because the magnitude of the transverse flow in a toroidal duct is proportional to Re^2 [137]. Increasing the oscillation frequency further reduces the relative magnitude of the transverse flow which scales roughly with f^{-1} (or α^{-2}). As the Womersley number increases, the contribution of curvature to the transverse flow continues to decrease and approaches negligible amplitudes in the toroidal duct.

As pointed out by Bolinder [137] for steady flow at low Reynolds numbers, torsion has a dominating effect on transverse flow, which can be seen by a 5-fold higher maximum transverse flow magnitude in the quasi-steady state (i.e., 0.125 Hz). Strikingly, in contrast to curvature, the contribution of torsion is substantial and gets more significant with increasing frequencies following approximately $\ln(\alpha)$, with the relative maximum exceeding 10% of the axial flow magnitude for Womersley numbers greater than 10. At 256 Hz ($\alpha \approx 48$), the maximum transverse flow velocity accounts for approximately 15% of the axial flow velocity.

For the twisted duct, the curves for the different Reynolds numbers are coinciding in Fig. 2.6. This agrees with Bolinder [137] who found that the magnitude of transverse flow scales to first order with Re in such geometries. Also for the helical duct the curves for different Re coincide, indicating that the maximum transverse flow remains proportional to Re, at least in the frequency range observed in our experiments.

Surprisingly, although the contribution of curvature alone is negligible in the toroidal duct, the combination of curvature with torsion results in a 2-fold gain of transverse flow magnitude in the helical duct. This gain can be observed throughout the simulated frequency range, even for cases with $\alpha > 10$, where the isolated contribution of curvature to the transverse flow is less than 0.1% of the axial flow magnitude.

Phase lag

Figure 2.7 shows the phase difference between the flow and pressure oscillations. As the phase depends on the location within the cross-section, the reported values are shown at the maximum amplitudes for the axial (Fig. 2.4a) and transverse flow (Fig. 2.4b). The axial velocity phase lag in the straight duct is in good agreement with the exact solution by Tsangaris & Vlachakis [141]. The axial phase lag in the twisted duct resembles the one in straight ducts (relative difference of 0.15%), reaching a plateau at a quarter of a cycle for $\alpha > 4$. In the toroidal and helical ducts, the phase lag is similar but on average higher than in the straight and twisted ducts.

The phase lag of the transverse flow velocity decreases monotonically in all geometries and approaches the phase lag of the axial flow velocity with increasing Womersley numbers, except for the toroidal duct. In the toroidal duct the phase lag fluctuates around a third of a cycle for $\alpha > 4$.

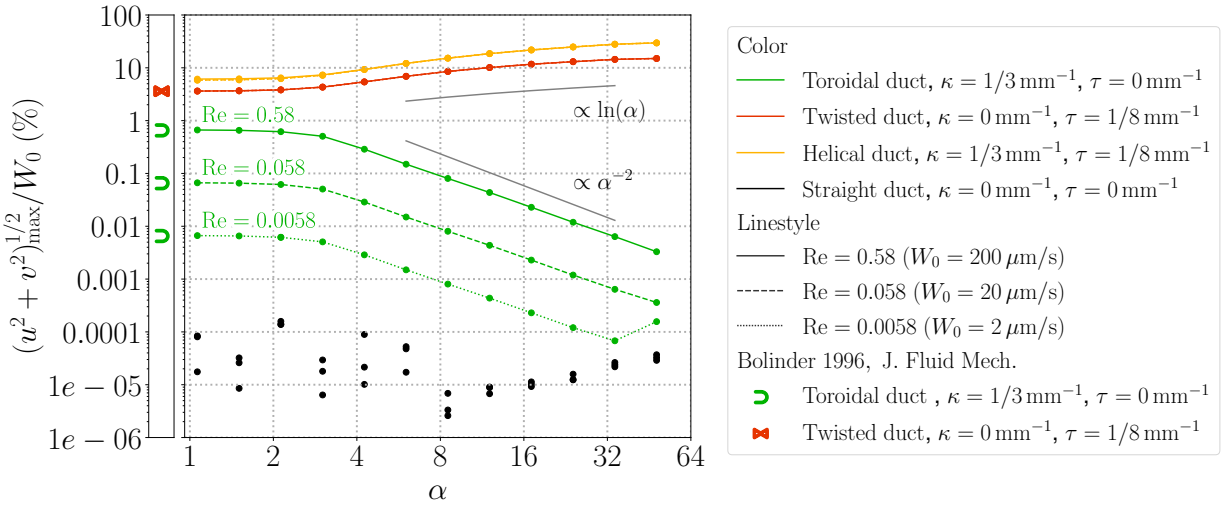

Fig. 2.6. Maximum transverse flow magnitude with respect to the mean axial flow velocity (W_0) as a function of the Womersley number α. The markers on the left side of the figure show the steady flow solutions for the toroidal and twisted ducts [137]. Black symbols indicate numerical noise defined as the maximum transverse flow velocities found in the straight duct simulations. Note that the maximum transverse flow at $\alpha \approx 48$ ($f = 256\,\mathrm{Hz}$) and $Re = 0.0058$ in the toroidal duct is distorted due to its proximity to the numerical noise floor.

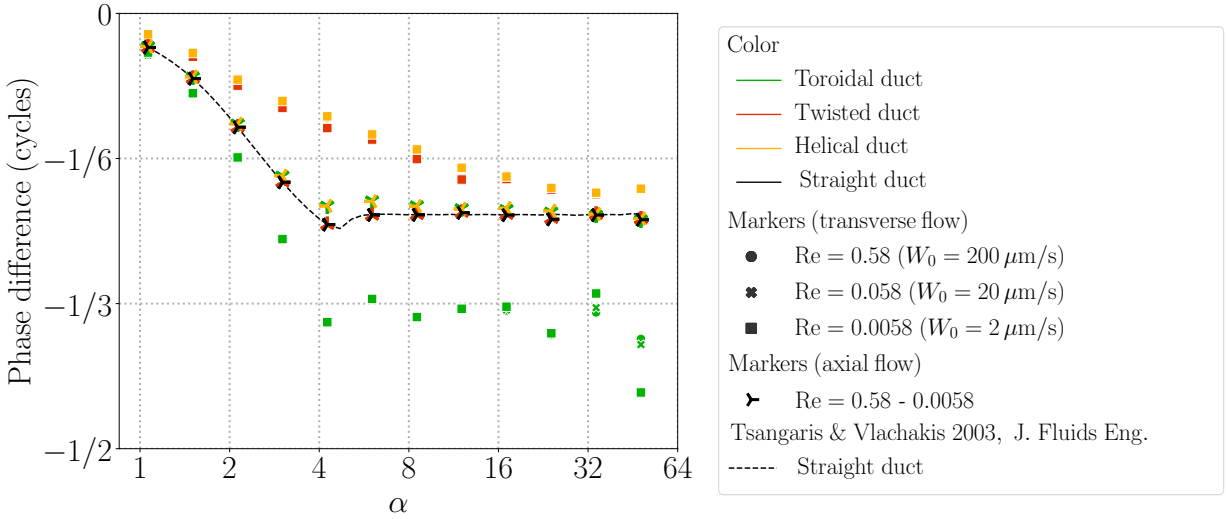

Fig. 2.7. Phase difference between maximum axial (trilateral markers) and transverse flow velocity (marker style according to the Reynolds number) and pressure for different Womersley numbers α. The black dashed line indicates the exact solution (phase lag between the axial flow and pressure) for a straight square duct [141]. Markers for different Reynolds numbers Re coincide. For the toroidal duct, the phase difference is distorted at $\alpha \approx 48$ ($f = 256\,\mathrm{Hz}$) and $Re = 0.0058$ due to the numerical noise floor.

2.5 Discussion

Transverse flow

In this study, we used simplified geometries to investigate the effects of curvature and torsion on transverse flow under oscillatory stimulation based on conditions in the human cochlea. Our models, which have square cross-sections and do not include fluid interactions with flexible membranes, serve as abstract representations of the cochlear scalae. Through our simulations, we discovered two key findings about the influence of geometry on transverse flow.

First, we found that torsion remains a significant contributor to transverse flow in unsteady conditions at low Reynolds numbers (< 1), as pointed out by Bolinder [137] for steady flow, and its contribution increases with higher oscillation frequencies. The formation of saddle flow due to torsion could be interpreted as a kinematic effect, as the twisted geometry forces a change of direction close to the boundaries.

Second, we observed that the combined effect of curvature and torsion on transverse flow is greater than what would be expected based on a simple combination of the two effects, especially when the relative contribution of curvature alone becomes negligible. The transverse velocities resulting from curvature are about one order of magnitude smaller than found from torsion, and decrease rapidly for increasing frequencies. The transverse flow patterns are similar between the twisted and the helical ducts (Fig. 2.5), however, caused by curvature, the maximum axial velocity gets shifted toward the corners of the inner duct wall in helical ducts (Fig. 2.4b), leading to stronger saddle flow there. Therefore, it appears as if the helical shape acts as an amplifier to transverse flow when stimulated with oscillations within the observed frequency range.

Axial flow

The straight and twisted ducts have nearly identical axial flow profiles in our simulations. This is in agreement with Kheshgi [132] who found that the axial flow profile in twisted channels approximates the velocity profile of a straight channel under steady conditions and low torsion. As soon curvature is present (i.e., in toroidal and helical ducts), the axial flow profiles are dominated by curvature over the observed frequencies. At low Reynolds numbers and high curvature, the maximum velocity is shifted towards the inner wall of the bend, contrary to what one would expect for higher Reynolds numbers [128, 198]. The axial pressure gradient is steeper along the inner wall because the arc length is shorter than at the outer wall. Since the centrifugal forces which push the fluid outwards are weak at low Dean numbers, we suspect that the effect of the higher pressure gradient dominates such that the highest velocities are found closer to the inner wall [199]. With increasing Womersley numbers, the maximum flow velocity moves closer to the inner wall. In the toroidal and helical geometry, the position of the maximum axial flow abruptly shifts from the middle line (along $x_b = 0$) towards the corners of the inner walls as α exceeds approximately 4.5. This sudden change reflects the transition from a low Womersley number regime, which is characterized by viscous inertial forces, to a regime where transient pulsatile forces dominate. Consequently, the velocity profile changes from a quasi-stationary, parabolic

shape to a Womersley flow exhibiting four local maxima close to the corners. In our geometries, torsion of the helical duct (or the resulting pitch) has little effect on the axial flow compared to the toroidal duct.

Phase lag

We found that the phase difference depends on the duct geometry for transverse flow and behaves differently than the phase difference between th pressure and axial flow velocity. In toroidal ducts, the axial and transverse flow velocities can be considered in-phase when approaching higher frequencies, with a quarter of a cycle offset to the pressure amplitude. The difference in the axial phase lag between the geometries with a straight centerline and the ones with a curved can be explained by the different probing locations, which were closer to the walls for helical and toroidal ducts (Fig. 2.4a). Also the fluctuations in the transverse phase lag in the toroidal duct for $\alpha > 4$ likely result from the change in the probing locations with increasing Womersley numbers (Fig. 2.4b).

Study limitations

The main limitation of our study is the use of abstract geometries to model the highly complex anatomy of the human cochlea [112]. Our largely simplified models do not capture important phenomena such as the travelling wave inside the cochlea or its tonotopic organization. Further studies on models featuring more realistic cross-sections and tapering, and in particular fluid-membrane interactions, are required to investigate possible implications on cochlear mechanics. Our simulations are limited to the observed frequency range, which only covers the low-frequency hearing regime of humans. Additional simulations, with refined mesh geometries, are required to obtain data covering the whole human hearing range up to 16 kHz and more.

2.6 Acknowledgements

We would like to thank Prof. Nathaniel Greene, University of Colorado, for providing middle ear transfer function data. We acknowledge the support from the Swiss National Science Foundation (Grant No. 205321_200850). Calculations were performed on UBELIX (www.id.unibe.ch/hpc), the HPC cluster at the University of Bern.

2.7 Supplement

The Supplemental Material includes transverse flow patterns at other Womersley numbers, simulation results where the viscosity and length scale were varied, and additional information about the methods described in the main article.

Transverse flow patterns

Fig. 2.8 and 2.9 show the transverse flow patterns for the remaining Womersley numbers α, which were not presented in the main article.

Viscosity and length scale variations

The maximal transverse velocities depend only on the Reynolds number Re in the steady case (for a fixed torsion and curvature) [137]. In our unsteady scenario, they changed additionally with the oscillation frequency. To verify that the Womersley number is the correct dependent variable (e.g., in Fig. 6 in the main article), we performed additional simulations with a dynamic viscosity of 2μ ($Re = 0.29$) and simulations with a length scale of $2l_0$ ($Re = 1.16$), where l_0 refers to the initial length dimension. We kept the mean velocity amplitude at 200 µm/s, and, consequently, the Reynolds number changed according to the length scale and viscosity. Figure 2.10 shows the maximal relative transverse velocities resulting from these variations as a function of the Womersley number. In the toroidal duct, the transverse velocity magnitude decreased linearly with Re while in the twisted duct, the magnitude remained constant for different Reynolds numbers. The different lines visible in Fig. 2.10a (and in Fig. 6 in the main article) for the toroidal geometry collapse to one line when the y-axis is divided additionally by the Reynolds numbers (Fig. 2.10b). Other changes in the maximal transverse velocity have not been observed by changing the viscosity or the length scale.

Method supplement

Grid stretching

The cross-section mesh consists of N nodes aligned along $\widehat{\mathbf{n}}$ and $\widehat{\mathbf{b}}$, respectively. For the direction in $\widehat{\mathbf{n}}$, the node coordinates x_n (in mm) at index j are

$$x_n^{(j)} = \frac{\tanh\left[-\pi/3 + 2\pi j/(3N)\right]}{|\tanh(\pi/3)|}\frac{d_h}{2}, \quad \text{with} \quad j = 0, 1, ..., N. \tag{2.7}$$

$d_h = 2\,\text{mm}$ is the side length of the cross-section. The node coordinates $x_b^{(j)}$ along $\widehat{\mathbf{b}}$ are distributed analogously.

For the applied mesh with $N = 26$, 125 nodes were uniformly distributed along the centerline (i.e., in the $\widehat{\mathbf{t}}$-direction), leading to a spacing of $s_{max}/124$.

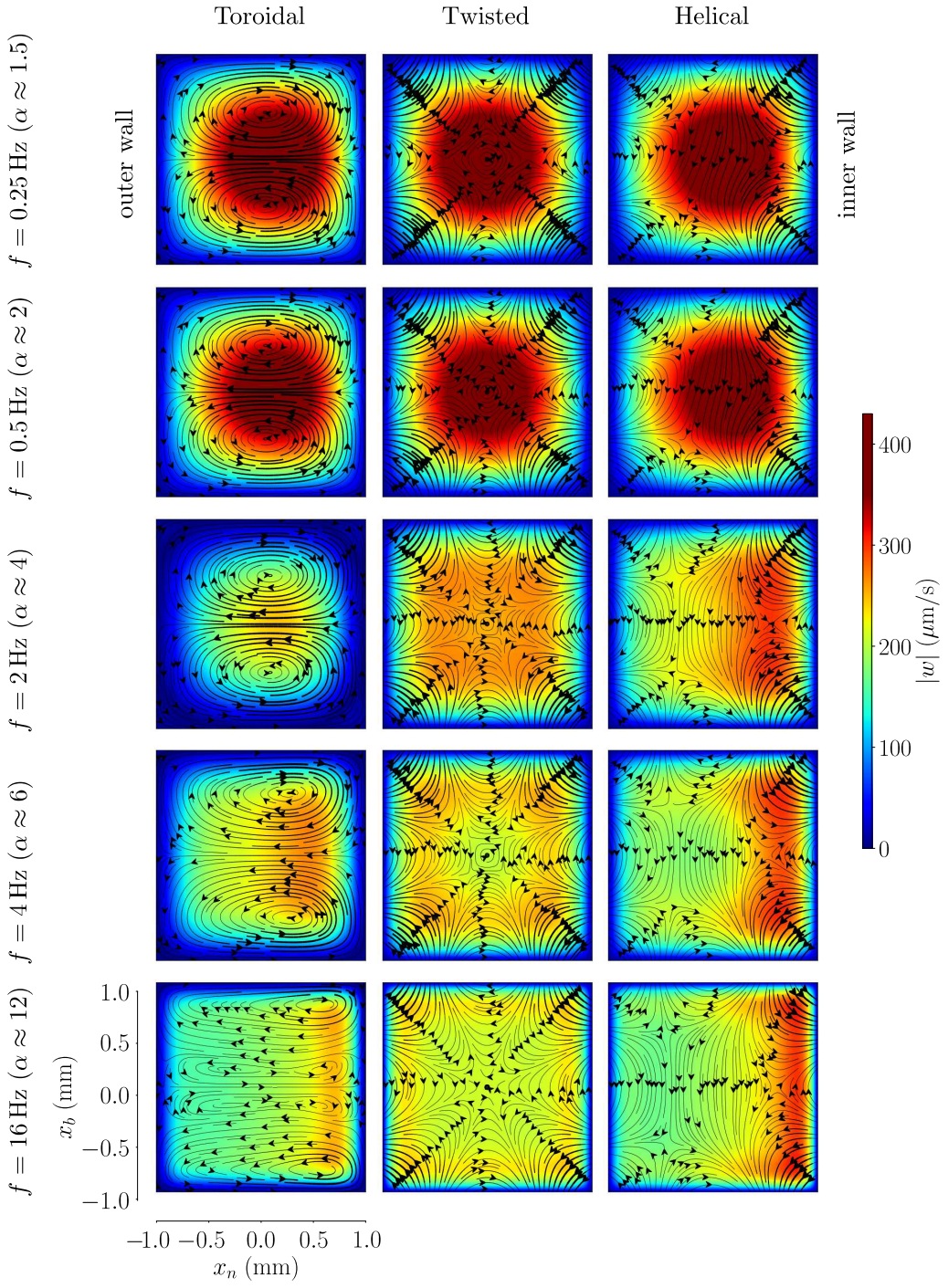

Fig. 2.8. Axial (colored contours) and transverse flow (streamlines) for different oscillation frequencies and geometries shown at the time of maximum transverse flow for a mean inlet velocity $W_0 = 200\,\mu\mathrm{m/s}$. Looking into the page plane, the twisted duct turns clockwise and the axial velocity is inflowing.

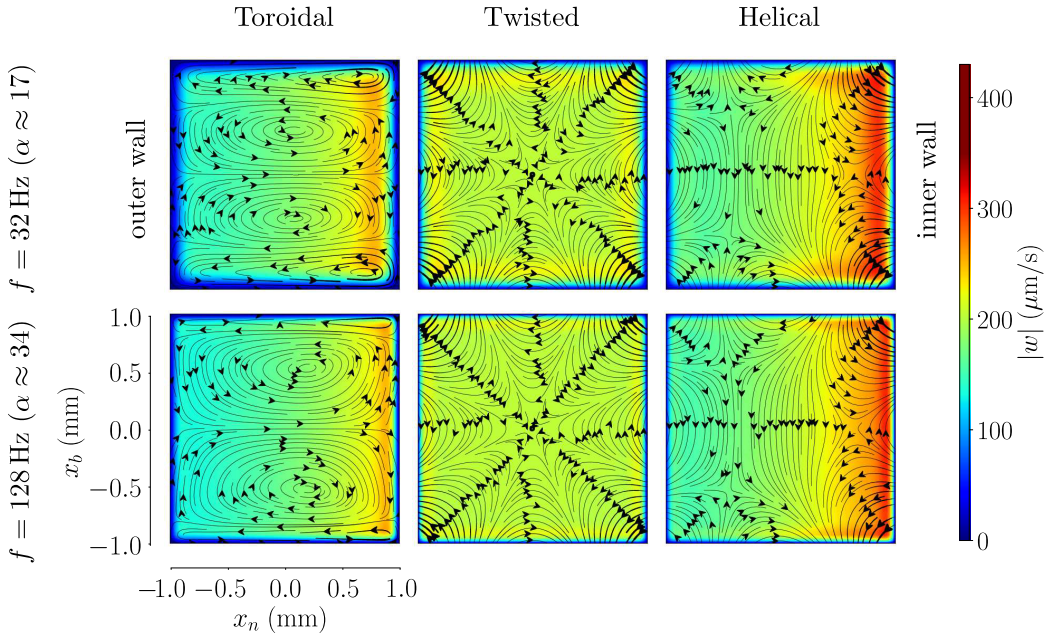

Fig. 2.9. Axial (colored contours) and transverse flow (streamlines) for different oscillation frequencies and geometries shown at the time of maximum transverse flow for a mean inlet velocity $W_0 = 200\,\mu\mathrm{m/s}$. Looking into the page plane, the twisted duct turns clockwise and the axial velocity is inflowing.

Verification of transverse velocities in steady conditions

To further verify the mesh and CFD settings, we conducted stationary simulations and compared the results with literature. According to Bolinder [137], the ratio of the maximal transverse velocities with respect to the mean axial velocity for a toroidal duct with curvature κ is given by

$$\frac{(\mathbf{u}^2 + \mathbf{v}^2)^{1/2}_{max}}{W_0} = 0.017 \kappa d_h Re, \tag{2.8}$$

and for a twisted duct with torsion τ by

$$\frac{(\mathbf{u}^2 + \mathbf{v}^2)^{1/2}_{max}}{W_0} = 0.144 \tau d_h, \tag{2.9}$$

where Re is the Reynolds number. Figure 2.11 shows the maximum transverse velocities in curved and twisted ducts for steady flows as a function of the Re. They are in good agreement with the results obtained by Bolinder [137]. The average relative difference of 2.4% can be explained by the fact that he included only terms up to first-order of a perturbation series in curvature and torsion (for said equations).

Simulation times

Table 2.2 lists the total simulation time and the duration over which the amplitude of the oscillating inlet pressure was ramped up. For frequencies above 8 Hz, the simulation time

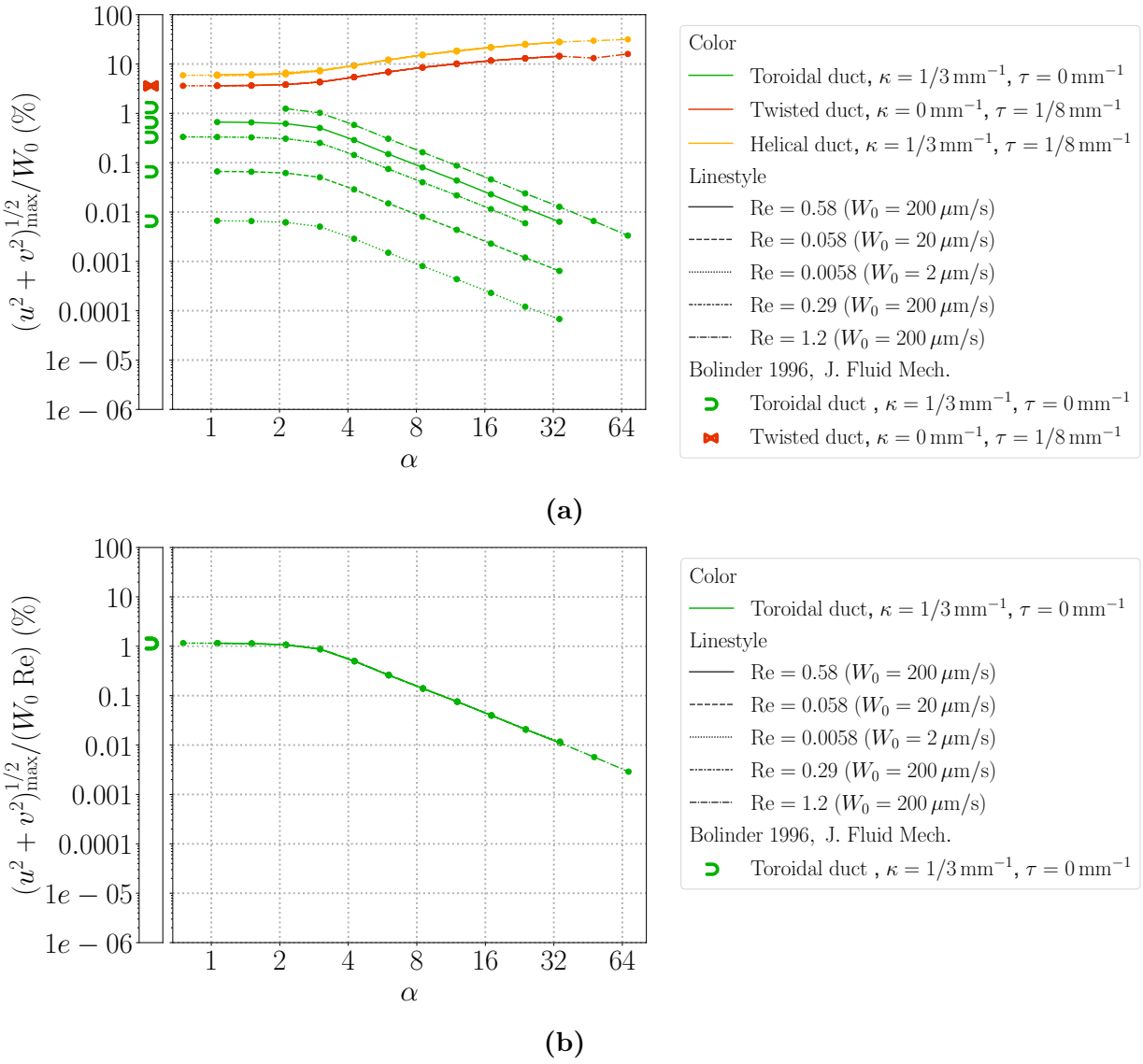

(a)

(b)

Fig. 2.10. Maximal transverse flow magnitude as a function of the Womersley number α; a with respect to the mean axial flow amplitude, and b with respect to the mean axial flow amplitude and divided by the Reynolds number. Line styles mark different mean axial flow velocities W_0 and Reynolds numbers. Note that the lines coincide per geometry, if scaled accordingly. The markers on the left side of the figure indicate the steady state solutions of Bolinder [137] for toroidal and twisted ducts.

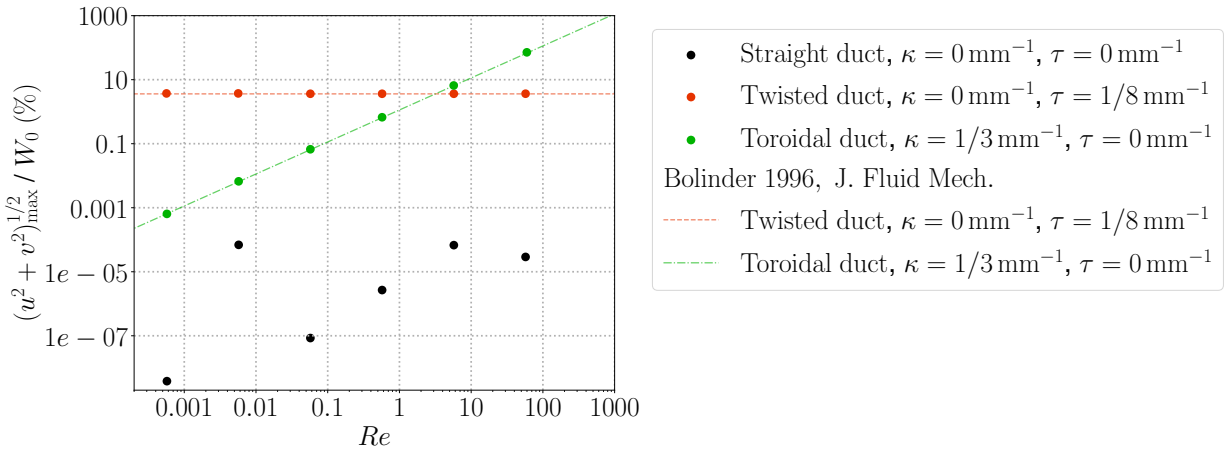

Fig. 2.11. Maximal transverse velocities with respect to the axial velocity versus the Reynolds number. Lines show first-order results by Bolinder [137] and dots our results.

amounted to 25 cycles, and the oscillating inlet pressure was ramped up over the first ten cycles with a smoothed step function. For each frequency, we used the last four cycles for post-processing.

Table 2.2. Simulation time T in cycles of the stimulation frequency f, and number of cycles T_p over which the pressure amplitude was ramped up.

f (Hz)	T (cycles)	T_p (cycles)
≤ 1	8	1
2	12	2
4	14	4
8	20	10
≥ 16	25	10

CHAPTER 3

WALL SHEAR STRESS AND PRESSURE FLUCTUATIONS UNDER OSCILLATING STIMULATION IN HELICAL SQUARE DUCTS WITH COCHLEA-LIKE GEOMETRICAL CURVATURE AND TORSION

This chapter is published as:
Harte N.C., Obrist D., Caversaccio M.D., Lajoinie G.P.R. and Wimmer W. Wall shear stress and pressure fluctuations under oscillating stimulation in helical square ducts with cochlea-like geometrical curvature and torsion. 45th Annual International Conference of the IEEE Engineering in Medicine & Biology Society (EMBC), 2023, Sydney, Australia.
doi: 10.1109/EMBC40787.2023.10340844.

Wall shear stresses and pressure fluctuations in a toroidal, a twisted, and a helical square ducts are presented. A decomposition of the wall shear stress into an axial and a transverse component is performed, based on the duct centerline and local wall normal. The combination of curvature and torsion is shown to cause higher wall shear stresses than either curvature or torsion alone.

Author contribution: Conceptualization and methodology, numerical simulations, data analysis, manuscript writing and data visualization.

3.1 Abstract

Our study aims to provide basic insights on the impact of the spiral shape of the cochlea, i.e., of geometric torsion and curvature, on wall pressure and wall shear stress. We employed computational fluid dynamics in square duct models with curvature and torsion similar to those found in human cochleae. The results include wall pressures and wall shear stresses within the ducts under oscillating axial flow. Our findings indicate that the helical shape generates higher transverse wall shear stresses compared to exclusively curved or twisted ducts. The wall pressures and transverse wall shear stresses we found rise to amounts that may be physiologically relevant in the cochlea.

Clinical relevance — The role of the spiral shape of the cochlea in hearing physiology remains, for a large part, elusive. For a better apprehension of hearing and its disorders, it is important to investigate the influence of geometric properties on biofluids motion and emerging phenomena in the cochlea.

3.2 Introduction

The cochlea, our organ of hearing, is a fluid-filled spiral structure that is small and difficult to access. Because direct experimental observations are limited, our understanding of hearing physiology remains partial. One unresolved question is that of the role and relevance of the cochlear morphology for hearing. In particular, the consequence of transverse flows on the shear flow along membranes has so far not been considered. In this study, we aim to quantify the effects of geometric curvature and torsion on wall shear stress and pressure fluctuations in abstracted models with cochlea-like geometric properties. In toroidal, twisted, and helical ducts, curvature and torsion cause transverse flow phenomena [137], [200], which further generate local pressure fluctuations and wall shear stresses [152, 168]. Using computational fluid dynamics, we simulated flow at oscillation frequencies covering the infrasonic regime and the low-frequency hearing range of humans, for which the apical region of the cochlea (the region with the highest curvature and torsion) is particularly sensitive.

The cochlea contains thin membranes, such as the basilar membrane (housing the sensory epithelium) and the Reissner's membrane (only consisting of two cell layers) [201]. Wall shear stress and pressure fluctuations caused by transverse flow could locally deflect these membranes. Our results could help to provide insights on the relevance of morphology for hearing.

3.3 Methods

Duct geometries

We have simulated fluid flow in straight, toroidal, twisted and helical geometries to independently characterize the impact of curvature and torsion on pressure fluctuations and wall shear stress (see top row in Fig. 3.1). The geometries were constructed using established methods [137] with centerline curvature $\kappa = 1/3\,\mathrm{mm}^{-1}$ and torsion $\tau = 1/8\,\mathrm{mm}^{-1}$. These values approximate those measured in human cochleae [133]. To save computational resources, we chose a total arc length of the centerline of 10 mm for all models, which is shorter than a human cochlea (37 mm) [194]. The models' cross-section measures $2\,\mathrm{mm} \times 2\,\mathrm{mm}$ to capture typical dimensions of the cochlea [195].

Wall pressure and wall shear stress

The Cauchy stress tensor T is given by

$$\mathsf{T} = -p\mathsf{I} + \mathsf{S}, \tag{3.1}$$

where S is the viscous stress tensor, p is the pressure and I is the identity tensor [202]. We subtract the mean pressure $\bar{p}$ over the cross-section from the total pressure to obtain pressure fluctuations p_{fluc}:

$$p_{fluc}(x, y, z, t) = p(x, y, z, t) - \bar{p}(t). \tag{3.2}$$

S is computed using the symmetric part of the velocity gradient

$$\mathsf{S} = \mu[\nabla\mathbf{u} + (\nabla\mathbf{u})^T], \tag{3.3}$$

where $\mathbf{u} = \mathbf{u}(x, y, z, t)$ is the velocity field at a time t. The viscous stress $\boldsymbol{\tau}_w$ exerted by the fluid on a wall element with unit surface normal vector $\widehat{\mathbf{s}}_n$ (pointing into the fluid domain) is

$$\boldsymbol{\tau}_w = \mathsf{S}\widehat{\mathbf{s}}_n. \tag{3.4}$$

We can further decompose the viscous stress into an axial and a transverse component. We define the transverse component $\widehat{\mathbf{s}}_{tr}$ as orthogonal to $\widehat{\mathbf{s}}_n$ and to the duct centerline's tangent $\widehat{\mathbf{t}}$:

$$\mathbf{s}_{tr} = \widehat{\mathbf{s}}_n \times \widehat{\mathbf{t}} \quad \text{and} \quad \widehat{\mathbf{s}}_{tr} = \mathbf{s}_{tr}/\|\mathbf{s}_{tr}\|. \tag{3.5}$$

The local wall element coordinate system is then defined by $(\widehat{\mathbf{s}}_{ax}, \widehat{\mathbf{s}}_{tr}, \widehat{\mathbf{s}}_n)$, with the direction of the axial component given by

$$\widehat{\mathbf{s}}_{ax} = \widehat{\mathbf{s}}_{tr} \times \widehat{\mathbf{s}}_n. \tag{3.6}$$

Since $\boldsymbol{\tau}_w$ is perpendicular to $\widehat{\mathbf{s}}_n$, we use the two-dimensional decomposition of the stress:

$$\boldsymbol{\tau}_w = \tau_{w,ax}\widehat{\mathbf{s}}_{ax} + \tau_{w,tr}\widehat{\mathbf{s}}_{tr}, \tag{3.7}$$

with axial wall shear stress $\tau_{w,ax} = \boldsymbol{\tau}_w \cdot \widehat{\mathbf{s}}_{ax}$ and the transverse wall shear stress $\tau_{w,tr} = \boldsymbol{\tau}_w \cdot \widehat{\mathbf{s}}_{tr}$.

Model implementation and numerical model

The perilymph fluid in the cochlea is modelled as a Newtonian fluid and the flow is considered incompressible (low Mach number) [50]. We used a sinusoidal pressure boundary condition at the inlet and zero pressure at the outlet surface. The oscillation frequency f ranged from 0.125 Hz to 256 Hz (the human hearing range starts at 16 Hz). The associated Womersley numbers are $\alpha = \frac{d_h}{2}\sqrt{2\pi f\rho/\mu} = 1$ to 48, and thus cover quasi-steady to unsteady inertial flows (hydraulic diameter $d_h = 2\,\text{mm}$, dynamic viscosity and density of water at body temperature $\mu = 0.69\,\text{mPa s}$ and $\rho = 993\,\text{kg/m}^3$ [50]).

For the simulations, we used the finite element solver COMSOL Multiphysics® (COMSOL AB, Stockholm, Sweden). The meshes consist of 77 500 hexahedral elements per geometry, with ensured convergence. We determined the inlet pressure amplitude iteratively such that the axial velocity amplitude averaged over the cross-section W_0 remained 200 µm/s across the stimulation frequency range [35, 40]. The resulting Reynolds number is $Re = d_h W_0 \rho/\mu = 0.58$, implying that the fluid phenomena are in the Stokes regime.

3.4 Results

Wall pressure

Fig. 3.1 shows the pressure fluctuations over time along the perimeter of a cross-section in the middle of the geometries.

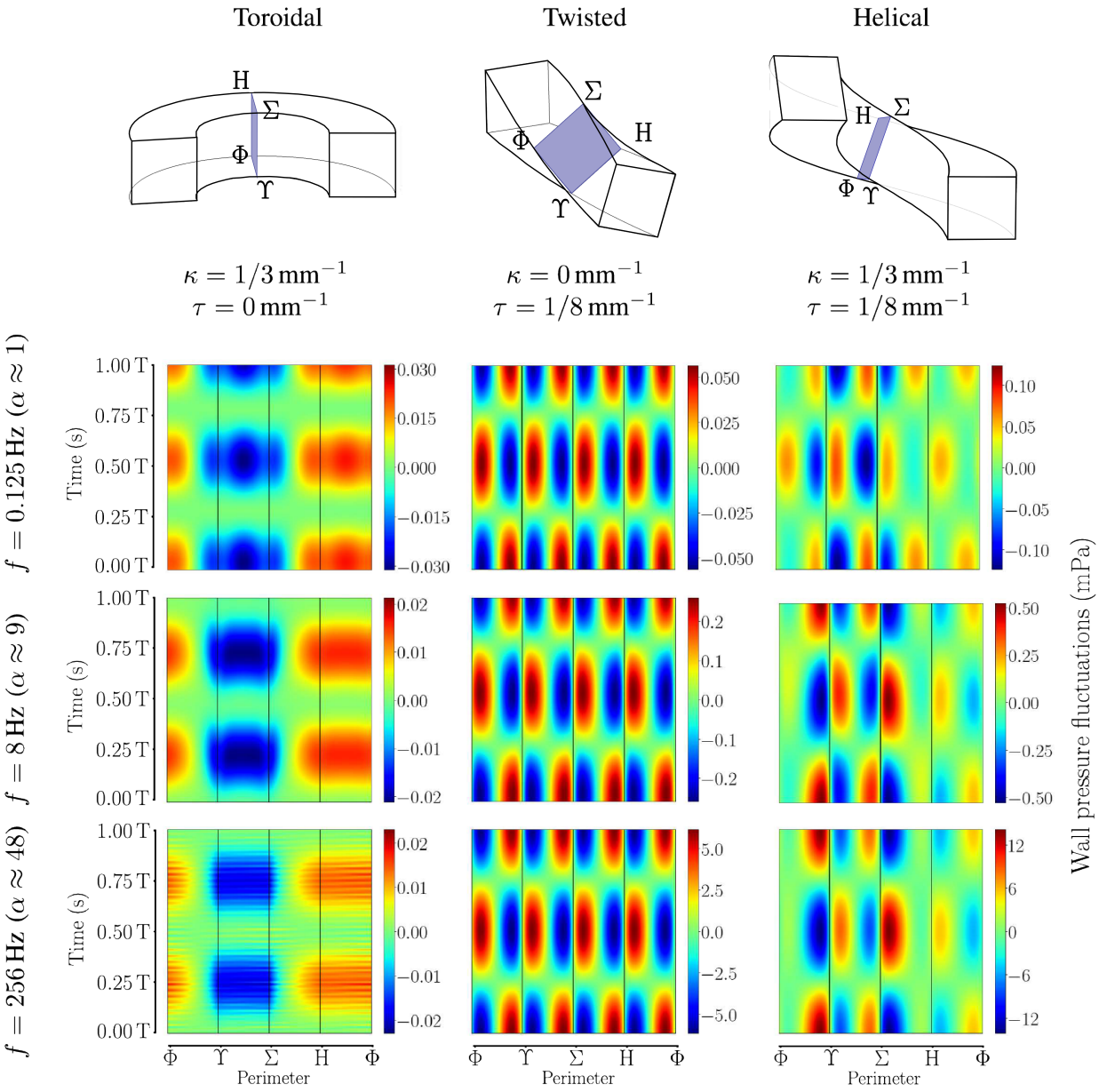

Fig. 3.1. Top row: Geometries with corresponding curvature κ and torsion τ. Greek capital letters indicate the corners of the central cross-section (shaded violet). Other rows: Pressure fluctuations along the perimeter of the central cross-section over time for different oscillation frequencies with period $T = 1/f$. Zero time in the plots corresponds to the time of maximum inlet pressure. Note that the pressure fluctuations at $\alpha \approx 48$ ($f = 256\,\mathrm{Hz}$) in the toroidal duct are distorted due to the proximity to the numerical noise floor (Fig. 3.2). The colorbars are scaled differently.

In the toroidal duct, a pressure gradient between the outer ($\mathrm{H} - \Phi$) and the inner wall ($\Upsilon - \Sigma$) of the duct can be observed as the result of fluid being pushed outwards. Notably, the pattern observed in toroidal ducts is unidirectional, i.e., it does not change with the direction of the axial flow. By contrast, in twisted ducts, the wall pressure changes according to the oscillation cycle of the axial flow. High wall pressure fluctuations arise in

the proximity of corners. This observation agrees with Kheshgi's findings for steady flows [132]. The pattern remains consistent over the entire range of observed frequencies.

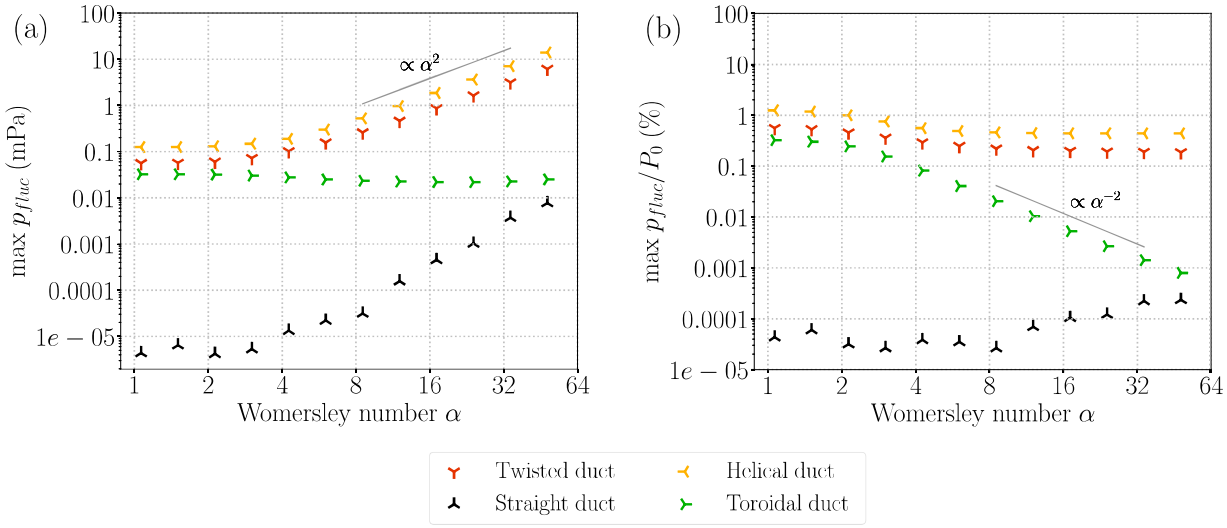

Fig. 3.2. Maximum wall pressure fluctuations p_{fluc} (a) and p_{fluc} with respect to the inlet pressure P_0 in percent (b), as a function of the Womersley number. The black symbols indicate numerical noise defined as the maximum wall pressure fluctuations found in the straight duct simulations.

In the helical duct, we recover a combination of the patterns observed in the toroidal and the twisted duct. At $\alpha \approx 1$, both contribute with comparable magnitudes, although the torsional effects dominate slightly. At higher α, however, the pressure fluctuations because of curvature decrease to negligible amounts. Notably, the pressure fluctuations reach greater magnitudes than the cumulative pressures observed in the other two ducts. The peak of the axial velocity is shifted toward the inner wall, because of the low Reynolds number and high curvature [198], and subsequently amplifies the pressure fluctuations near the inner wall.

Fig. 3.2a shows the maximum pressure fluctuation at the wall as a function of the Womersley number α. Since the inlet pressure amplitude P_0 was increased with the Womersley number to keep velocity amplitude W_0 the same, we examined the maximum pressure fluctuation with respect to P_0 in Fig. 3.2b. The maximum relative pressure fluctuations remain nearly constant for $\alpha => 24$ in the helical and twisted geometry, at a level of 0.4% and 0.2%, respectively. Surprisingly, the combination of curvature and torsion in the helical duct causes pressure fluctuations to increase more than twice as much as in the twisted duct, which has no curvature. In contrast, in the toroidal duct, the pressure maximum is most pronounced at low frequencies and located at the center of the outer wall, whereas at high frequencies, the peak becomes wider and is distributed along the entire side wall (Fig. 3.1). We observed that the fluctuations decrease with α^{-2} for Womersley numbers $\alpha => 9$.

Wall shear stress

Fig. 3.3 and 3.4 illustrate the evolution of the axial and transverse wall shear stresses along the perimeter of the central cross-section (see Fig. 3.1) over time. The lower y-axis limit corresponds to the time of maximum inlet pressure.

The axial wall shear stress (AWSS) increases by about one order of magnitude from 0.125 to 256 Hz in all geometries. Its direction changes with the axial flow direction. In the toroidal and helical ducts, the highest axial wall shear stresses are found at the inner wall of the geometry (ϒ - Σ) and are about 40% higher than in the twisted duct. For the AWSS it is the toroidal aspect of the geometry that dominates.

We define counterclockwise (Φ-ϒ-Σ-H-Φ) transverse wall shear stress (TWSS) as positive. By opposition to the AWSS, the patterns of the twisted duct dominate the TWSS in the helical duct. In the presence of torsion, strong TWSS emerges close to the corners, which increase and move closer to the corners for higher Womersley numbers. The highest TWSS can be observed in the helical duct close to the corners ϒ and Σ.

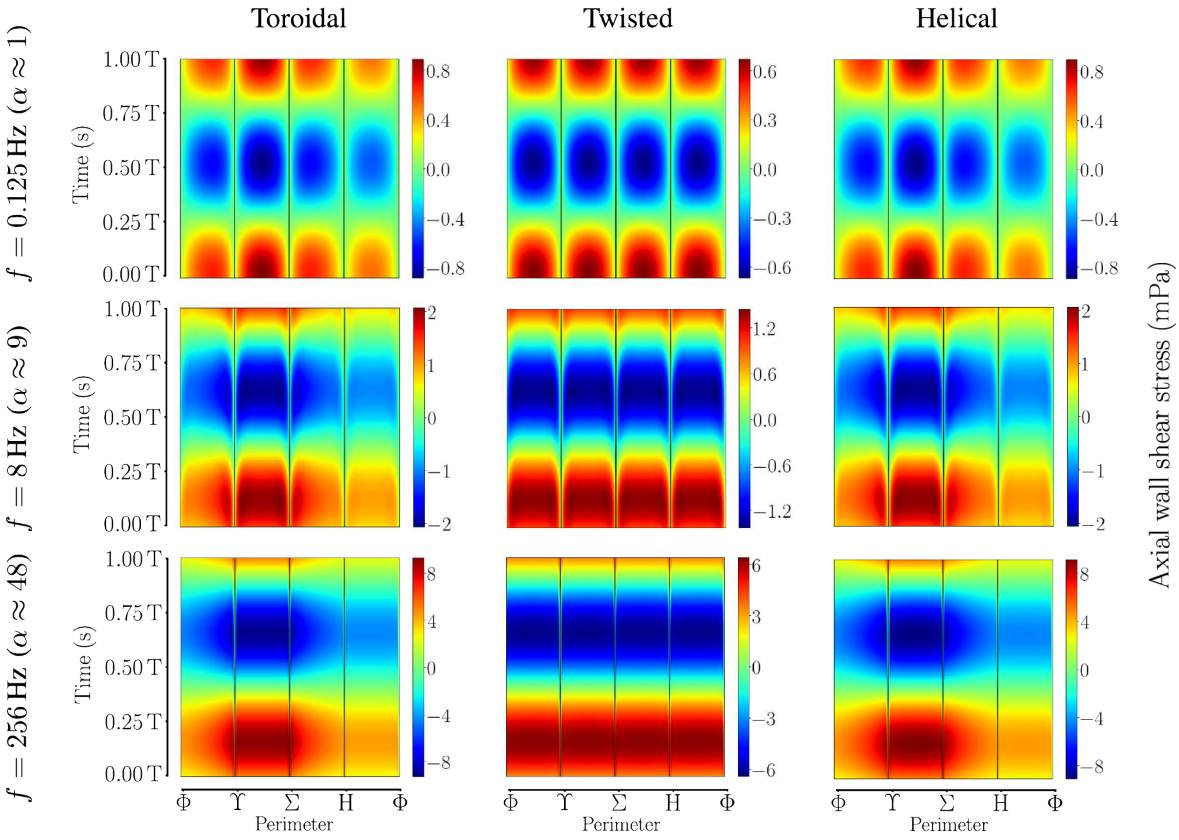

Fig. 3.3. Axial wall shear stress $\tau_{w,ax}$ visualized for different oscillation frequencies f along the perimeter of the central cross-section. One oscillation period ($T = 1/f$) is shown on the y-axis. Greek capital letters indicate the position along the perimeter. The colorbars are scaled differently.

Fig. 3.5 displays the ratio of the maximum transverse wall shear stress to the average axial wall shear stress as a function of the Womersley number α. We chose this ratio to quantify the deviation of shear stress from the axial direction, which could be relevant for transverse membrane deflections in the cochlea [61]. The maximum relative wall shear stress in the twisted and helical geometries increases up to 10% and 20%, respectively. Over the entire frequency range, the helical geometry exhibits approximately a two-fold increase

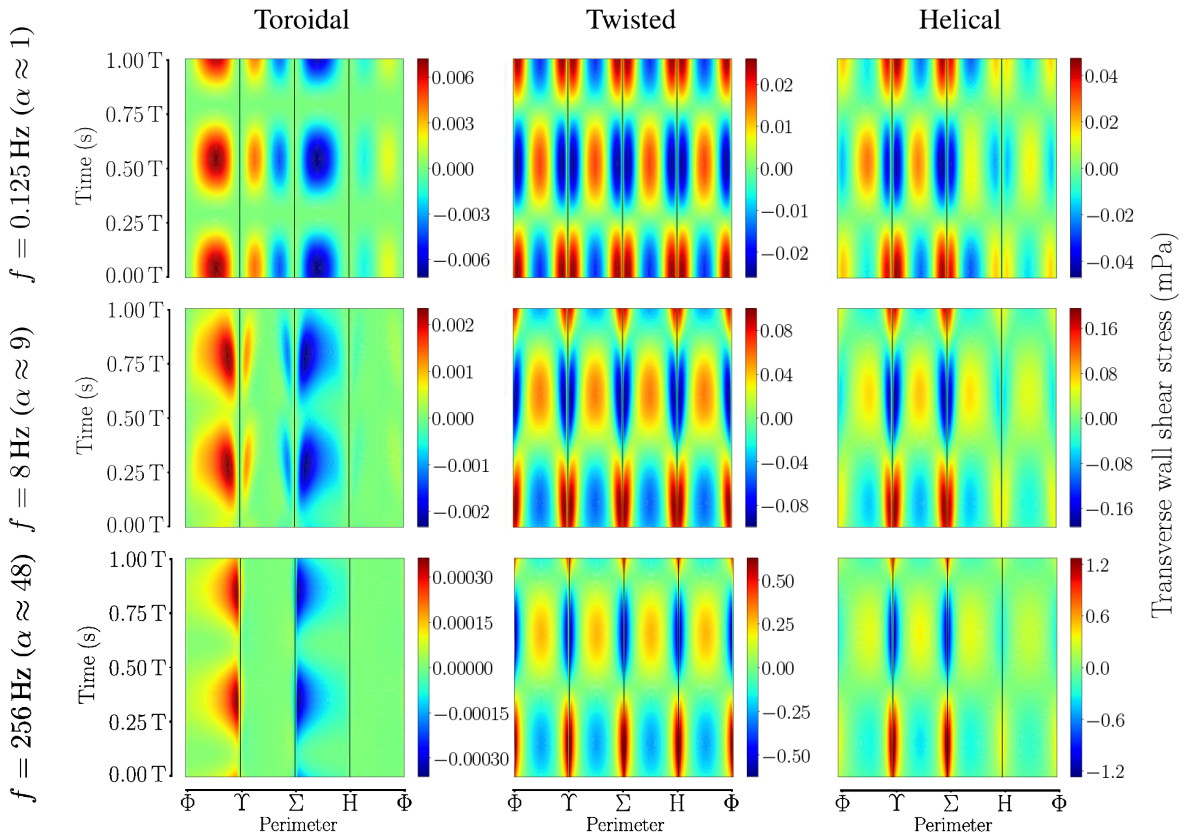

Fig. 3.4. Transverse wall shear stress $\tau_{w,tr}$ visualized for different oscillation frequencies f along the perimeter of the central cross-section. One oscillation period ($T = 1/f$) is shown on the y-axis. Greek capital letters indicate the position along the perimeter. The colorbars are scaled differently.

in the maximum relative TWSS compared to the twisted duct. Conversely, we observed that the maximum TWSS in the toroidal geometry decreases with α^{-2} and falls below 0.01%.

3.5 Discussion

Wall pressure

Wall pressure fluctuations drive transverse flows near walls, as observed, e.g., in the formation of Dean cells in toroidal ducts [136]. The pressure fluctuations we found reflect the behavior of the transverse flows found by [137, 200]. In helical ducts, torsional effects are dominant for transverse flows at low Reynolds numbers [137] and, as our results suggest, also for the corresponding wall pressure fluctuations. Both are similar to those observed in twisted ducts.

We identified two regimes in Fig. 3.2 (and Fig. 3.5): For Womerlsey numbers below 4, the maximum magnitudes behave similarly in the curved, twisted and helical geometries. For $\alpha > 4$ transient inertial forces are predominant and the magnitudes diverge strongly.

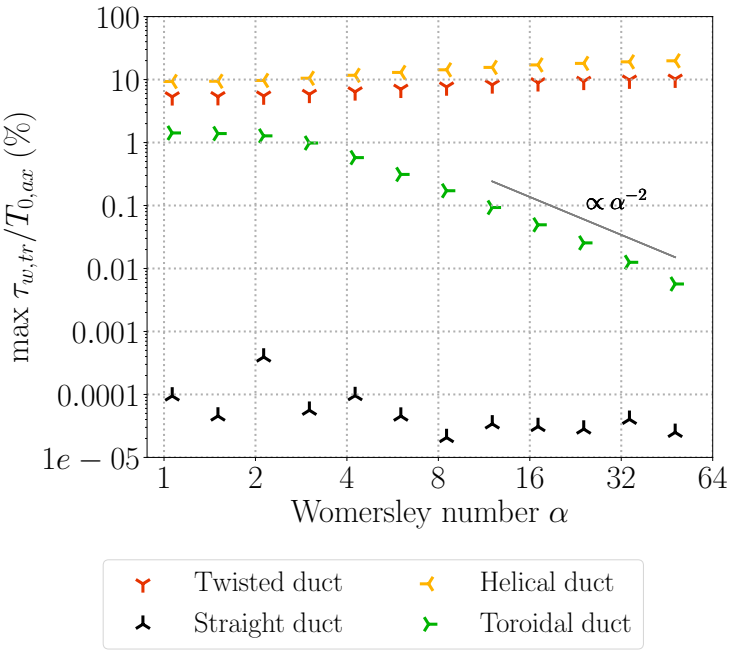

Fig. 3.5. Maximum transverse wall shear stress $\tau_{w,tr}$ with respect to the mean axial wall shear stress amplitude $T_{0,ax}$ (in percent) as a function of the Womersley number. The black symbols indicate numerical noise defined as the maximum relative transverse wall shear stress found in the straight duct simulations.

This coincides with the phase lag between the pressure and the axial velocity which reaches about 90° at $\alpha \approx 4$ [200]. The increase with α^2 in Fig. 3.2a in helical and twisted ducts can probably be attributed to the unsteady term in the Navier-Stokes equations, which scales with α^2 when written in dimensionless form. Conversely, the magnitudes in the toroidal duct remain nearly constant in Fig. 3.2a. This could indicate that the non-linear inertial term continues to dominate in the toroidal duct.

Wall shear stress

The shear stress is highest along the axial direction, but when torsion is present, there is also an evident transverse component. This is an effect of transverse velocities, which in helical ducts at 256 Hz reach a magnitude of above 31% of the main flow [200]. Gammack and Hydon suggested that, for steady flows, torsion leads to an increase in TWSS through altering the transverse flows [152].

Interestingly, the axial shear stress in helical ducts is dominated by curvature, while torsion dominates the transverse component. It seems that AWSS follows axial flow, while TWSS is affected by transverse flow, which show similar dependencies on geometry [200].

The maximum TWSS in helical duct reaches higher magnitudes than we would expect from a superposition of the effects in twisted and toroidal ducts. This is most evident at 256 Hz, where the transverse shear stress in the helical duct reaches a maximum of 20% of the mean AWSS, while the sum of the TWSS in twisted and toroidal ducts would only amount to 10%. Curvature shifts the axial velocity peak towards the inner wall (low

Re, high κ) [198], which enhances transverse velocities there and thus also TWSS caused by torsion. Summarized, the combination of curvature and torsion, as observable in the cochlea, enhance TWSS, while curvature alone leads to negligible TWSS.

Potential physiological implication

The geometry induced transverse flow introduces wall shear stress and local pressure fluctuations which have magnitudes that could be physiologically relevant, especially in the presence of torsion and close to corners. This is particularly interesting because in the cochlea the axial flow and its corresponding transverse flows occur mainly in the scala tympani and vestibuli, introducing possibilities of fluid-structure interactions. Membrane deformations could lead to radial or transverse flow phenomena within the interfacing scala media, which contains the sensory epithelium for hearing.

Study limitations

The main limitation of our study is the use of abstract geometries to represent the highly complex anatomy of the human cochlea [112]. Further studies that include fluid-membrane interactions are needed to investigate the possible effects on the mechanics of the cochlea.

CHAPTER 4

SECOND ORDER AND TRANSVERSE FLOW VISUALIZATION THROUGH 3D PIV IN COMPLEX MILLIMETRIC DUCTS

This chapter is to be submitted as:
Harte N.C., Obrist D., Versluis M., Groot Jebbink E., Caversaccio M.D., Wimmer W. and Lajoinie G.P.R. Second order and transverse flow visualization through 3D PIV in complex millimetric ducts.

A setup for three-dimensional particle image velocimetry and two novel complementary analysis methods are developed and applied to visualize transverse flows in millimetric flow channels. The PIV results are compared to simulations in both the measurement samples and idealized models. Possible physiological implications of Lagrangian streaming in the cross-section are discussed.

Author contribution: Conceptualization and methodology, development of flow set-up supported by David Sprecher, laboratory work and PIV measurements, development of PIV analysis supported by Guillaume Lajoinie, data analysis, CT image segmentation, mesh generation, numerical simulations, manuscript writing and data visualization.

4.1 Abstract

Despite recent advances in 3D particle image velocimetry (PIV), challenges remain in measuring small-scale 3D flows, in particular flows with several orders of magnitude dynamic range. This study presents a scanning 3D-PIV system tailored for oscillatory flows, capable of resolving transverse flows at a small fraction of the axial flow amplitude. The system was applied to visualize transverse flows in millimetric straight, toroidal, and twisted ducts. Two PIV analysis techniques, stroboscopic and semi-Lagrangian PIV, enable the quantification of net motions as well as time-resolved axial and transverse velocities. The experimental results closely align with computational fluid dynamics (CFD) simulations in a digitized representation of the measurement model. Differences between simulations in PIV-specimen and ideal square duct geometries are discussed because of their relevance to (biological) structures with intricate, complex morphologies. While the given PIV system offers a cost-effective and compact setup, challenges at higher frequencies due to decreasing flow amplitudes and increased noise are discussed. Nevertheless, the presented method allows examining periodic flows in micro- to millimeter-scale systems and is particularly suited for applications that cannot be scaled due to their complex multi-physical nature.

4.2 Introduction

Flow related problems are ubiquitous in technical, industrial, and biological applications. In industry, the efficiency of chemical reactors [203], the success of pharmaceutical (e.g., vaccines) production [204, 205], as well as food and beverage processing [127, 206] heavily rely on well-controlled flows. Maritime transport is eminently linked to fluid dynamics [207, 208]. In medicine, flow is central to the development of cardiovascular disease [120, 209–211]. Finally, flow is crucial to understanding the function of organs such as the cochlea [46, 61], which is not yet fully understood [91].

Simulations are not always possible for complex geometries; it can be difficult to model an accurate representation of their shape and generate a high-quality mesh. In addition, setting the correct boundary conditions can be extremely challenging, in particular in a biological context. The flows therein involve fluid-structure interactions, where the viscoelastic properties of the structure are largely unknown. They also involve entry length effects and transient flows. Furthermore, these flow problems are often multi-scale, which results in complex numerical models with heavy computational costs which, ultimately, must also be validated experimentally.

The most widely used flow visualization techniques are probably particle image velocimetry (PIV) and particle tracking velocimetry (PTV). Both involve tracer particles. PIV is based on the cross-correlation of sub matrices in successive images, while PTV consists in tracking the trajectory of individual particles. Other flow visualization techniques include Schlieren photography and shadowgraphy, both exploiting the variations in the refractive index of the fluid of interest, e.g., due to temperature or density variations [212, 213]. Finally, other techniques were developed that use laser-induced fluorescence with fluorescein dye to visualize, for example, secondary flow vortices [160, 161]. In their vast majority, these techniques are designed to image 2D slices of the flow. Although this may be sufficient in some cases, most flow phenomena are intrinsically three-dimensional and thus require 3D visualization.

This fact has led to the development of several PTV and PIV techniques to measure the full velocity field in 3D. They are referred to as three-dimensional three-component (3D3C) measurements. 3D-PTV requires at least two imaging directions (in practice up to 5) to determine the out-of-plane velocity. The technique is effective, but experimentally complex and expensive, and the required processing is computationally heavy. 3D-PTV has been adapted to be feasible with a single camera [176], which, however, requires a calibration, and increases the sparsity requirement. 3D-PIV is not limited by sparsity, which improves the spatial coverage – required for complex flows – and/or reduces the necessary acquisition time. Several variations of this technique have been proposed such as holographic PIV, tomographic PIV, and scanning PIV. The spatial resolution of digital holographic PIV is limited mostly by the image sensor (i.e., CCD) [178, 182]. In tomographic PIV, the whole test volume is illuminated at the same time [183]. Tomographic PIV provides high spatial and temporal resolution, but requires a substantial pulse energy [178]. In scanning PIV fast successive scans of a laser sheet through a volume of interest are recorded with a single synchronized high speed camera [186, 187]. Hori & Sakakibara [214] applied a scanning laser sheet with stereoscopic PIV and a dual camera setup to measure the 3D3C velocity field. Scanning comes at the cost of higher camera frame rates to achieve the desired

temporal resolution. The advantage is a high accuracy, which is mainly limited by the camera features. As cameras continue to improve in resolution, sensitivity, and frame rate, the importance of scanning PIV is also growing.

Two aspects remain challenging with 3D-PIV, which are small dimensions, i.e., 3D-microPIV, and multi-scale flows. The former is a consequence of the optics used for small-scale imaging, as they typically provide a very limited depth of field. Multi-scale flows arise when looking at slow features within a fast flow, especially when these features are orthogonal to the main flow, as is the case for Dean cells, for example. Secondary or transverse flows are of particular interest in the inner ear, where they lead to streaming effects [5, 55] and are suspected to play a role in hearing physiology [61, 102]. Transverse flow is also gaining attention for helical stents in the superficial femoral artery as a possible mechanism to improve stent patency [124, 171]. Several studies have measured transverse flows in toroidal geometries using PIV for their importance to the arterial vessel system [164–168]. The difficulty of measuring transverse flows lies in the fact that they are several orders of magnitudes smaller than the axial flow, especially at low Reynolds numbers. Besides scanning PIV, potential techniques to measure minute transverse flows are digital holographic PIV and tomographic PIV, which are, in particular, used to study turbulent flows [215, 216] and droplets [217, 218]. Scanning PIV offers similar capabilities for the frequencies of interest and is more convenient as it requires a less complicated experimental setup.

We present the development and experimental validation of a scanning 3D-PIV system for small-scale oscillatory flows, which is capable of resolving transverse flows down to about two orders of magnitude smaller than the main axial flow amplitude. This is for axial flows in the orders of millimeters per seconds. With this setup, we experimentally investigate the effect of torsion and curvature on transverse inertial flows in three geometries: a straight square duct, a toroidal duct, and a twisted square duct. The setup is accompanied by two original and complementary forms of PIV analyses: stroboscopic and semi-Lagrangian, which allow for quantifying net flows and time-resolved axial and transverse velocities. The toroidal duct, only exhibiting curvature, causes pairs of rotating flow cells oriented in the transverse plane, known as Dean flow [136, 143]. Inside twisted straight ducts, which only contain torsion, saddle flow patterns arise depending on the cross-section of the duct [132, 137, 138]. The duct shape was measured using micro-CT (μ-CT), and used to perform geometry-specific CFD simulations. The experimental measurements are in good agreement with these simulations. We detected time-resolved transverse flows down to 5% of the axial flow amplitude in the twisted duct and down to 2% of the axial flow amplitude in the toroidal duct at 5 Hz. The detected net flows are approximately 1% of the axial flow for the toroidal duct and 0.1% for the twisted duct at 5 Hz.

This technique allows for investigating periodic flows in models of micrometric to millimetric systems that cannot be scaled up because of their multi-physics properties. This includes flows induced by membranes motion as, e.g., in the inner ear [15, 45, 219], flows with solid particles or cells, and cilia-driven flows, e.g., in the models of trachea [220, 221] or amphibian skin [222, 223]. Other possible applications include in vitro models of millimeter-sized blood vessels, which are in many cases highly curved and twisted. Some examples are the umbilical vein and the helical umbilical arteries [224, 225], the superficial femoral artery [171], and the circle of Willis [226].

4.3 Material and methods

Measurement set-up

Models

We measured transverse flows within straight, toroidal, and twisted flow channels (see Fig. 4.1). We chose these models as our previous work is based on fluid simulations in ideal square ducts, and can serve as a validation framework [200, 227]. The toroidal flow channel has a radius of curvature of approximately 2.8 mm, which equals a curvature of $\kappa = 0.36\,\mathrm{mm}^{-1}$. The torsion of the twisted flow channel is approximately $\tau = 1/6\,\mathrm{mm}^{-1}$ in the measurement sample. These values are within the range proposed by Viergever [94] and match values observed in human anatomy [48, 133]. The flow channels were created by heating acrylonitrile-butadiene-styrene (ABS) square rods with a size of approximately 2 mm with a heat gun and thermally bending them into the desired shape. The bent ABS rods were then cast in polydimethylsiloxane (PDMS). After curing, the ABS rods were dissolved with acetone and only the PDMS casting remained. A heat bath at 55 degrees Celsius was used to accelerate the dissolution process. The flow channels were extended at each end with a straight segment of at least 20 mm length to minimize possible entry length effects from the inlet and outlet.

Fluid solution

The density and viscosity of the perilymphe in the cochlea are similar to those of water at body temperature [50]. We used an aqueous solution with 49 wt% urea to obtain a refractive index of about 1.41 (measured by [229] at 589 nm), which matches the PDMS specimen. Refractive index matching is needed to avoid optical distortion. The solution's density $\rho = 1133\,\mathrm{kg/m}^3$ and dynamic viscosity $\mu = 1.7\,\mathrm{mPa\,s}$ are higher than those of water [229, 230]. We added homogenous fluorescent tracer particles (Fluoro-Max dry red fluorescent polymer microspheres from Thermo Scientific™) with a diameter of 6 μm and a density of $1050\,\mathrm{kg/m}^3$ to the solution.

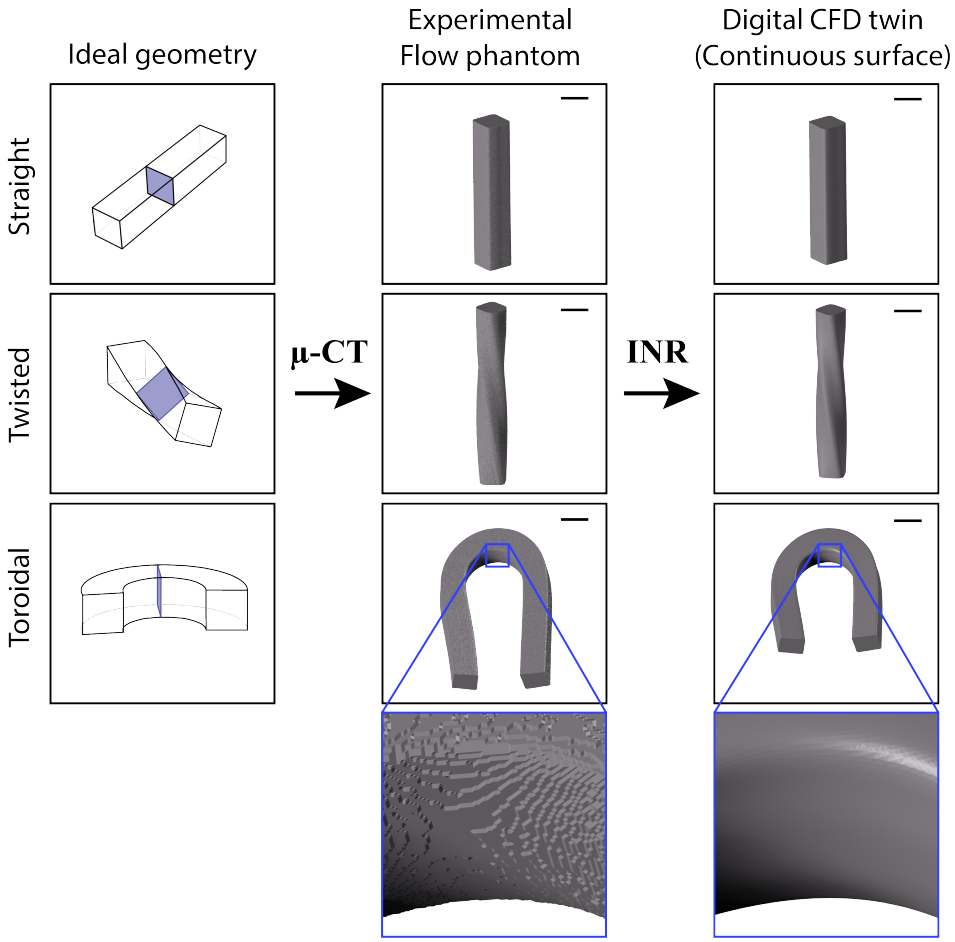

Fig. 4.1. Flow channels of the straight, toroidal and twisted samples. From left to right: ideal CFD models with a $2 \times 2\,\mathrm{mm}^2$ cross-section, μ-CT scan of the measurement samples, and CFD models obtained with continuous implicit neural representations (INR) of the scanned samples [228]. The scale bar measures 2 mm.

Flow system

Figure 4.2A shows the setup schematics. A custom-built actuator pump induced an oscillatory motion in the fluid during measurements. Its key component is a piezoelectric transducer (PHUA6630; PiezoListen™ series), driven by a Raspberry Pi 4B mini-computer and a Hifiberry AMP2 amplifier. The piezoelectric transducer was attached to a thin 3D-printed polyethylen terephthalat (PET) shell, which was mounted on a small, sealed fluid container. A continuous flow through the phantom was maintained between measurements to prevent sedimentation of the particles on the walls of the specimen and keep the particle suspension homogeneous. During measurement, the steady flow was fully stopped by a manual valve positioned between the oscillatory pump and the gear pump. The flow rate and fluid temperature were monitored with a commercial thermal flow sensor (Sensirion® SLF3S-0600F) placed between the oscillatory pump and the specimen. The inner tube diameter in the flow circuit was 2 mm. To minimize the system's inertia and achieve higher flow rates, the fluid volume in the flow system was minimized to approximately 100 ml.

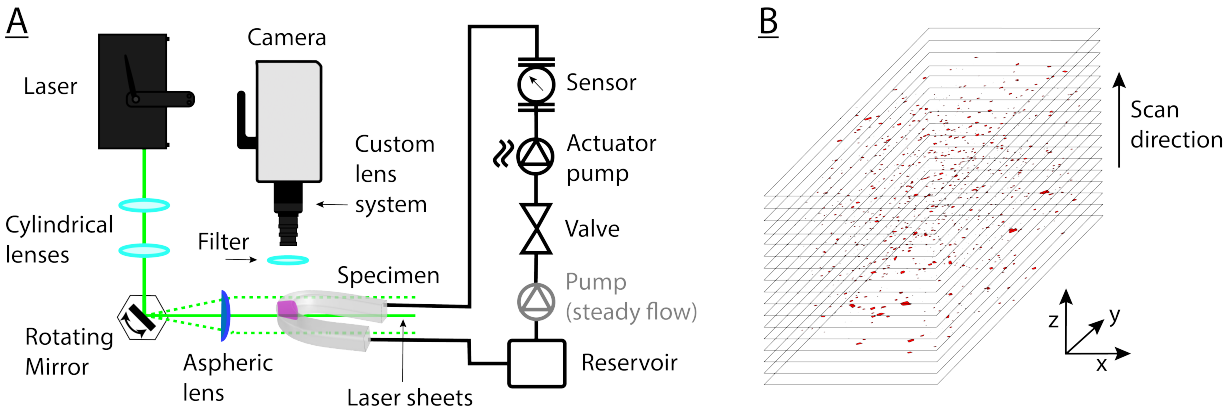

Fig. 4.2. (A) Schematics of the 3D-PIV measurement setup. Gray labels denote parts not running during measurement. (B) Stacked images of raw data (colors inverted). The image height along the scan direction corresponds to different layers of the same scan.

Nonetheless, owing to the limited bandwidth of the flow system, velocities were lower for 20 Hz than for 5 and 10 Hz (Table 4.1).

Optical system

The optical setup, shown in Fig 4.2, uses a continuous wave frequency-doubled Nd:YAG(-532 nm) laser to stimulate the fluorescent particles, which have an absorption maximum at 542 nm. The laser beam was expanded into a sheet by three lenses. First, a cylindrical plano-concave lens diverges the laser beam in the x-direction, while a cylindrical plano-convex lens focuses it onto the rotating mirror. The mirror is in the focal distance of a plano-convex aspheric lens, which collimates the beam in the desired sheet and focuses it in the elevation direction to minimize the sheet thickness within the camera's depth of field. The long focal distance of the lens ($f = 121$ mm) minimizes the variations in the thickness of the sheet within the area of interest. This configuration also ensures that the laser sheet translates through the sample without rotation (Fig. 4.2B). To characterize the laser sheet, a glass plate coated with a thin layer of PDMS containing fluorescent Nile Red was fixed at a 45° angle to the laser and camera. The beam width was defined as the $1/e$ width of the profile after correction for the PDMS layer thickness. The laser sheet thickness was estimated as $\delta_l = 13.5 \pm 0.9\,\mu$m. The details of the laser sheet calibration and the variation in sheet thickness through the sample are provided in appendix 4.8. The rotating mirror was driven by a sawtooth waveform which provides a linear position of the sheet as a function of time. The scanning frequency and amplitude can be tuned independently through the driving frequency and voltage (see appendix 4.8 for more details).

A high-speed CMOS camera (NOVA S16, Photron, Tokyo, Japan), captured the light emitted by the fluorescent particles in synchronization with the laser scanning. The measured test section had a volume about $1 \times 2 \times 2\,\text{mm}^3$. We combined two commercial camera lenses front-to-front to obtain a suitable combination of magnification and depth of field. A tele-macro lens with a focal length $f = 105$ mm, was attached to the camera in the normal direction and focused to infinity. The aperture was closed as much as possible. A macro lens with $f = 12.5$-75 mm, was attached to the first lens in reversed direction and was

also focused to infinity. The aperture and focal length of the second lens were adjusted to obtain the desired field of view. The diaphragms of the lenses enabled a depth field of more than 100% with respect to the field of view, at a frame rate of 40 kpfs. A dichroic filter was placed between the lenses to remove the small fraction of laser light scattered by the sample. We calibrated the PIV system using a resolution target (1951 USAF). The spatial imaging resolution was approximately $5 \times 5 \times 15\,\mu\text{m}^3$ for a typical focal length of $f = 22\,\text{mm}$ (see appendix 4.8).

Experimental procedure

Table 4.1. Measurement parameters. The actuation frequency f refers to the fluid oscillation frequency, while W_0 denotes the velocity amplitude. The number of layers is given by the ratio of the camera frame rate and the laser scan rate.

f (Hz)	Scan rate (Hz)	Frame rate (fps)	# layers	W_0 (mm/s)
5	100	20000	200	$4-8$
10	200	40000	200	$4-7$
20	400	40000	100	$3-6$

The specimen was aligned with the laser such that the sheet was focused on its center, which was achieved by first aligning the sample manually and then adjusting the offset voltage of the sawtooth signal driving the mechanical mirror. The measurement was only started when the flow sensor reported steady oscillations. A pulse generator triggered the driver of the rotating mirror and the camera for data acquisition. The high-speed camera memory allowed for recording 45 periods, with 20 scans per period and a resolution of 256×496 pixels. For each scan, we recorded a volume consisting of 200 layers for frequencies below 20 Hz. To compensate for the increased frame rate necessary at higher frequencies, we reduced the layers to 100 at 20 Hz, see Table 4.1. This increased the number of recorded periods to 90. Using a resolution of 128×496 pixels doubles the number of recorded frames.

We performed measurements in three samples (Fig. 4.1) for three actuation frequencies (5, 10, and 20 Hz). The flow amplitude was adjusted by changing the gain of the signal driving the piezoelectric actuator. For each frequency, we measured different flow amplitudes in the operating ranges of the actuator pump. The fluid phenomena are laminar and the associated Reynolds numbers (between 1 to 10) are close to the Stokes regime. The resulting Womersley numbers (4.5 to 9) are above the quasi-stationary regime ($\alpha > 1$).

Particle image velocimetry analysis

We have developed two complementary analysis methods to analyze transverse velocities, which exploit the same measurement data: the stroboscopic and the semi-Lagrangian PIV (Fig. 4.3). The stroboscopic approach shows the transverse net motion with high accuracy, while the semi-Lagrangian approach is used to visualize the instantaneous, time-resolved transverse flows. In principle, an (Eulerian) net motion can be obtained from the time-resolved approach by averaging instantaneous velocities over time (Eulerian streaming).

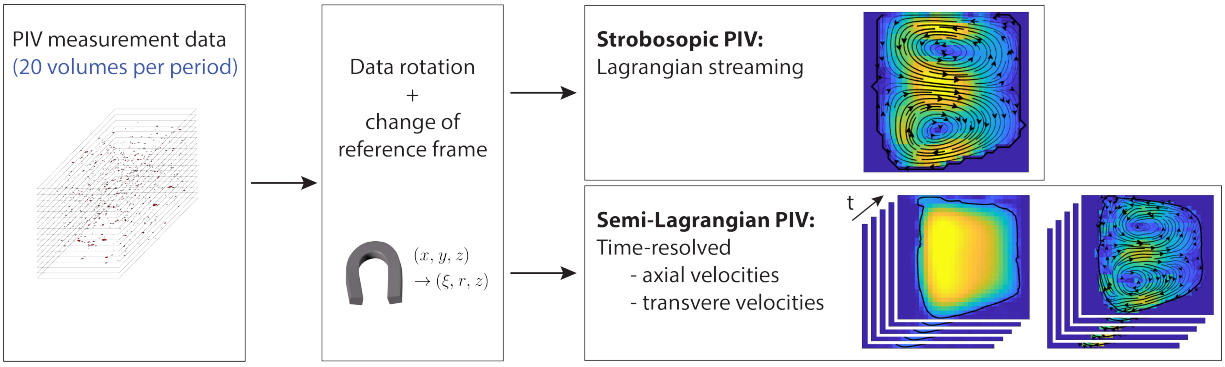

Fig. 4.3. The measurement data was analyzed using the stroboscopic and the semi-Lagrangian PIV method. In both procedures, the data was rotated to align the axial flow direction with the x-axis. In the toroidal duct, the reference frame was changed to polar coordinates to define transverse planes of constant angles and average velocities along the curved channel. The stroboscopic approach was used to visualize net motions, i.e., Lagrangian streaming, while the semi-Lagrangian PIV gave time-resolved axial and transverse velocities.

This approach, however, provides a much lower signal-to-noise ratio (SNR) than the stroboscopic approach for net motion and is thus not retained. The net motion from the stroboscopic approach provides a Lagrangian mean velocity, representing the average velocity of a particle during one oscillation cycle.

The analysis is based on two assumptions. First, we consider the scanning rates to be high enough to neglect the motion occurring between the frames forming a single volume. Second, to increase the SNR, the velocities can be averaged along the channel axis since we measure a short test section (0.5 - 1 mm along the axial direction).

Alignment, data rotation, and PIV settings

Moving consecutively from top to bottom, the scanning laser sheet illuminates a narrow section of the flow channel. The scanning direction defines the z-axis. Consequently, the planes captured by the camera are parallel to the xy-plane, i.e., the measurement plane. The x-axis is aligned with the channel axis. Since we aim at measuring minute flow orthogonal to the channel axis, it is necessary to ensure that this channel axis is perfectly aligned with the x-axis as defined for the analysis. Such precision cannot be achieved experimentally and has to be adjusted in a processing step. To that end, the direction of the main axial flow is determined from a first PIV analysis. The deviation angles are then determined from the median of the directions of the velocity vectors. Finally, the volumes (4D stack of images) are rotated by these angles. For simplicity, we write the velocities in the x, y, and z directions as U, V and W.

The image intensity of each layer is normalized with respect to 99% of its maximal intensity (averaged over 15 images) to compensate for the brightness reduction in layers that are physically further from the camera. The PIV analysis is based on PIVlab [231, 232], a particle image velocimetry tool for MATLAB®. More specifically, we use the built-in multi-pass technique with decreasing interrogation window sizes: 64×64, 32×32, 22×22 px^2 and a 50% overlap of the interrogation areas. While we apply these three passes in the

measurement plane (xy-plane), only two passes (with final pass size of $32 \times 32\,\mathrm{px}^2$) are used in planes, which are constructed or interpolated from the measurement planes (e.g., in the xz- and yz-plane). The spatial resolution of the resulting 3D velocity field is approximately $80\,\mu$m. The velocities are collected in 20 bins per cycle and the median velocity over all cycles that could be recorded by the camera is used to increase the SNR.

Reference frame for the toroidal duct

In the toroidal duct, the streamwise and radial velocity components are not exactly aligned with the x-axis and y-axis, because of the curvature of the channel's main axis. To account for the deviation, we computed the geometrical center of curvature and used it to define a local polar coordinate system. The U and V velocities are decomposed in the local coordinate system to obtain an angular velocity U_ξ and a radial velocity U_r, while the third velocity component is left unchanged and $U_z = W$.

More specifically, we first compute the center of curvature by performing a PIV analysis to determine the in-plane velocity field for each layer. The velocities are averaged in the z-direction over these layers for a better estimation of the flow field. We then extract the locations of the strongest flow for each x-coordinate, by taking a velocity-weighted average of the y-coordinates, in the y-direction (see Fig. 4.4A). We estimate mean velocities at these locations by averaging over 11 pixels in the y-direction. The normalized, in-plane reference velocity vector is defined as the median velocity over these locations (see red arrows in 4.4A). Finally, the (in-plane) center of curvature R_c is determined as the point with the smallest mean distance to all normals on the mean velocity vectors. To improve R_c, the angle between the reference velocity and the y-axis is varied. The optimal angle is chosen as the angle at which the transverse velocities summed over the yz-plane are minimal. To decompose the in-plane velocities, we defined at every grid point a radial unit vector $\widehat{\mathbf{e}}_r$ pointing towards the center of curvature R_c and an angular unit vector $\widehat{\mathbf{e}}_\xi$. Subsequently, the velocity vectors are projected onto these angular and radial unit vectors. The radial velocity here corresponds to the transverse velocity in the xy-plane, while the angular velocity represents the axial velocity. Finally, the velocities are interpolated to a uniform grid of r and $\xi = R_0\theta$, see Fig. 4.4B. This transformation is then applied to each layer such that $(U, V, W) \rightarrow (U_\xi, U_r, U_z)$ and $(x, y, z) \rightarrow (\xi, r, z)$. The out-of-plane velocity W is obtained as explained in the semi-Lagrangian PIV: $U_z = W$.

Stroboscopic PIV

The stroboscopic PIV method provides a fast way to analyze the data and get an impression of the net flow field, despite having axial velocities orders of magnitude larger than the investigated net motion. In this procedure, we perform the PIV analysis between volumes from the same phase in the oscillation period, i.e., volume N is compared to volume $N+20$, for each oscillation frequency. The initial volume for the series is chosen at the peak axial velocity, corresponding to a 0-displacement of the particles. Note that this choice is, in fact, arbitrary. The peak velocity is determined from a PIV analysis on the central measurement plane. The space between the layers in z-direction, in the recorded volume, is cubically interpolated to get the same spatial resolution as in the x and y-directions. The transverse

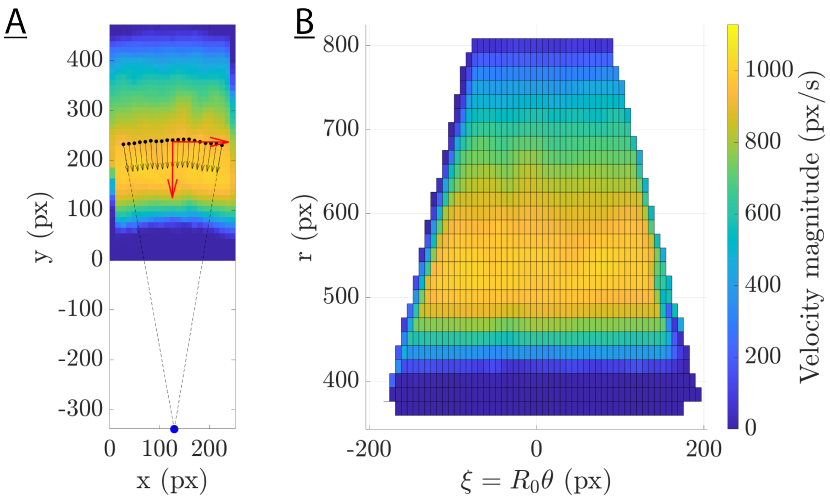

Fig. 4.4. Velocity transformation from 2D Cartesian (x, y) to polar coordinates (ξ, r). (A) The center of curvature (blue dot) and velocity magnitude in Cartesian coordinates. Radial vectors are shown in black at the velocity-weighted y-positions (black dots). The red arrows indicate the radial and axial reference velocities. (B) Velocity magnitude in polar coordinates, interpolated to a rectangular grid.

planes are constructed from the volumes by averaging over 21 pixels in the x-direction with 50% overlap between the planes. The PIV analysis is then performed in these planes to determine the transverse net velocities V_{net} and W_{net}. To increase the SNR, we average V_{net} and W_{net} over all periods and over all transverse planes. The resulting velocity field is the average net velocity in the transverse plane during one oscillation cycle.

Semi-Lagrangian PIV

The basic concept of the semi-Lagrangian PIV approach consists in using the particle displacement in the axial direction to construct the "semi-Lagrangian" transverse planes. These planes deform in the axial direction to follow the axial motion of the particles. The images constructed from pixels on these deformable planes thus do not suffer from disappearing particles due to the main flow and can be subjected to PIV analysis.

The first steps are identical to the section "Reference frame for the toroidal duct", where the U and V velocities (U_ξ and U_r in case of the toroidal duct) are obtained from analyzing each slice of the 3D volume individually. For all geometries, U is averaged along the x-direction and integrated to obtain the axial displacement. Figure 4.5 shows an example of the displacement in the central layer of the volume. We apply a spline interpolation to the displacement profile in the y-direction to obtain a profile with the same resolution as the original image. The semi-Lagrangian transverse planes are constructed by stacking the pixels on this moving line (blue line in Fig. 4.5) through the layers of the volume. Since individual pixels would provide a too sparse image, the pixels of the semi-Lagrangian planes are the average over 11 pixels in the x-direction with 50% overlap between the planes. The transverse velocities V and W are subsequently obtained by running a PIV analysis on the constructed planes. We average the velocities from the same time points per cycle over all cycles. The V, W velocities are further averaged over all semi-Lagrangian planes. In

case of the toroidal duct, we use the radial velocity U_r instead of V and transformed the velocities to polar coordinates, see section "Reference frame for the toroidal duct".

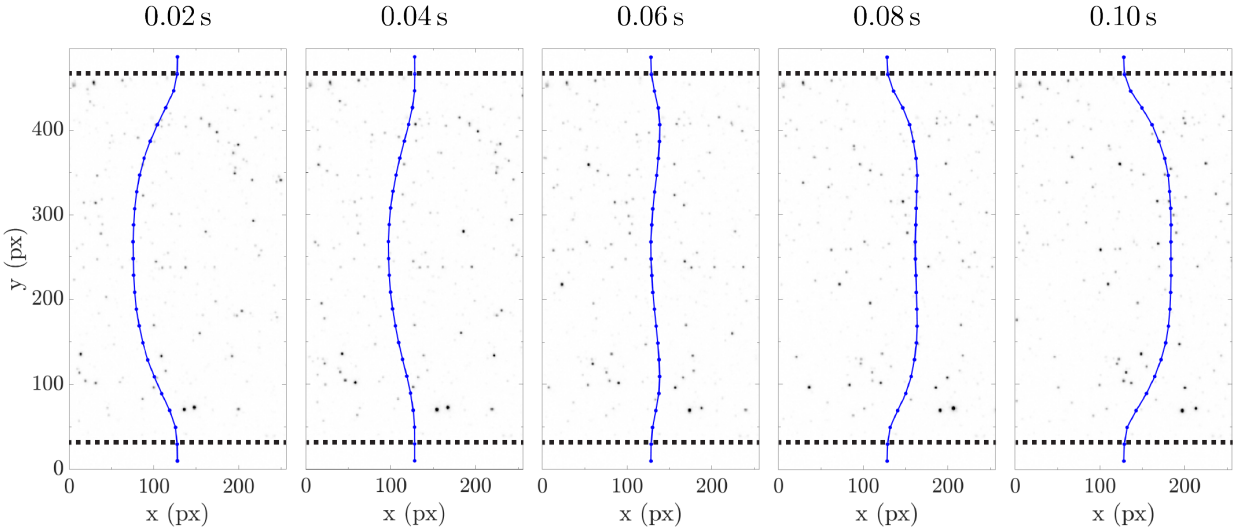

Fig. 4.5. Particle motion and reconstructed average displacement (blue line) in the central measurement plane for an oscillation frequency of 5 Hz (colors inverted). The dotted line indicates the approximate duct boundaries.

Computational fluid dynamics simulations

Idealized models

We simulated fluid flow in ideal geometries (Fig. 4.1) as ground truth for the measurements that can be compared to literature. The geometries were constructed using established methods [114, 137] with centerline curvature $\kappa = 1/3\,\mathrm{mm}^{-1}$ and torsion $\tau = 1/8\,\mathrm{mm}^{-1}$. To save computational resources, we chose a total arc length of the centerline of 10 mm for all models. The model cross-section is 2 mm × 2 mm.

Measurement models

To perform computational fluid dynamics (CFD) simulations in the same geometric shapes as were used in the measurements, the samples were measured using a high-resolution μ-CT scanner (μCT, SCANCO Medical AG, Switzerland, isotropic voxel size of 20 μm). The flow channels were segmented from the μ-CT scans and converted into a continuous representation using an implicit neural representation [228] from which the CFD surface at any arbitrary precision can be derived. The scan and its representations are shown in Fig. 4.1 for the three models.

Numerical simulations

The flow was modeled as the incompressible flow of a Newtonian fluid [50]. We used a sine pressure boundary condition at the inlet and zero pressure at the outlet surface. No-slip boundary conditions were imposed on the walls. The fluid properties from section "Fluid

solution" were used. The simulation parameters were set to match the measurements: we used oscillation frequencies of 5, 10, and 20 Hz and extracted the mean axial velocity amplitudes from the PIV results to set the pressure boundary criteria for CFD, i.e., we chose the inlet pressure amplitude such that the axial velocity amplitude averaged over the inlet surface was the same as in the measurements.

Simulations and meshing for the geometry-specific models were performed using the finite element solver COMSOL Multiphysics® (COMSOL AB, Stockholm, Sweden). For the ideal models, structured meshes were generated as described in Harte et al. [200] and Harte et al. [227] and consisted of 77 500 hexahedral elements per geometry. The number of elements was chosen based on a convergence analysis. Lagrange elements of order two and one were used for velocity and pressure (P2P1), respectively. For the time-dependent solver, the implicit backward differentiation method of variable order (between 1 and 5) was used. We chose 100 steps per oscillation period of the pressure boundary condition. To ensure that the initial transient was washed out, the inlet pressure amplitude P_0 was ramped up smoothly over the first few cycles, e.g., 16 cycles at 5 Hz.

The motion of tracer particles was determined using the COMSOL Multiphysics® "Particle Tracing for Fluid Flow" interface. We used the massless formulation because we assumed that the tracer particles were small enough to move with the local fluid velocity (Stokes number of approximately 10^{-4}). To compute the Lagrangian mean velocity, the particles were released and traced for one cycle. The difference in the end positions divided by the time interval $T = 1/f$ is the Lagrangian mean velocity.

Transverse and axial flow

In the idealized models, we applied the orthonormal Frenet-Serret frame consisting of the tangent ($\widehat{\mathbf{t}}$), normal ($\widehat{\mathbf{n}}$), and binormal ($\widehat{\mathbf{b}}$) unit vectors to decompose the velocity field $\mathbf{u}$:

$$\mathbf{u} = u\widehat{\mathbf{n}} + v\widehat{\mathbf{b}} + w\widehat{\mathbf{t}}, \tag{4.1}$$

and defined the velocity component along the tangent as axial flow $w = \mathbf{u} \cdot \widehat{\mathbf{t}}$, while the components in the normal and binormal directions, $u = \mathbf{u} \cdot \widehat{\mathbf{n}}$ and $v = \mathbf{u} \cdot \widehat{\mathbf{b}}$ constitute the transverse flow.

In the geometry-specific models, the centerlines were extracted using kinematic surface fitting [113] and cross-checked with the vascular modeling toolkit [233]. The transverse plane was defined as orthogonal to the centerline.

4.4 Results

2D flow field

Figure 4.6) shows an example of the in-plane velocity in the center of the geometry, which was obtained by analyzing images of the same layer from consecutive volume scans. The profiles in the bottom row show the axial velocity component W along the red line at different times, which are typical Womersley profiles for low Womersley numbers ($\alpha \approx 4.5$)

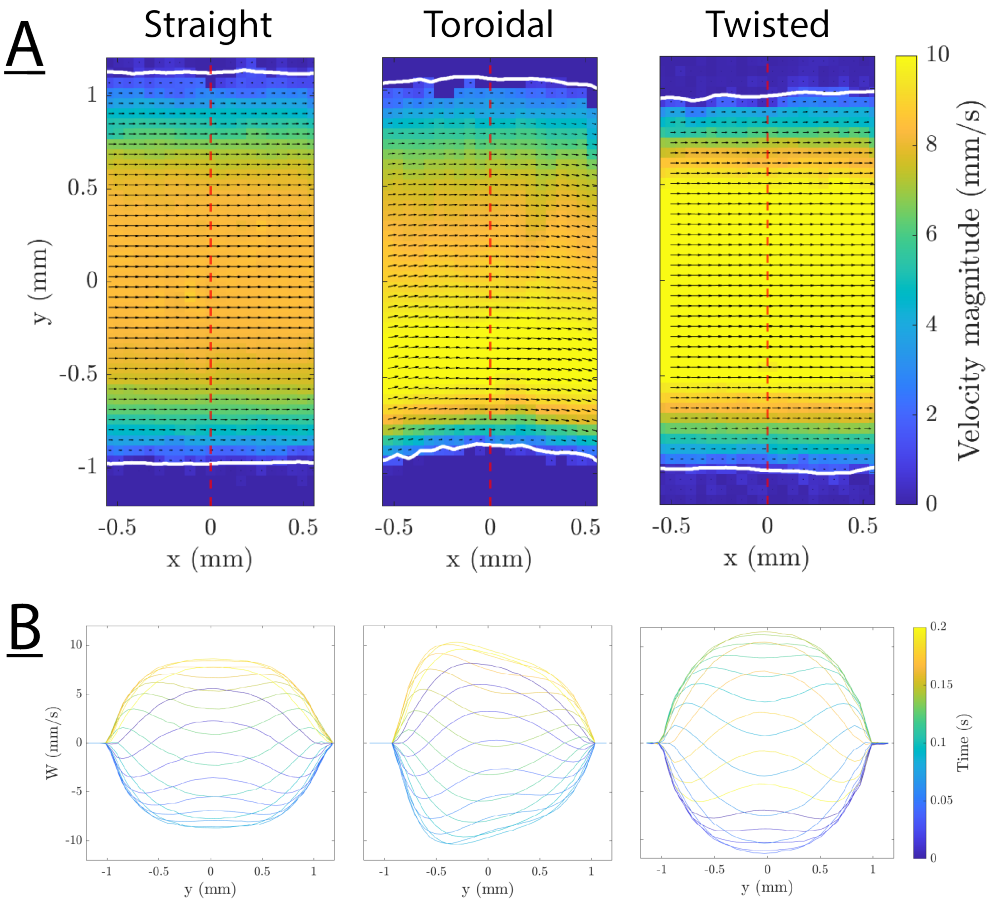

Fig. 4.6. In-plane velocities in a central measurement plane for an oscillation frequency of 5 Hz. (A) 2D flow at peak velocity. (B) Axial velocity profile at different times of one oscillation cycle. The red line (top row) indicates the position where the velocity profiles were evaluated.

in all three geometries: In the core the profile is flatter than we would expect for quasi-stationary Poiseuille flow and the velocity gradients in the vicinity of the walls are steeper. The axial velocity is well resolved in time and space and shows the expected behavior. In the toroidal geometry, the velocity profile is skewed towards the inner side of the curve, as will be discussed in the next section. In contrast, the profile of the twisted duct exhibits a similar velocity profile as the straight duct. This is in agreement with Kheshgi [132] and Zabielski & Mestel [135] who observed that torsion has only a small impact on axial flow.

Axial flow

Figure 4.7 shows the axial velocity amplitude in the transverse plane for an actuation frequency of 5 Hz ($\alpha = 4.5$) according to both the PIV measurements and geometry-specific CFD simulations. There is a small deviation in the flow amplitude between the measurements and the simulations, most likely, due to differences in the geometry owing to either a slightly different location along the axis or the finite precision of the μ-CT scan. The peak velocity is approximately 5% higher in the CFD model of the twisted duct than in the PIV measurement for this sample. Nonetheless, the axial velocity profiles obtained from

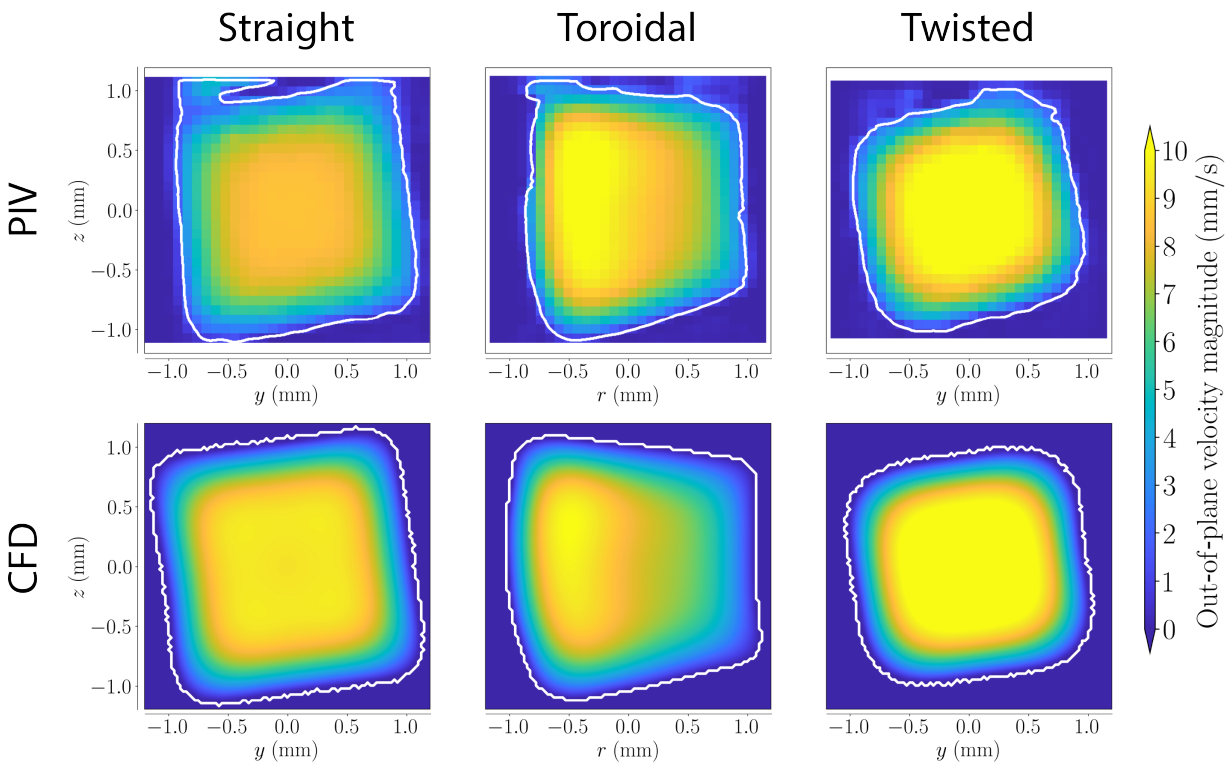

Fig. 4.7. Axial velocity amplitude for an oscillation frequency of 5 Hz. The inner wall of the curve is to the left in the toroidal duct.

the geometry-specific simulations are in good agreement with the PIV measurements. In the toroidal geometry, the maximum velocity shifts towards the inner wall of the bend, contrary to expectations from higher Reynolds numbers. The shift towards the inner wall occurs because of the low Reynolds number and the high curvature [128, 198]. Along the inner wall, the axial pressure gradient is steeper compared to the outer wall because the arc length is smaller. Since the centrifugal forces pushing the fluid outwards are weak at low Dean numbers, we suspect that the effect of the higher-pressure gradient probably dominates, so that the highest velocities are found closer to the inner wall. The Dean number, used to describe flow in toroidal ducts, is proportional to the Reynolds number $De = Re\sqrt{d_h/(2R)}$, where d_h is the hydraulic diameter of the pipe and R is the radius of curvature.

Net transverse flow

The tracer particles exhibited a net motion (Lagrangian mean velocity) in the transverse plane, which was visualized using the stroboscopic PIV approach. Figures 4.8 and 4.9 show the transverse net motion in the toroidal and twisted duct for frequencies of 5, 10 and 20 Hz. In curved ducts, the tracer particles follow the streamlines of Dean cells (Fig. 4.8). The Dean flow points towards the outer wall in the ducts center and towards the center of curvature close to the top and bottom boundary of the cross-section. At higher oscillation frequencies, the vortex centers move closer to the cross-section's top and bottom boundary and the inner wall. The shape of the Dean cells is consistent between the CFD and the PIV

results. In particular, they both show the same asymmetry in the Dean cells caused by the specific, nearly trapezoidal, cross-section of the duct. Unlike in the idealized models, the axis between the two Dean cells is tilted in the models with the trapezoidal cross-section. The tilt is more pronounced at 10 Hz than at 5 Hz for the measurements, as well as the geometry-specific CFD. Furthermore, the Dean cells are not of equal size.

At 5 Hz, the transverse structures show flow magnitudes on the order of 100 μm/s, i.e., 1.6% of the axial flow. The net flow is captured accurately and quantitatively. The same holds for 10 Hz, where the transverse flow falls to 0.6% of the axial flow, i.e., approximately 40 μm/s. However, at 20 Hz, the Dean cells have a velocity on the order of 0.3% of the axial flow, i.e, about 10 μm/s, based on the CFD analysis. There, the transverse flow patterns from PIV fall within the noise floor of the proposed method. All referenced flow ratios, including subsequent ones, are given relative to the axial flow amplitude averaged over the cross-section.

In the twisted duct, the net motion was more than an order of magnitude smaller than in the toroidal duct (the color scales are by a factor of 15 lower). The transverse flows caused by torsion change direction with the axial flow, and are thus largely averaged out when performing such time-averaged measurements (see Fig. 4.9). In addition, in the twisted duct, the net transverse flow consists of complex, small-scale structures. Therefore, since the exact transverse planes visualized in the measurements is not known, it is difficult to perform a detailed quantitative comparison. Nonetheless, the defining structures are very similar for the measurement and for the CFD at 5 Hz, with a pair of counter-rotating vortices in each corner and a flow through the center. The magnitude of the transverse flow is also in quantitative agreement between the CFD and the measurements, and amounts to roughly 0.1% of the axial flow (6 μm/s). Because of these low net flows, the PIV analysis only reveals the strongest transverse features at 10 Hz, and at 20 Hz the transverse flow is altogether lost. The net motion in the real cross-section deviates strongly from that in idealized ducts. For example, at 5 Hz, the strongest velocities are on the diagonal in the idealized ducts, while in the measurement they are close to the center of the side walls (Fig. 4.9). This highlights the need for geometry-specific strategies in complex, real-world systems.

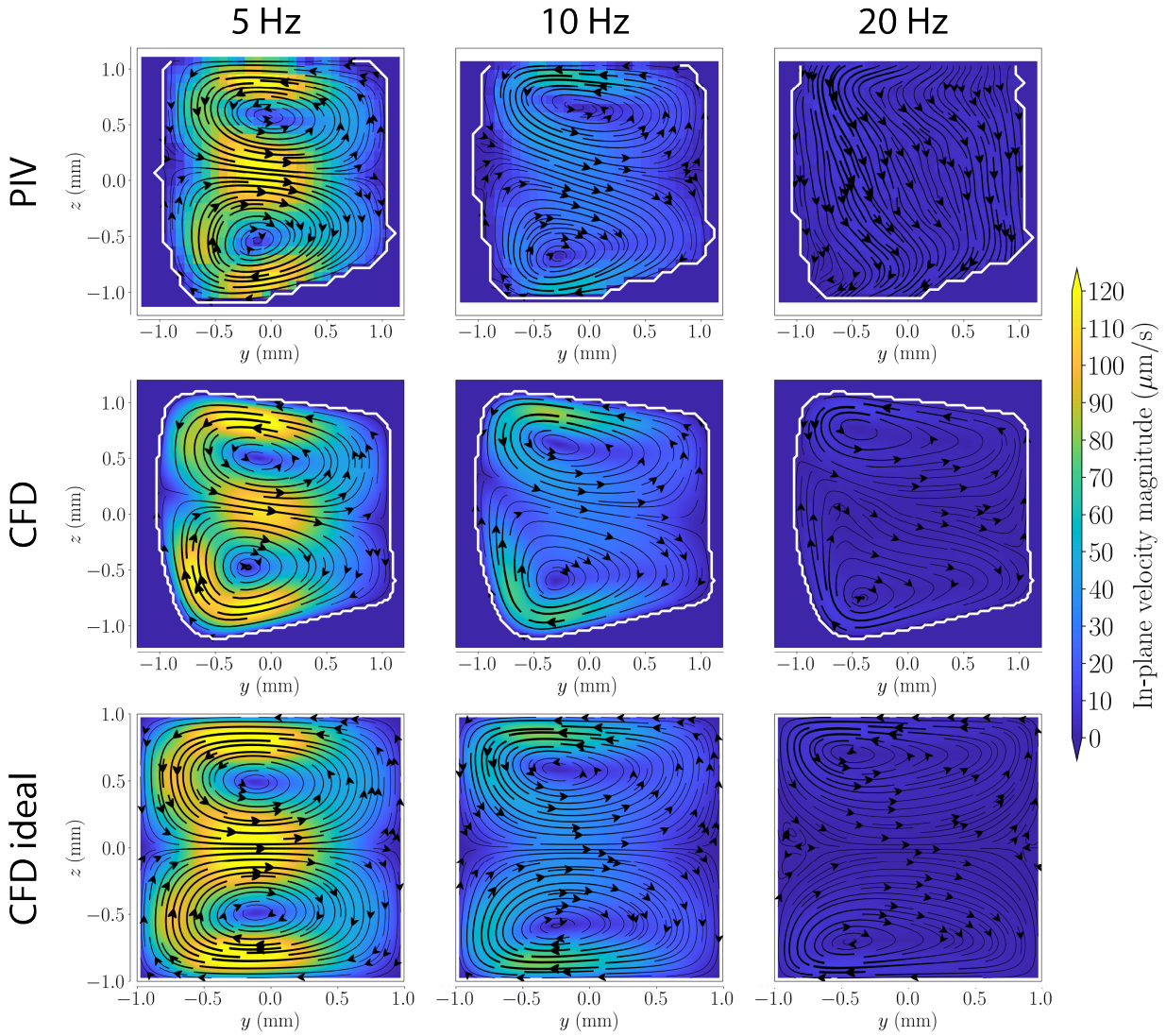

Fig. 4.8. Transverse net motion (i.e., Lagrangian streaming) for an oscillation frequency of 5, 10 and 20 Hz in the toroidal duct. The inner wall of the curve is to the left. The white lines indicate the approximate wall locations.

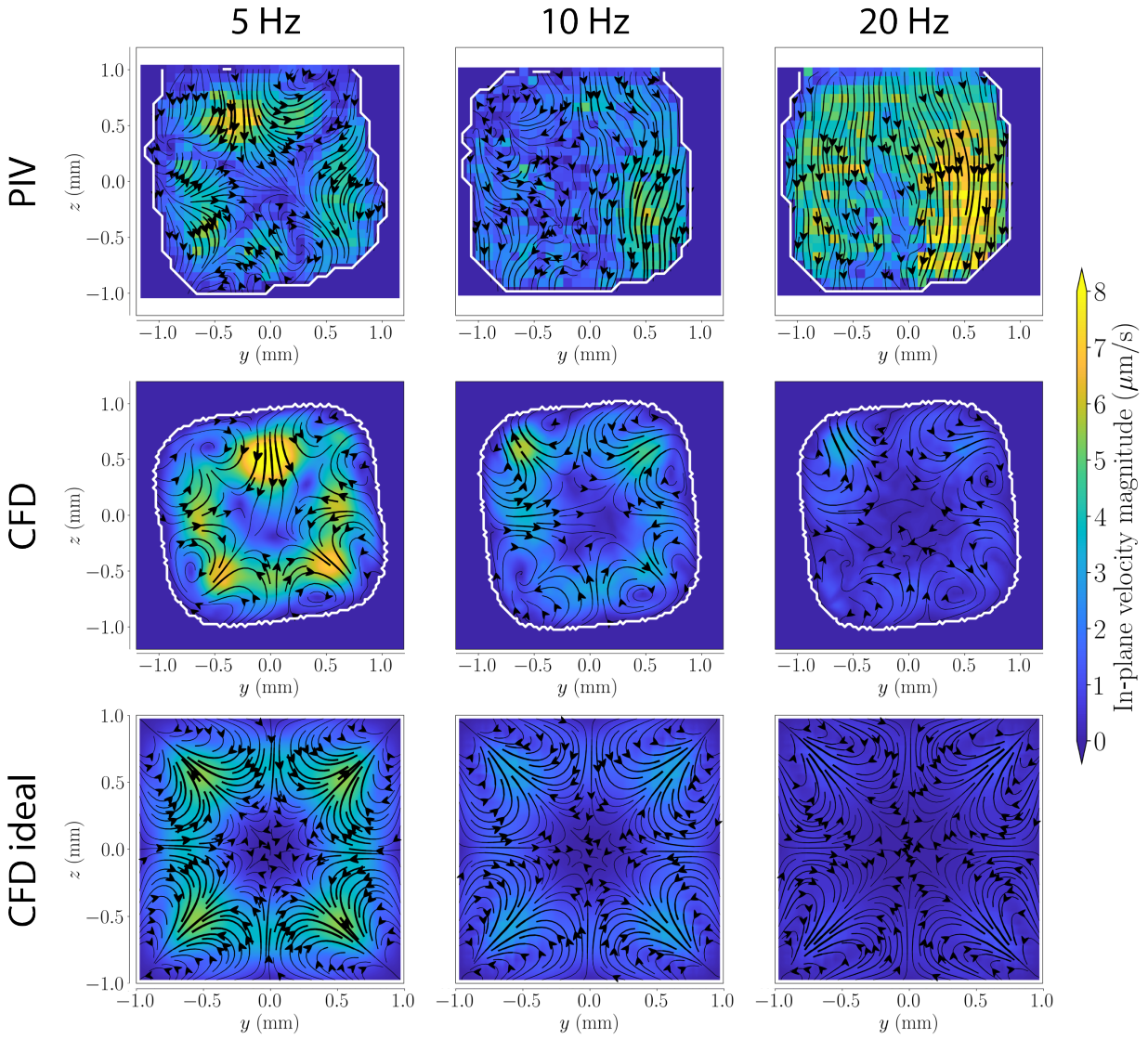

Fig. 4.9. Transverse net motion (i.e., Lagrangian streaming) for an oscillation frequency of 5, 10 and 20 Hz in the twisted duct. The white lines indicate the approximate wall locations. The absence of closed streamlines in the idealized twisted duct can be attributed to the absence of particle trajectories data at its boundaries. Looking into the page plane, the twisted duct turns clockwise.

Dynamic transverse flow

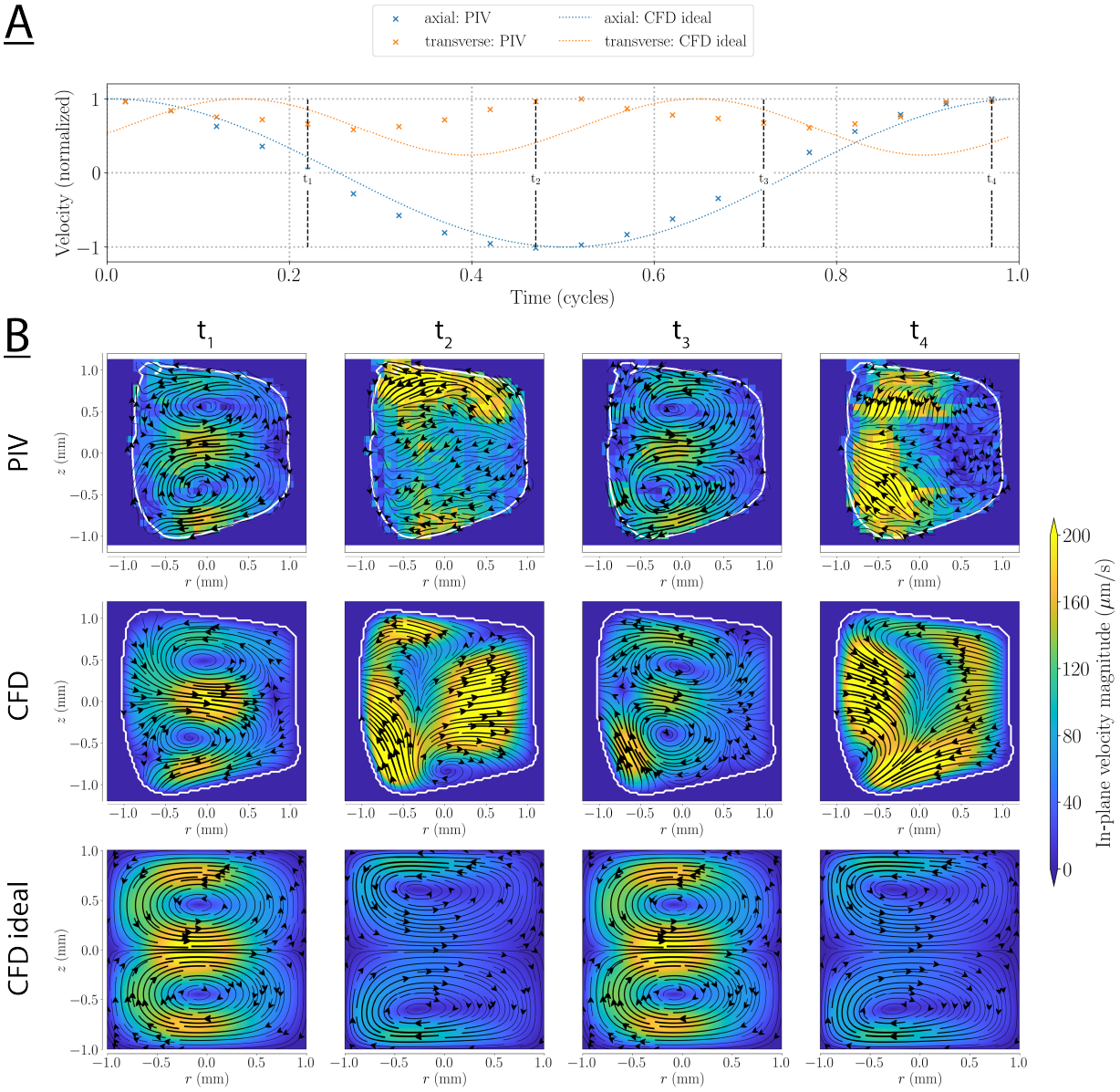

Fig. 4.10. (A) Mean axial and transverse velocities for an oscillation frequency of 5 Hz in the toroidal duct. The vertical lines indicate the times at which the transverse flow patterns are shown in (B). (B) Transverse flows at different time points in one cycle. The inner wall of the curve is to the left.

Figures 4.10 and 4.11 show the instantaneous, transverse flow pattern in the toroidal and twisted duct, respectively, at different time points within one oscillation period. The reference time for this period corresponds to the maximum axial velocity.

For the toroidal ducts, counter-rotating Dean cells occur twice per cycle around the inflection point of the axial flow (t_1 and t_3), i.e., when the velocity reverses. The measured phase difference with the main flow is of approximately 80 degrees. The Dean cells rotate

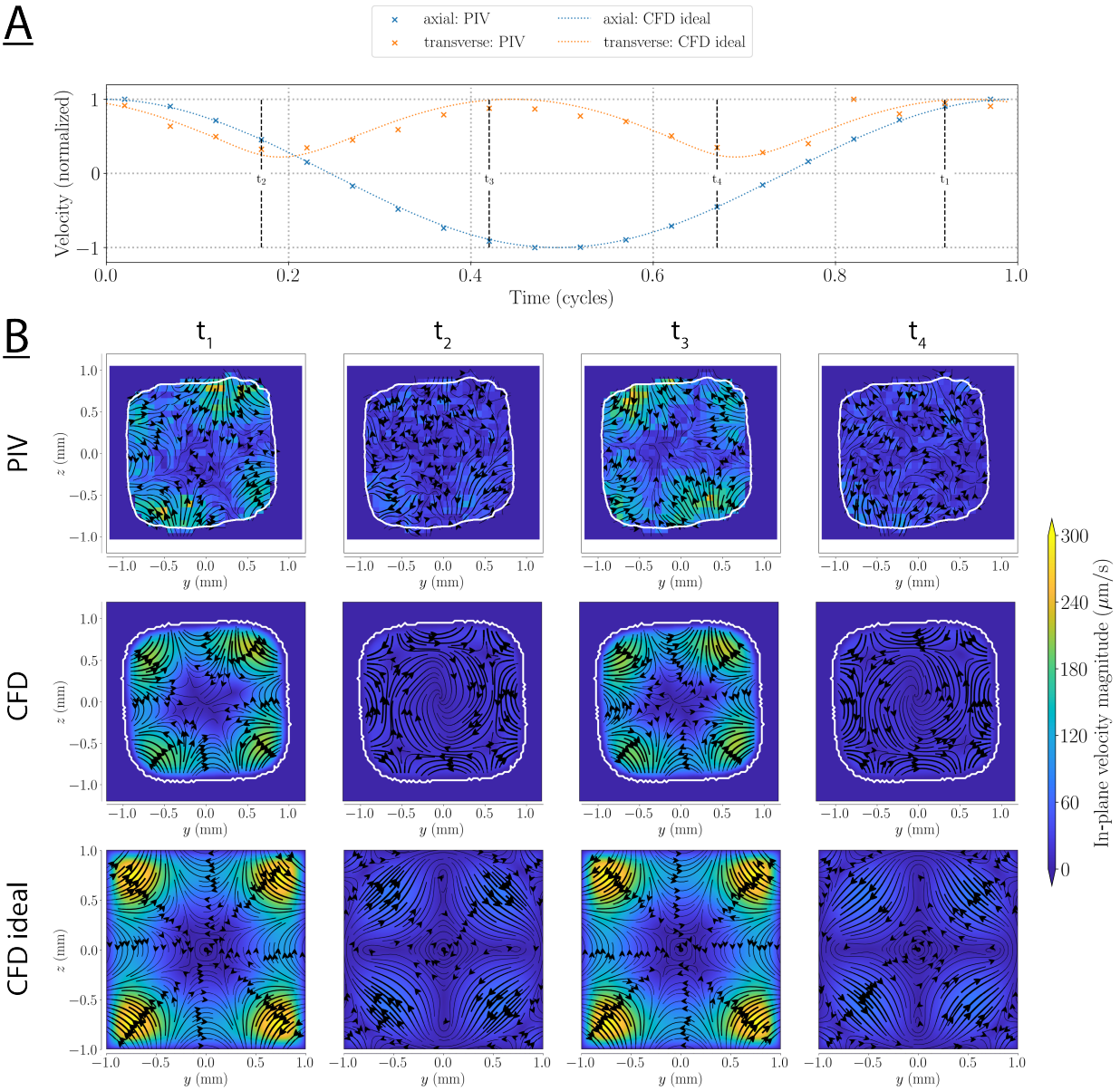

Fig. 4.11. (A) Mean axial and transverse velocities for an oscillation frequency of 5 Hz in the twisted duct. The vertical lines indicate the times at which the transverse flow patterns are shown in (B). (B) Transverse flows at different time points in one cycle. Looking into the page plane, the twisted duct turns clockwise and the axial velocity is inflowing for t_1 and outflowing for t_3.

in the same direction for inflowing and outflowing axial velocities (t_1 and t_3, respectively). However, irregularities in the real duct geometry produce slightly different patterns during inflow and outflow. When the axial flow is maximal (i.e., close to t_2 and t_4), the rotating cells appear to be concealed by stronger flows. These flows increase with the axial flow and are probably geometry-induced as they appear in both, the CFD model and the measurement, but not in the ideal-duct simulations. In these idealized models, the Dean cells have a phase lag of approximately 55 degrees relative to the maximum axial flow. Consequently, they reach their maximum strength before t_1 and t_3 which is a significant difference with the

measurements. We suspect that the shift in the phase lag compared to the real geometry, originates from the fact that at 55 degrees the Dean cells are concealed in the real geometry. In contrast to the ones in the measured models, the Dean cells in the ideal model are present throughout the entire cycle, changing only in magnitude.

In twisted ducts, the transverse flow patterns are strongest at t_1 and t_3, see Fig. 4.11. The typical saddle flow structure emerges near the walls and corners at these times. Most importantly, unlike the Dean cells, the saddle flow structure changes direction for inflowing and outflowing axial velocities. The transverse flow pattern is similar in the idealized and geometry-specific CFD unlike the weaker net motion, since this net flow is the residual of the near cancelation of this alternating flow. At 5 Hz, the saddle flow structure has a phase difference of approximately 20 degrees to the axial flow in all three models. Features of the saddle flow structure are distinguishable throughout most of the cycle, even in the PIV results. Although the transverse velocities in the twisted duct are higher than the Dean flow in the toroidal duct, the agreement with the simulation is comparatively more limited.

Maximal dynamic transverse flow

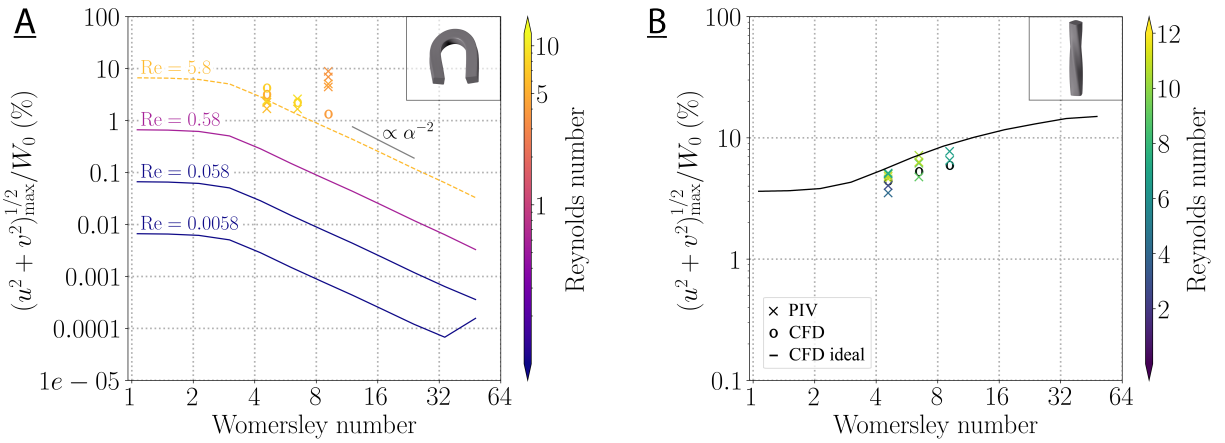

Fig. 4.12. Maximal transverse flow with respect to the mean axial flow amplitude W_0 as a function of the Womersley number α for the toroidal (A) and the twisted duct (B). The crosses indicate the PIV measurements, the circles denote the simulations in the geometry-specific measurement models, and the lines show the idealized CFD results from [200]. The lines for different Reynolds numbers (0.0058-0.58) are plotted on top of each other in the right image. The dashed line for $Re = 5.8$ is interpolated from the results at lower Reynolds numbers.

Fig. 4.12 compares the strength of the maximal transverse flows with idealized model data [200]. We varied the flow amplitudes in the PIV measurements to test the expected transverse flow strength at different Reynolds numbers. The maximum Dean flow in the idealized toroidal duct scales with the square of the Reynolds number, while the saddle flow structure in the twisted duct is proportional to it since it is a kinematic effect [137]. Thus, the curves for different Reynolds numbers overlap for the twisted duct in Fig. 4.12B, but not for the toroidal duct. In the PIV measurements, we detected transverse flows down to 5% of the axial flow amplitude in the twisted duct and down to 2% of the axial flow amplitude in the toroidal duct at 5 Hz.

The maximum strength of the transverse flows in the twisted duct is lower than the data from the idealized simulation would suggest. The measured specimen has a higher torsion ($\tau = 1/6\,\mathrm{mm}^{-1}$) than the idealized models did ($\tau = 1/8\,\mathrm{mm}^{-1}$). Bolinder [137] found that the maximum strength of the transverse flows is proportional to $\tau d_h Re$ in twisted ducts under steady scenarios, where d_h is the hydraulic diameter. Therefore, we would expect the measured sample to have even higher, by a factor of $8/6 = 1.333$, transverse flows. However, the idealized square cross-section has a greater distance from the center to the corners than the real cross-section. We suspect this to counteract the change in torsion.

Within the toroidal duct, we identified the maximum transverse flows during time instances when the Dean cells were fully developed, i.e., t_1 and t_3 in Fig. 4.10 for the PIV measurements and the geometry-specific CFD. At 5 and 10 Hz the magnitude of the Dean flows is similar to the expected one. Some measurements are on the higher side, which could be due to geometry induced flows that enhances the maximum transverse flows. At 20 Hz, the PIV measurements yielded much higher maximal transverse flows than expected from the CFD results because the Dean flow was below the limit of detection in the PIV data.

In the idealized simulations, the strength of the Dean cells decreases with the frequency and with the square of the axial flow for sufficiently high Womersley numbers according to Harte et al. [200]. This is consistent with the PIV measurements.

4.5 Discussion

3D-PIV system validation

Our 3D-PIV system offers several advantages. It is cost-effective, requiring only one camera and one optical access for the laser. The proposed single camera system is especially beneficial when working with small-scale models as it simplifies the setup and calibration processes. In addition, it allows the measurement of transverse flows from a side or top view, without the need to directly capture the transverse plane, which would be challenging, especially in the case of a twisted duct. Finally, the associated optical system allows for a depth of field comparable to or larger than the field of view, which allows for imaging specimens with large aspect ratios.

Nonetheless, the system also presents its limitations. While the transverse flow patterns were clearly recognized in PIV analysis at low oscillation frequencies (5 and 10 Hz), they were either close or below the noise floor for 20 Hz. This is attributed to the combined effect of their decreasing magnitude and the increasing experimental noise for higher frequencies. At higher frequencies, the transducer produced a lower flow amplitude and smaller particle displacement, which is suboptimal for PIV analysis. At the same time, higher frame and scan rates are required to obtain a sufficient number of frames per period. To compensate for the shorter exposure time, we opened the aperture more, resulting in less depth of field in the scan direction. This is the main technical limitation of the study.

Here, the stroboscopic PIV analysis was implemented for transverse net motions, therefore no axial net motion is evaluated since it was outside our scope of interest. While this axial net flow is probably not substantial in the toroidal duct, see e.g., Zabielski & Mestel [135], the twisted duct may have an axial net flow component. The method, however, can be readily extended by performing the PIV analysis in the orthogonal planes aligned with the channel axis. Furthermore, the SNR of the method could be further increased by performing the analysis at each recorded phase in the driving period and averaging the result.

Sample imperfections and net transverse flow

We have observed large differences between the transverse flow patterns in ideal geometries and in the measured samples. We attribute these differences to uneven sample walls and, more importantly, rounded corners. However, these differences are not artifacts since they are recovered by the geometry specific CFD simulations. For example, in the twisted duct, the observed flow through the center probably results from variations in the twist and the curvature of the centerline itself. Addressing this would be quite an experimental challenge. In addition, the tilt of the axis between the Dean cells in the toroidal duct is not present in the idealized model. Such effects are particularly relevant for physiological structures

such as the cochlea, which are intricate geometries with torsion, curvature, and varying cross-sections.

We suspect that the transverse net motion in the twisted duct originates from the Stokes drift, as the Lagrangian mean velocity significantly exceed the corresponding Eulerian mean velocities (in the simulations). The Stokes drift arises from the oscillatory characteristics of the saddle flow structure and local gradients in the axial velocity. During the first half of the oscillation cycle, the particles move in one direction, only to inverse their direction during the second half. Since the initial position of the particle is not exactly the same during these two halves, the particle experiences different forces from the local flow field. This mismatch causes a net drift. The Stokes drift is inversely related to the oscillation frequency, according to Edom et al. [5]. We also observed that these net motions decrease with the oscillation frequency in the ideal geometries.

Alignment and dynamic transverse flow

Notably, the Dean cells in the measured models were only pronounced at two instances per cycle, and they were even less distinguishable at higher frequencies in CFD. This may be due to three reasons. First, the geometric differences between the idealized models and the measurement models could cause additional flows, that are overlaid with the transverse flows. Second, it could be due to their sensitivity to the orientation of the transverse plane; even a small deviation in the plane orientation during post-processing causes a part of the axial flow to be inaccurately defined as transverse, resulting in an overlap with the actual transverse flow. Third, they may still be developing in the measurement models and therefore may still be subjected to entry length effects.

The transverse flow presented for the twisted duct are averaged over a short axial distance. However, the twisted duct displays a continuous twist, and this average may thus impact the reconstructed flow field. The quantitative comparison with the geometry specific CFD model suggests that the influence is limited. Nonetheless, implementing corrections such as a rotating reference frame to account for the rotating cross-section could improve the results for the twisted duct, potentially down to the order of parts per thousand with respect to the axial flow.

Potential physiological implications

The observed cross-sectional Lagrangian streaming may be of interest for mixing and mass transport in small enclosed systems such as the cochlea. Streaming velocities decreased with oscillation frequency in both curved and twisted channels. This suggests that mass transport induced by the geometry may be more prominent at low stimulation frequencies. This is in line with Edom et al. [5], who characterized steady streaming in the cochlea which, inter alia, originated from fluid structure interaction with the vibrating basilar membrane. They also indicated that streaming is predominantly relevant to the low-frequency hearing process. Frequencies in the infrasonic regime (i.e., below 16 Hz) are not considered audible, they can, however, still lead to fluid motion in the cochlea. In addition to passive diffusion, steady streaming could help transport ions and metabolites throughout the cross-section. This is important as the structure that secretes ions into the endolymph is located at the

outer wall of the spiral duct, from where they need to move to the surrounding tissues and sensory hair cells.

4.6 Conclusion

We developed a scanning 3D-PIV system for small-scale oscillatory flows, resolving subtle transverse flows at a fraction of the main axial flow amplitude. The axial flow amplitudes were varied between 3 and 8 mm/s. We applied the system to three millimetric geometries: a straight square duct, a twisted square duct, and a toroidal duct with a trapezoidal cross-section. Curvature and torsion lead to time-resolved transverse flows (Dean cells, saddle flow structure) and time-averaged net motions. The net motion in the toroidal duct, i.e., Dean flow, was stronger and thus easier to visualize than the one in the twisted duct. The detected net motions were approximately 1% of the axial flow in the toroidal duct and about an order of magnitude lower in the twisted duct. We measured time-resolved transverse flows down to 5% of the axial flow amplitude in the twisted duct and down to 2% of the axial flow amplitude in the toroidal duct at 5 Hz.

4.7 Acknowledgement

The authors would like to thank the Swiss National Science Foundation (Grant No. 205321_200850), the European Research Council (ERC-2022-STG Super-FALCON, No. 101076844), and the 4TU Precision Medicine program supported by High Tech for a Sustainable Future for providing financial support to this project. We further thank the FRIDERICUS Foundation, the Burgergemeinde Bern, and the Saly Frommer Foundation for supporting the project. We would like to thank Dr. Ashkan Ghanbarzadeh-Dagheyan for the many helpful discussions and for performing CT scans of the models along with Remco Liefers. We also thank Dieuwertje Alblas for reconstructing the flow channel using implicit neural representations [228]. We further thank Tobias Weber and Jan Schulte for measuring the PDMS layer thickness. Our special thanks go to David Sprecher, who helped to develop the flow setup.

4.8 Appendix

System calibration

Laser sheet thickness

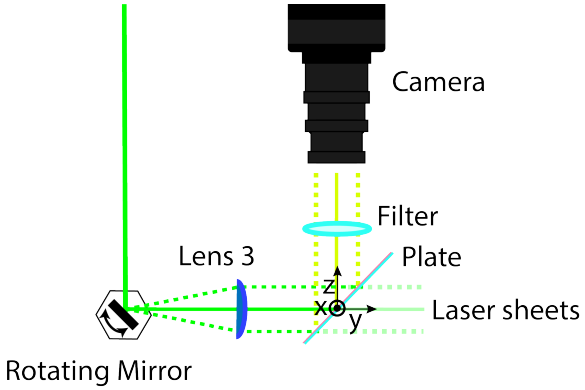

Fig. 4.13. Setup for calibration.

To characterize the laser sheet, we used a glass plate with a thin layer of PDMS mixed with fluorescent Nile Red. The plate was fixed at a 45° angle to the laser and camera, see Fig. 4.13. The plate was scanned with the laser sheet, as in the measurements, and the camera consequently captured images at different heights z and positions y along the plate. We used a laser scan rate of 200 Hz and a camera frame rate of 40000 fps. Figure 4.14B shows the height of the laser sheet as a function of time, which reveals the sawtooth function used to control the laser height. Note that the height corresponds to the y coordinate as the plate is at a 45° angle to the laser and camera. Figure 4.14A shows the line of the laser sheet at one height and Fig. 4.14C shows the intensity profile over it at different x-position. The beam was assumed to be Gaussian and its width was defined as the width at $1/e$ times the maximum intensity:

$$\delta_{1/e} = 1/\sqrt{-\ln(0.5)}\, FWHM \approx 1.2\, FWHM, \tag{4.2}$$

where $FWHM$ is the full width at half of the maximum intensity. The $FWHM$ was obtained from a Gaussian fit of the intensity profile in Fig. 4.14C.

The beam width is larger than the laser sheet thickness, because of the non-zero layer thickness of the PDMS. We measured the PDMS layer thickness δ_{PDMS} with confocal laser scanning microscopy to be $13 \pm 0.7\,\mu$m. To correct for this, the laser sheet thickness δ_l was calculated as

$$\delta_l = \delta_{1/e} - \sqrt{2}\delta_{PDMS}. \tag{4.3}$$

We used the median beam width over the x-direction. Figure 4.14D shows the resulting laser sheet thickness and the original beam width as a function of the height. The minima correspond to the layer where the focus of the camera system is best and the measured thickness increases below and above due to optical distortions. The laser sheet thickness was thus approximately $\delta_{1/e} = 31.9\,\mu$m before correction and $\delta_l = 13.5 \pm 0.9\,\mu$m after correction with the thickness of the PDMS layer.

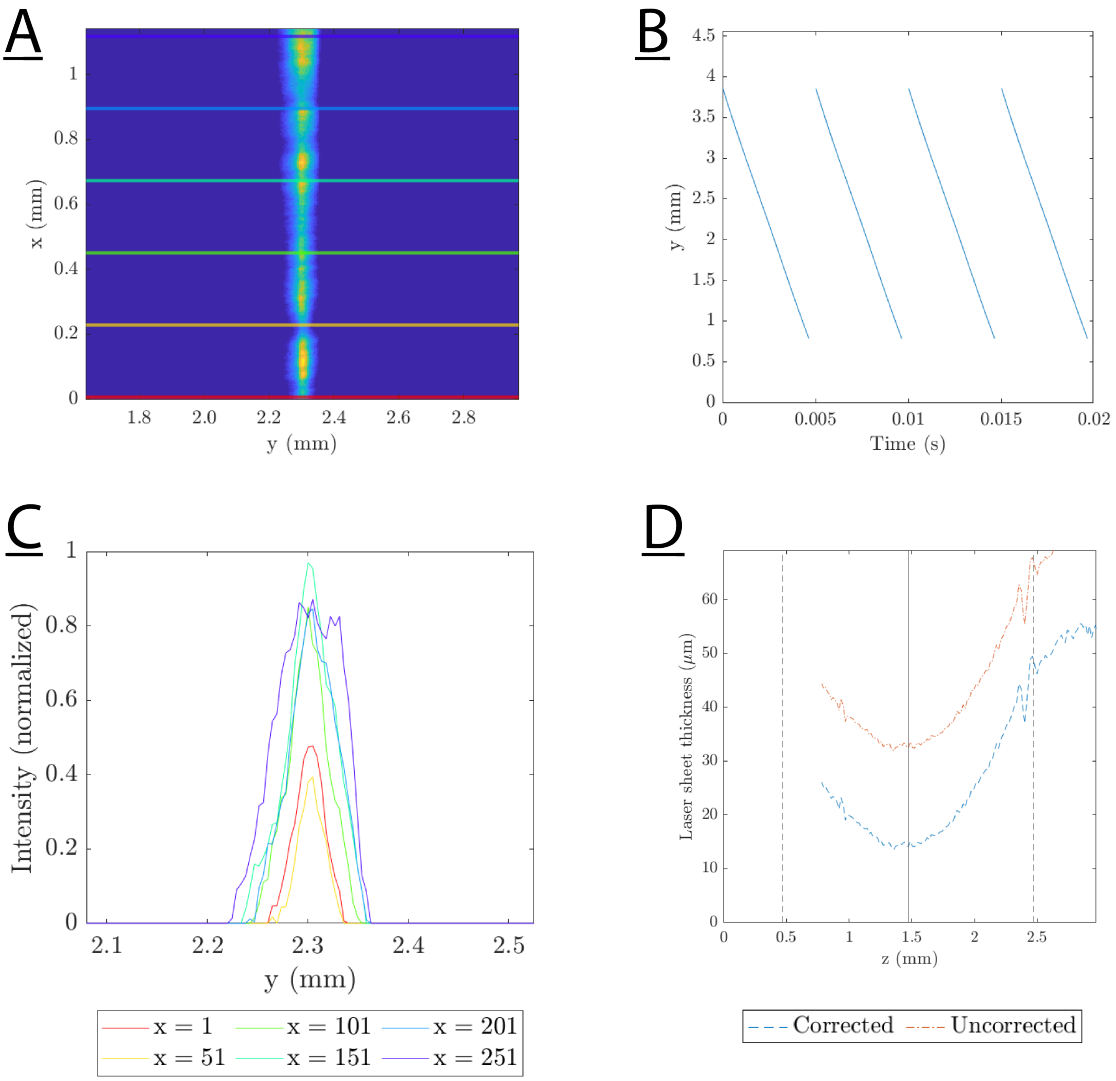

Fig. 4.14. Laser sheet characteristics. (A) Image of the laser sheet as captured by the high-speed camera. (B) Position of the laser sheet as a function of time. (C) Intensity over the image of the laser sheet at different widths across the measured plate. (D) Laser sheet thickness before (red) and after (blue) correction with the PDMS layer thickness. The solid vertical line indicates the z position where focus is best, while the dashed lines indicate the borders of the test section.

Scanning rate and inter-slice distance

We used a 1951 USAF resolution target, which contains line pairs of different sizes, to calibrate the PIV system. We recorded the target for different focal lengths of the reversed macro lens. The resolution was interpolated quadratically between the measured focal lengths to determine their dependence (Fig. 4.15). In the PIV analysis, we then used the interpolated function to related the focal lengths set in the measurements to the corresponding pixel resolution.

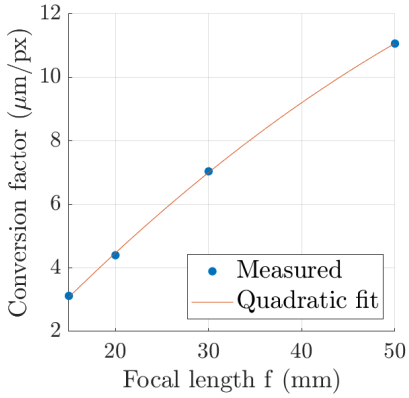

Fig. 4.15. Conversion factor from pixels to micrometers for different focal lengths of the frontal lens.

The different sawtooth function amplitudes, i.e., laser amplitudes, scale linearly with the distances between the captured layers in the z-direction. The total scan height per amplitude was approximately 3.75 μm/mV (Fig. 4.16). For example, for 200 layers and 800 mV, the median distance between the layers was approximately $15.09 \pm 1.66\,\mu$m. This leads to a spatial imaging resolution of approximately $5 \times 5 \times 15\,\mu\text{m}^3$ for a typical focal length of 22 mm.

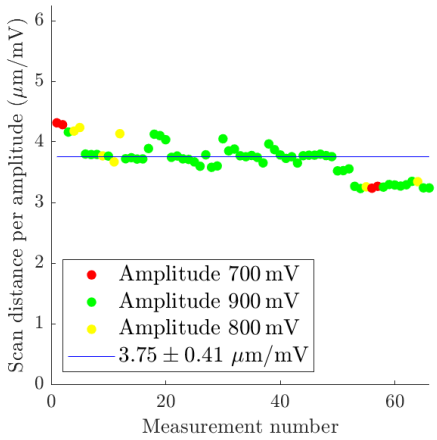

Fig. 4.16. Scan distance per amplitude of the sawtooth function (laser amplitude) for different calibration measurements. The solid blue line shows the median distance per amplitude.

Dynamic axial and transverse flows for higher frequencies

Figures 4.18 and 4.17 show the time-resolved, dynamic axial and transverse velocities in the twisted and toroidal duct, respectively, at one time point. The axial velocity is shown at its maximum. The transverse velocities are shown at the time when they are most developed.

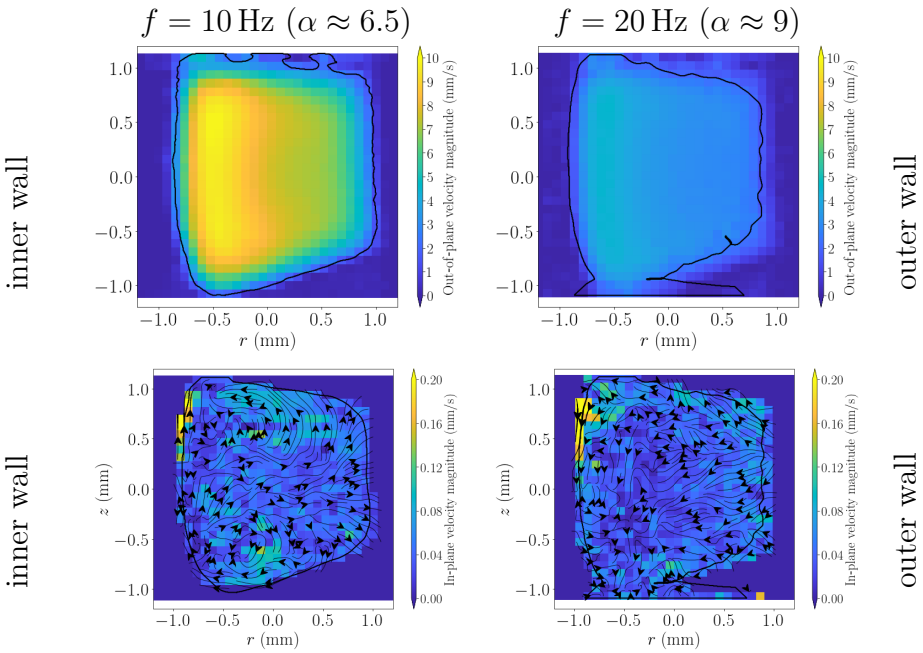

Fig. 4.17. Dynamic axial (first row) and transverse flow (second row) in the toroidal duct.

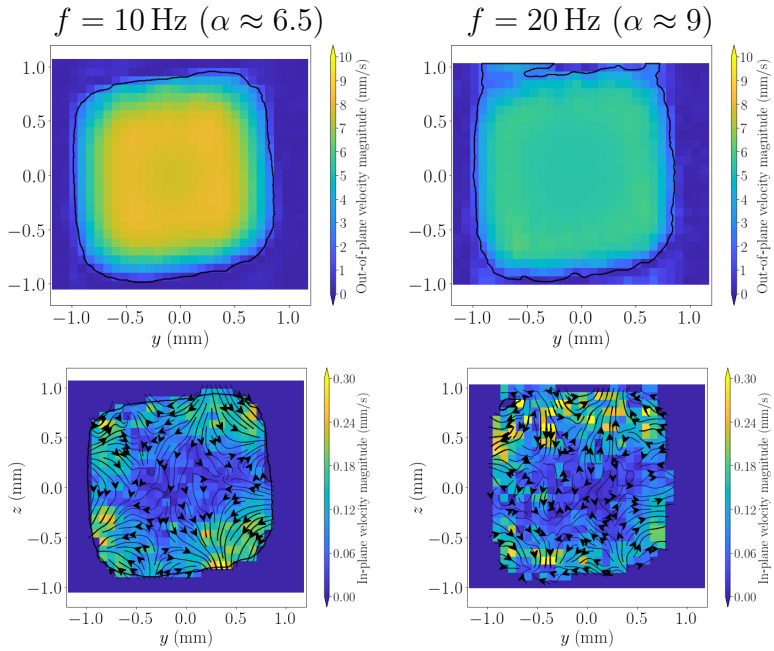

Fig. 4.18. Dynamic axial (first row) and transverse flow (second row) in the twisted duct.

CHAPTER 5

CONCLUSIONS AND OUTLOOK

This chapter provides an overall summary of the work presented in this thesis. The contributions and limitations of the three research projects are discussed and future work is outlined.

This thesis addresses the effect of geometry on transverse flow phenomena under oscillating flows with small amplitudes. Our hypothesis is that torsion facilitates low frequency hearing. In a first part, computational fluid dynamics (CFD) was employed to quantify transverse flows in helical square ducts. Dependencies of the emerging phenomena on the two relevant dimensionless numbers, the Womersley number α and the Reynolds number Re, were then characterized. They describe the transient inertial force as well as the inertial force with respect to the viscous force, respectively. In the second part, a measurement setup was developed to visualize these subtle transverse flows in physical models. The use of two unique, complementary particle image velocimetry (PIV) analysis methods allowed to capture both time-resolved velocities and net flows. Finally, combining insights from these two perspectives allowed us to quantify the extent to which the PIV captured the transverse flows, and to outline differences between ideal models and measured samples.

5.1 CFD visualizations and wall shear stresses

An existing kinematic surface fitting algorithm by Wimmer et al. [113] was adapted and used to build structured meshes along a centerline, which can either be user defined or determined by shape parameters extracted from micro-CT data. In Chapter 2 this method was applied to generate meshes of a straight, a toroidal, a twisted, and a helical duct for use in CFD. This method further offers a convenient and effective way to decompose the flow field into axial and transverse components, since it uses the Frenet-Serret frame, where the tangent to the centerline defines the axial direction. The transverse flow patterns that emerge from curvature, i.e., Dean cells, and from torsion, i.e., saddle flow structures, are presented in Chapter 2. While the Dean cells occurred with a substantial phase lag to the axial flow, the maximum saddle flow structure preceded it. In the helical duct, torsion dominated the transverse flow pattern at low Reynolds numbers.

Two new findings are highlighted in this chapter: First, we extended the dependence of maximal transverse flows on the Reynolds number, shown by Bolinder [137], to their dependence on the Womersley number, i.e., oscillation frequency. We were able to demonstrate that the combined effect of curvature and torsion in the helical duct results in a transverse flow that exceeds in magnitude what would be expected from the superposition of the two effects. Second, we present results of oscillating low Reynolds number flow tailored to the cochlea. Other studies investigating pipe flow in the biological context, are, in contrast, often geared towards application in the aorta. These flows have different characteristics (e.g., higher viscosity, shear thinning), are usually studied under pulsating flow with a single frequency (i.e., the heartbeat with $\alpha \approx 20$ in the aorta, e.g., [135]), and have larger vessel diameters and higher Reynolds numbers.

In Chapter 3, the numerical setup was applied to examine pressure fluctuations and wall shear stresses along the cross-section. Both are closely related with the previous results. Pressure differences across the cross-section are prominent drivers of transverse flow, and their behavior in magnitude and pattern is reflected in them. Moreover, torsion predominately affected the transverse flow velocities and in turn lead to high transverse

wall shear stresses. Curvature, in contrast, dominated the axial velocity profile, and thus also strongly influenced the axial wall shear stress.

In addition, two regimes were identified based on the Womersley number, which allowed to get a clearer understanding of the dominating effects in each geometry. While they were discussed for the wall shear stress and pressure fluctuations in Chapter 3, these regimes also characterized the transverse flow velocities and phase lags with respect to pressure. Below a Womersley number of 4, the transverse velocities behaved similarly in twisted, toroidal, and helical ducts. Above, they diverged and hinted at a different force dominating their drive. For example, the centripetal force in the toroidal duct decreased with the oscillation frequency. The kinematic effects of torsion, in contrast, increased. At higher frequencies, the driving force (pressure) needs to be higher to cause the same velocity amplitudes (which were imposed in the simulations). The flow is therefore strongly accelerated and thus the effect of directional changes in the boundaries, e.g., rotation, increases as well. This could be the reason for the elevated importance of torsion at higher driving frequencies.

5.2 3D-PIV visualizations and complex cross-sections

Next, the numerical results were used to validate an experimental setup and to quantify its performance for measuring transverse flows. Namely, a scanning PIV setup geared towards measuring oscillating flows with small amplitudes was developed and combined with a stroboscopic and a semi-Lagrangian PIV analysis technique, which enabled the detection of transverse net flows down to 0.1% of the axial flow amplitude and time-resolved flows down to 2%. It addresses two shortcomings among current measurement systems: it can resolve *multi-scale* flows in *small* models.

The measurement models were formed by thermally bending ABS square rods into the desired shape and casting them in PDMS. Using acetone, the ABS was subsequently dissolved and the PDMS casting retained. The thermal shaping introduced considerable deviations (slightly varying twist and curvature, rounded corners, etc.) to the ideal models from Chapters 2 and 3. These differences lead to unique flow patterns, in particular, to asymmetrical Dean cells. In the context of the complex cross-sectional shapes of the cochlear scalae, these findings are interesting because they demonstrate the need for accurate representations in measurement models.

The PIV system brings its own limitations. The transverse flow patterns were challenging to detect at higher oscillation frequencies due to increased systematic noise and reduced flow rates. Higher oscillation frequencies require higher camera frame rates to obtain a sufficient temporal resolution. To compensate for the shorter exposure time, we enlarged the aperture, resulting in less depth of field in the scan direction. Compared to other systems for similar scales, however, the introduced system still offers significant advantages. Holographic and tomographic PIV, for example, need optical access from multiple viewing angles, increasing cost and complexity of the setup. Single camera applications like general defocusing and astigmatic particle tracking velocimetry are limited in particle densities and thus in their resolution, in particular, as overlapping particles in the images lead to uncertainties about the particle positions. Scanning PIV does not require low particle densities, as the layers are scanned sequentially. In addition, our single camera setup is cost-effective

and convenient to apply. In summary, scanning PIV is an adequate system for studying transverse flows in millimetric in vitro models, such as those of the cochlea.

5.3 Potential physiological implications

We used abstracted geometries to examine the fundamental properties of low-amplitude oscillatory flow. As we wanted to investigate the effects of torsion and curvature separately and to validate our results with literature [137], our models had a square cross-section. Despite this abstraction, we can still derive insights about the fluid dynamics in the highly complex anatomy of the human cochlea. In its context, we relate the square ducts to either the scala vestibuli or scala tympani. In our simulations we modelled the walls as rigid and neglected interactions between the cochlear chambers. In particular, we neglected the dynamics of the basilar membrane. Therefore, we consider the fluid motion in our models as an addition to the one expected from the displacement of the basilar membrane (which is especially important at the characteristic place). The cochlear scalae have a complex, non-square cross-section, which however still contains regions with sharp bends (e.g., the lateral wall of the scala vestibuli, adjacent to Reissner's membrane). The transverse flow pattern near the corners of our square duct models' cross-section can be translated to these locations. This allows to predict locations with maximal effects.

Our findings show that torsion in the helical geometry leads to high transverse flows (up to 31% of the main flow at 256 Hz), which in turn cause high transverse wall shear stresses. Interestingly, the highest shear stresses were found at the inner wall of the curve close to the corners. This relates to locations closer to the modiolus. The rigid walls in our simulations allow pressure and wall shear stresses to build up considerably. In a flexible geometry, wall shear stresses might be partly converted to motion of surrounding structures and membranes. For example, high wall shear stress along the Reissner's membrane might deform it in the direction of the shear. This could have two main effects: First, it could stretch or compress the membrane, affecting ion channels. Second, a deformation of the Reissner's membrane would displace fluid in the scala media. Flow in the scala media is interesting, as the oscillating fluid motion which is generated by the stapes displacement is primarily in the perilymph while the hair cells are located in the scala media. To quantify these two effects, fluid structure interactions would have to be taken into consideration. Our results do, therefore, not allow us to conclude if the observed transverse flows also enhance low-frequency hearing. Nevertheless, based on their proportion relative to the axial flow, the transverse flow magnitudes may be relevant in hearing physiology.

Besides the oscillating fluid motion that we considered, the stapes movement leads to a travelling wave on the basilar membrane. The basilar membrane displacement peaks at a frequency dependent position along the cochlea, i.e., the characteristic place, and stimulates hair cells located there. While transverse flows are very interesting for hair cell stimulation, due to their arrangement in the scala media, our primary focus is not yet on hair cells. The geometry induced transverse flows arise throughout the spiral cochlea, from the base until the characteristic place (and maybe even beyond) — with local variations based on the curvature and torsion. Their effect is thus not primarily at the characteristic place. The main impact of the observed transverse flows is therefore in mixing and metabolite transfer.

Our results indicate that net flow with diverse Dean cell shapes and sizes could occur in the cross-sections of the cochlea. Such Dean cells would be most pronounced at infrasound frequencies, which can, despite being below the audible frequency range, still induce fluid motion in the cochlea. Studies suggested that infrasound may play a role in fluid homeostasis of the endolymph [234, 235]. Interestingly, if Dean cells were to form in the scala media, they could lead to net flow from the outer wall along the organ of Corti and the Reissner's membrane, which could help in ion transportation from the stria vascularis to the hair cells. In the cochlea, the time-reversible nature of creeping flow ($Re < 1$) impedes mixing, emphasizing the importance of such steady streaming effects for mass transport.

5.4 Outlook and future work

Mean velocities and streaming

The PIV results addressed geometry-induced, cross-sectional net flow, but of no less interest is axial net flow for mass transport along the longitudinal axis. The current PIV analysis could be readily adapted to obtain streaming in the axial direction, e.g., by a stroboscopic analysis of planes at right angles to the transverse plane. Furthermore, we are currently examining steady streaming effects with CFD, including the Stokes drift, as well as Eulerian and Lagrangian streaming. While streaming in a toroidal duct occurs mainly within the cross-section, our preliminary results suggest that torsion can cause axial streaming. Especially intriguing to examine is the potential combination of Stokes drift (from torsion) and Dean flow (from curvature) in the helical geometry. In addition to commonly applied drugs for the inner ear, such as cortisone [7, 8] and ototoxic antibiotics [9], axial streaming might someday be relevant for gene therapies aimed at hair cell regeneration [236, 237].

Helical centerlines and anatomically more detailed models

Possible future directions to explore include models which consider fluid-membrane interactions, or which have an anatomically more realistic cross-section. The latter can either be constant or vary along the cochlear duct according to the shape of the cochlea as determined, for example, from micro-CT data. Along this line, a series of patient specific samples would be intriguing, especially regarding the wide interindividual variability in cochlear shape.

In Chapter 4, we presented comprehensive results for twisted and toroidal flow channels, but not for the helical one. We also measured the helical samples with our 3D-PIV setup, but the corresponding results are still preliminary as the determination of the transverse plane requires an additional, not yet implemented, post-processing step. In addition, the PIV analysis would need to be adapted to enable averaging along a curvilinear centerline to increase SNR.

Flow setup

The key challenge of the flow setup is to obtain a driving system that is suited in precision and yields high flow rates at a wide frequency range. This task is challenging, because

of the fluid's inertia. Our group is working on possible alternatives to the current single layer piezo actuator, including pumps with stacked piezo actuators and an underwater-transducer (loudspeaker). Another modification includes thermal heating, which has been implemented in our group but not yet applied in the measurements. Heating water to body temperature reduces its viscosity by roughly 30% compared to a temperature of 20 degrees Celsius.

5.5 Summary

In the cochlea, transverse flow phenomena may help to maintain the homeostasis of the endolymph and are thought to be involved in inner hair cell stimulation. Ducts with torsion alone, as well as in combination with curvature, exhibit significantly increased transverse flow and transverse wall shear stress, in comparison to toroidal ducts. Curvature, on the other hand, dominated the cross-sectional net motions. This implies that torsion as well as curvature can be expected to have a significant impact on secondary flow phenomena in the cochlea. Interestingly, many previous studies of cochlear flow neglected torsion. Despite their potential relevance, the observed transverse flows are small compared to the axial flow. The developed measurement setup allowed to measure transverse flows down to 2% and net motions down to 0.1% of the axial flow. Apart from its capacity to measure multi-scale flows, the presented single camera system is convenient to use and cost-effective, and thus overcomes limitations of current systems for small-scale applications.

Despite the active research areas of both cochlear modeling and transverse flows, future research combining them in realistic geometries is needed to unravel the physiological role of the spiral cochlea. I hope that the developed setup will contribute to future work on this project, and that the presented work will help to view the role of the cochlear morphology in causing fluid dynamical effects from a new perspective.

LIST OF TABLES

Table 2.1 Model parameters 30
Table 2.2 Simulation time 44

Table 4.1 Measurement parameters 62

LIST OF FIGURES

Fig. 1.1 Phylogenetic radiation of the form of the auditory papilla in amniote vertebrates . . . 3
Fig. 1.2 Amniote phylogenetic tree over 500 million years . . . 4
Fig. 1.3 Coronal section through a right ear. . . . 5
Fig. 1.4 Left inner ear with the three ossicles . . . 6
Fig. 1.5 Axial section through a left cochlea. . . . 8
Fig. 1.6 Cross-section of the scala media and the organ of Corti . . . 9
Fig. 1.7 Soft tissue segmentation of ten cochleae . . . 10
Fig. 1.8 Primary and secondary flows in a curved pipe. . . . 16
Fig. 1.9 Meandering River. . . . 17
Fig. 1.10 Womersley flow profiles . . . 18
Fig. 1.11 Schematic of saddle flow structure . . . 19
Fig. 1.12 Schematics of Dean and Lyne cells . . . 19

Fig. 2.1 The geometries with corresponding curvature κ and torsion τ . . . 29
Fig. 2.2 Cross-sectional mesh . . . 31
Fig. 2.3 Axial flow magnitude for different frequencies and geometries . . . 33
Fig. 2.4 Location of maximum axial and transverse flow . . . 34
Fig. 2.5 Axial and transverse flow for different frequencies and geometries . . . 35
Fig. 2.6 Maximum transverse flow magnitude with respect to the mean axial flow velocity as a function of the Womersley number . . . 37
Fig. 2.7 Phase difference between maximum axial and transverse flow velocity and pressure for different Womersley numbers . . . 37
Fig. 2.8 Axial and transverse flow for different oscillation frequencies and geometries 41
Fig. 2.9 Axial and transverse flow for different oscillation frequencies and geometries 42
Fig. 2.10 Maximal transverse flow magnitude as a function of the Womersley number 43
Fig. 2.11 Maximal transverse velocities with respect to the axial velocity versus the Reynolds number . . . 44

Fig. 3.1 Pressure fluctuations along a cross-section . . . 49
Fig. 3.2 Maximum wall pressure fluctuations . . . 50
Fig. 3.3 Axial wall shear stress along a cross-section . . . 51
Fig. 3.4 Transverse wall shear stress along a cross-section . . . 52
Fig. 3.5 Maximum transverse wall shear stress with respect to the mean axial wall shear stress . . . 53

Fig. 4.1 Flow channels . . . 60
Fig. 4.2 Schematics of the 3D-PIV measurement setup and stacked images of raw data . . . 61
Fig. 4.3 Particle image velocimetry analysis overview . . . 63

Fig. 4.4 Velocity transformation from 2D Cartesian to polar coordinates 65
Fig. 4.5 Particle motion and reconstructed average displacement 66
Fig. 4.6 In-plane velocities in a central measurement plane 68
Fig. 4.7 Axial velocity 69
Fig. 4.8 Transverse net motion (Lagrangian streaming) in the toroidal duct 71
Fig. 4.9 Transverse net motion (Lagrangian streaming) in the twisted duct 72
Fig. 4.10 Dynamic transverse flows at different times in the toroidal duct 73
Fig. 4.11 Dynamic transverse flows at different times in the twisted duct 74
Fig. 4.12 Maximal transverse flow with respect to the mean axial flow amplitude as a function of the Womersley number 76
Fig. 4.13 Setup for calibration 80
Fig. 4.14 Laser sheet characteristics 81
Fig. 4.15 Conversion factor from pixels to micrometers 82
Fig. 4.16 Scan distance per amplitude of the sawtooth function 82
Fig. 4.17 Dynamic axial and transverse flow for the toroidal duct 83
Fig. 4.18 Dynamic axial and transverse flow for the twisted duct 83

REFERENCES

[1] Deafness and hearing loss. `https://www.who.int/news-room/fact-sheets/detail/deafness-and-hearing-loss`. Accessed: 2023-07-26.

[2] Olusanya BO, Neumann KJ, & Saunders JE. The global burden of disabling hearing impairment: a call to action. *Bulletin of the World Health Organization* 2014; 92.

[3] Olusanya BO, Davis AC, & Hoffman HJ. Hearing loss: Rising prevalence and impact. *Bulletin of the World Health Organization* 2019; 97.

[4] Sumner L, Mestel J, & Reichenbach T. Steady streaming as a method for drug delivery to the inner ear. *Scientific Reports* 2021; 11.1:57.

[5] Edom E, Obrist D, & Kleiser L. Steady streaming in a two-dimensional box model of a passive cochlea. *Journal of Fluid Mechanics* 2014; 753:254–278.

[6] Salt AN & Hirose K. Communication pathways to and from the inner ear and their contributions to drug delivery. *Hearing Research* 2018; 362.

[7] Chandrasekhar SS, Do BST, Schwartz SR, et al. Clinical Practice Guideline: Sudden Hearing Loss (Update). *Otolaryngology - Head and Neck Surgery (United States)* 2019; 161.

[8] Daneshi A, Jahandideh H, Pousti SB, & Mohammadi S. One-shot, low-dosage intratympanic gentamicin for Ménière's disease: Clinical, posturographic and vestibular test findings. *Iranian journal of neurology* 2014; 13.

[9] Bremer HG, van Rooy I, Pullens B, et al. Intratympanic gentamicin treatment for Ménière's disease: A randomized, double-blind, placebo-controlled trial on dose efficacy - results of a prematurely ended study. *Trials* 2014; 15.

[10] Manley GA. Comparative Auditory Neuroscience: Understanding the Evolution and Function of Ears. *JARO - Journal of the Association for Research in Otolaryngology* 2017; 18.

[11] Hachmeister JE. An abbreviated history of the ear: From Renaissance to present. *Yale Journal of Biology and Medicine* 2003; 76.

[12] Manley GA. Cochlear mechanisms from a phylogenetic viewpoint. *Proceedings of the National Academy of Sciences of the United States of America* 2000; 97.22:11736–11743.

[13] Walsh SA, Barrett PM, Milner AC, Manley G, & Witmer LM. Inner ear anatomy is a proxy for deducing auditory capability and behaviour in reptiles and birds. *Proceedings of the Royal Society B: Biological Sciences* 2009; 276.

[14] Fettiplace R. Diverse Mechanisms of Sound Frequency Discrimination in the Vertebrate Cochlea. *Trends in Neurosciences* 2020; 43.

[15] Von Békésy G. Experiments in Hearing. McGraw-Hill series in psychology. New York: McGraw-Hill, 1960.

[16] Luo ZX, Ruf I, Schultz JA, & Martin T. Fossil evidence on evolution of inner ear cochlea in Jurassic mammals. Proceedings of the Royal Society B: Biological Sciences. Vol. 278. 2011.

[17] Pietsch M, Aguirre Dávila L, Erfurt P, Avci E, Lenarz T, & Kral A. Spiral Form of the Human Cochlea Results from Spatial Constraints. *Scientific Reports* 2017; 7.1:1–11.

[18] Heffner HE & Heffner RS. Hearing ranges of laboratory animals. *Journal of the American Association for Laboratory Animal Science* 2007; 46.

[19] Zeh DR, Heupel MR, Limpus CJ, et al. Is acoustic tracking appropriate for air-breathing marine animals? Dugongs as a case study. *Journal of Experimental Marine Biology and Ecology* 2015; 464.

[20] Warfield D. Chapter 2 - The Study of Hearing in Animals. Methods of Animal Experimentation. Ed. by Gay WI. Academic Press, 1973:43–141.

[21] West CD. The relationship of the spiral turns of the cochlea and the length of the basilar membrane to the range of audible frequencies in ground dwelling mammals. *Journal of the Acoustical Society of America* 1985; 77.

[22] Peter Dallos Arthur N. Popper RRF. The Cochlea. Springer Handbook of Auditory Research. Springer New York, NY, 1996.

[23] Moller H & Pedersen C. Hearing at low and infrasonic frequencies. *Noise and Health* 2004; 6.23:37–57.

[24] Sieber D, Erfurt P, John S, et al. Data descriptor: The openEar library of 3D models of the human temporal bone based on computed tomography and micro-slicing. *Scientific Data* 2019; 6.

[25] Aebischer P. SMART Insertions for Cochlear Implant Electrode Arrays. Doctoral Thesis. University of Bern, 2022.

[26] Stenfelt S. Acoustic and physiologic aspects of bone conduction hearing. *Advances in Oto-Rhino-Laryngology* 2011; 71:10–21.

[27] Ren LJ, Yu Y, Fang YQ, Hua C, Dai PD, & Zhang TY. Finite element simulation of cochlear traveling wave under air and bone conduction hearing. *Biomechanics and Modeling in Mechanobiology* 2021; 20:1251–1265.

[28] Reinfeldt S, Stenfelt S, Good T, & Håkansson B. Examination of bone-conducted transmission from sound field excitation measured by thresholds, ear-canal sound pressure, and skull vibrations. *The Journal of the Acoustical Society of America* 2007; 121.

[29] Stenfelt S & Håkansson B. Air versus bone conduction: An equal loudness investigation. *Hearing Research* 2002; 167.

[30] Ugarteburu M, Withnell RH, Cardoso L, Carriero A, & Richter CP. Mammalian middle ear mechanics: A review. *Frontiers in Bioengineering and Biotechnology* 2022; 10.

[31] Killion MC & Dallos P. Impedance matching by the. combined effects of the outer and middle ear. *Journal of the Acoustical Society of America* 1979; 66.

[32] Jeught SVD, Dirckx JJ, Aerts JR, Bradu A, Podoleanu AG, & Buytaert JA. Full-field thickness distribution of human tympanic membrane obtained with optical coherence tomography. *JARO - Journal of the Association for Research in Otolaryngology* 2013; 14.

[33] Zdilla MJ, Skrzat J, Kozerska M, Leszczyński B, Tarasiuk J, & Wroński S. Oval window size and shape: A Micro-CT anatomical study with considerations for stapes surgery. *Otology and Neurotology* 2018; 39.

[34] Gerber N, Reyes M, Barazzetti L, et al. Data Descriptor: A multiscale imaging and modelling dataset of the human inner ear. *Scientific Data* 2017; 4.

[35] Koch M, Eßinger T, Maier H, et al. Methods and reference data for middle ear transfer functions. *Scientific reports* 2022; 12.1:1–17.

[36] Thompson CW, Rohani SA, Dirckx JJ, Ladak HM, & Agrawal SK. Finite element modelling of the human middle ear using synchrotron-radiation phase-contrast imaging. *Computers in Biology and Medicine* 2023; 157.

[37] Gan RZ, Reeves BP, & Wang X. Modeling of sound transmission from ear canal to cochlea. *Annals of Biomedical Engineering* 2007; 35.

[38] Gan RZ, Feng B, & Sun Q. Three-dimensional finite element modeling of human ear for sound transmission. *Annals of Biomedical Engineering* 2004; 32.

[39] Areias B, Santos C, Jorge RMN, Gentil F, & Parente MP. Finite element modelling of sound transmission from outer to inner ear. *Proceedings of the Institution of Mechanical Engineers, Part H: Journal of Engineering in Medicine* 2016; 230.

[40] Greene NT, Jenkins HA, Tollin DJ, & Easter JR. Stapes displacement and intracochlear pressure in response to very high level, low frequency sounds. *Hearing Research* 2017; 348.

[41] Gan RZ, Wood MW, & Dormer KJ. Human middle ear transfer function measured by double laser interferometry system. *Otology and Neurotology* 2004; 25.

[42] Aibara R, Welsh JT, Puria S, & Goode RL. Human middle-ear sound transfer function and cochlear input impedance. *Hearing research* 2001; 152.1-2:100–109.

[43] Hato N, Stenfelt S, & Goode RL. Three-dimensional stapes footplate motion in human temporal bones. *Audiology and Neuro-Otology* 2003; 8.

[44] Sim JH, Chatzimichalis M, Lauxmann M, Röösli C, Eiber A, & Huber AM. Complex stapes motions in human ears. *JARO - Journal of the Association for Research in Otolaryngology* 2010; 11.3:329–341.

[45] Edom E, Obrist D, Henniger R, Kleiser L, Sim JH, & Huber AM. The effect of rocking stapes motions on the cochlear fluid flow and on the basilar membrane motion. *The Journal of the Acoustical Society of America* 2013; 134.

[46] Obrist D. Flow Phenomena in the Inner Ear. *Annual Review of Fluid Mechanics* 2019; 51:487–510.

[47] Avci E, Nauwelaers T, Lenarz T, Hamacher V, & Kral A. Variations in microanatomy of the human cochlea. *Journal of Comparative Neurology* 2014; 522:3245–3261.

[48] Shin KJ, Lee JY, Kim JN, et al. Quantitative analysis of the cochlea using three-dimensional reconstruction based on microcomputed tomographic images. *Anatomical Record* 2013; 296.7:1083–1088.

[49] Meng J, Li S, Zhang F, Li Q, & Qin Z. Cochlear size and shape variability and implications in cochlear implantation surgery. *Otology and Neurotology* 2016; 37.9:1307–1313.

[50] Steele CR & Puria S. Cochlear Mechanics. The Biomedical Engineering Handbook. Ed. by Bronzino JD & Peterson DR. Fourth. Biomedical Engineering Fundamentals, 2014. Chap. 24:24-1 - 24–23.

[51] Felix H, Fraissinette AD, Johnsson LG, & Gleeson MJ. Morphological features of human reissner's membrane. *Acta Oto-Laryngologica* 1993; 113.

[52] Wimmer W. Multidisciplinary Approaches Toward an Improved Efficacy of Cochlear Implants. Doctoral Thesis. University of Bern, 2015.

[53] Von Békésy G. Traveling Waves as Frequency Analysers in the Cochlea. *Nature* 1970; 225:1207–1209.

[54] Voss SE, Rosowski JJ, & Peake WT. Is the pressure difference between the oval and round windows the effective acoustic stimulus for the cochlea? *The Journal of the Acoustical Society of America* 1996; 100:1602–1616.

[55] Lighthill J. Acoustic streaming in the ear itself. *Journal of Fluid Mechanics* 1992; 239:551–606.

[56] Hudspeth AJ. Integrating the active process of hair cells with cochlear function. *Nature Reviews Neuroscience* 2014; 15.

[57] Ciganović N, Warren RL, Keçeli B, Jacob S, Fridberger A, & Reichenbach T. Static length changes of cochlear outer hair cells can tune low-frequency hearing. *PLoS Computational Biology* 2018; 14.

[58] Reichenbach T & Hudspeth AJ. The physics of hearing: Fluid mechanics and the active process of the inner ear. *Reports on Progress in Physics* 2014; 77.

[59] Ashmore JF. A fast motile response in guinea-pig outer hair cells: the cellular basis of the cochlear amplifier. *The Journal of Physiology* 1987; 388.

[60] Brownell WE, Bader CR, Bertrand D, & Ribaupierre YD. Evoked mechanical responses of isolated cochlear outer hair cells. *Science* 1985; 227.

[61] Ciganović N, Wolde-Kidan A, & Reichenbach T. Hair bundles of cochlear outer hair cells are shaped to minimize their fluid-dynamic resistance. *Scientific Reports* 2017; 7.1:1–9.

[62] Warren RL, Ramamoorthy S, Ciganovic N, et al. Minimal basilar membrane motion in low-frequency hearing. *Proceedings of the National Academy of Sciences of the United States of America* 2016; 113.

[63] Greenwood DD. Critical Bandwidth and the Frequency Coordinates of the Basilar Membrane. *The Journal of the Acoustical Society of America* 1961; 33.

[64] Li H, Helpard L, Ekeroot J, et al. Three-dimensional tonotopic mapping of the human cochlea based on synchrotron radiation phase-contrast imaging. *Scientific Reports* 2021; 11.

[65] Thulasiram MR, Ogier JM, & Dabdoub A. Hearing Function, Degeneration, and Disease: Spotlight on the Stria Vascularis. *Frontiers in Cell and Developmental Biology* 2022; 10.

[66] Spyropoulos ITCS. Stria vascularis as source of endocochlear potential. *Journal of neurophysiology* 1959; 22.

[67] Patuzzi R. Ion flow in stria vascularis and the production and regulation of cochlear endolymph and the endolymphatic potential. *Hearing Research* 2011; 277.1:4–19.

[68] Wangemann P. Supporting sensory transduction: Cochlear fluid homeostasis and the endocochlear potential. *Journal of Physiology* 2006; 576.

[69] Kim SH & Marcus DC. Regulation of sodium transport in the inner ear. *Hearing Research* 2011; 280.

[70] Paolis AD, Bikson M, Nelson JT, de Ru JA, Packer M, & Cardoso L. Analytical and numerical modeling of the hearing system: Advances towards the assessment of hearing damage. *Hearing Research* 2017; 349.

[71] Obrist D. Fluid mechanics of the inner ear. en. Habilitation Thesis. Zürich: ETH Zurich, 2011.

[72] Peterson LC & Bogert BP. A Dynamical Theory of the Cochlea. *Journal of the Acoustical Society of America* 1950; 22:369–381.

[73] Lesser MB & Berkley DA. Fluid mechanics of the cochlea. Part 1. *Journal of Fluid Mechanics* 1972; 51.

[74] Steele CR & Taber LA. Comparison of WKB calculations and experimental results for three-dimensional cochlear models. *Journal of the Acoustical Society of America* 1979; 65.

[75] Yoon YJ, Puria S, & Steele CR. Intracochlear pressure and derived quantities from a three-dimensional model. *The Journal of the Acoustical Society of America* 2007; 122.

[76] Steele CR & Lim KM. Cochlear model with three-dimensional fluid, inner sulcus and feed-forward mechanism. *Audiology and Neuro-Otology* 1999; 4.

[77] Ranke OF. Theory of Operation of the Cochlea: A Contribution to the Hydrodynamics of the Cochlea. *Journal of the Acoustical Society of America* 1950; 22.

[78] Riley N. Steady Streaming. *Annual Review of Fluid Mechanics* 2001; 33.1:43–65.

[79] Gerstenberger C & Wolter FE. Numerical simulation of acoustic streaming within the cochlea. *Journal of Computational Acoustics* 2013; 21.4.

[80] Thompson C & Chandra K. Acoustic streaming resulting from compression of the cochlear bony capsule. *The Journal of the Acoustical Society of America* 2021; 150.6:4548–4557.

[81] Gold T & Gray J. Hearing. II. The physical basis of the action of the cochlea. *Proceedings of the Royal Society B: Biological Sciences* 1948; 135.

[82] Gold T, Pumphrey RJ, & Gray J. Hearing. I. The cochlea as a frequency analyzer. *Proceedings of the Royal Society B: Biological Sciences* 1948; 135.

[83] Kemp DT. Stimulated acoustic emissions from within the human auditory system. *Journal of the Acoustical Society of America* 1978; 64.

[84] Nin F, Reichenbach T, Fisher JA, & Hudspeth AJ. Contribution of active hair-bundle motility to nonlinear amplification in the mammalian cochlea. *Proceedings of the National Academy of Sciences of the United States of America* 2012; 109.

[85] Oghalai JS. The cochlear amplifier: Augmentation of the traveling wave within the inner ear. *Current Opinion in Otolaryngology and Head and Neck Surgery* 2004; 12.

[86] Kozlov AS, Baumgart J, Risler T, Versteegh CP, & Hudspeth AJ. Forces between clustered stereocilia minimize friction in the ear on a subnanometre scale. *Nature* 2011; 474.

[87] Zagadou BF, Barbone PE, & Mountain DC. Significance of the microfluidic flow inside the organ of corti. *Journal of Biomechanical Engineering* 2020; 142.

[88] Steele CR & Puria S. Force on inner hair cell cilia. *International Journal of Solids and Structures* 2005; 42.21:5887–5904.

[89] Guinan JJ. Cochlear amplification in the short-wave region by outer hair cells changing organ-of-Corti area to amplify the fluid traveling wave. *Hearing Research* 2022; 426.

[90] Shokrian M, Knox C, Kelley DH, & Nam JH. Mechanically facilitated micro-fluid mixing in the organ of Corti. *Scientific Reports* 2020; 10.

[91] Guinan JJ. Cochlear Mechanics, Otoacoustic Emissions, and Medial Olivocochlear Efferents: Twenty Years of Advances and Controversies Along with Areas Ripe for New Work. Ed. by Popper AN & Fay RR. Springer New York, 2014:229–246.

[92] Givelberg E & Bunn J. A comprehensive three-dimensional model of the cochlea. *Journal of Computational Physics* 2003; 191.2:377–391.

[93] Böhnke F & Arnold W. 3D-finite element model of the human cochlea including fluid-structure couplings. *ORL* 1999; 61.5:305–310.

[94] Viergever MA. Basilar membrane motion in a spiral-shaped cochlea. *Journal of the Acoustical Society of America* 1978; 64.4:1048–1053.

[95] Loh CH. Multiple scale analysis of the spirally coiled cochlea. *The Journal of the Acoustical Society of America* 1983; 74.1:95–103.

[96] Steele CR & Zais JG. Effect of coiling in a cochlear model. *Journal of the Acoustical Society of America* 1985; 77.5:1849–1852.

[97] Manoussaki D, Dimitriadis EK, & Chadwick RS. Cochlea's graded curvature effect on low frequency waves. *Physical Review Letters* 2006; 96.8:088701.

[98] Isailovic V, Nikolic M, Milosevic Z, et al. Finite element coiled cochlea model. AIP Conference Proceedings. Vol. 1703. 2015.

[99] Ren LJ, Hua C, Ding GH, Yang L, Dai PD, & Zhang TY. Three-dimensional finite element hydrodynamical modeling of straight and spiral cochlea. Vol. 1965. 2018.

[100] Yao W, Zhao Z, Wang J, & Duan M. Time-domain analysis of a three-dimensional numerical model of the human spiral cochlea at medium intensity. *Computers in Biology and Medicine* 2021; 136.

[101] Ma J & Yao W. Research on the distribution of pressure field on the basilar membrane in the passive spiral cochlea. *Journal of Mechanics in Medicine and Biology* 2014; 14.

[102] Zhao Z, Yao W, Wang M, Wang J, & Zhang T. Radial Flow Field of Spiral Cochlea and Its Effect on Stereocilia. *Journal of biomechanical engineering* 2022; 144.

[103] Yao W, Liang J, Ren L, et al. Revealing the actions of the human cochlear basilar membrane at low frequency. *Communications in Nonlinear Science and Numerical Simulation* 2022; 104.

[104] Zhang X & Gan RZ. A comprehensive model of human ear for analysis of implantable hearing devices. *IEEE Transactions on Biomedical Engineering* 2011; 58.

[105] Bradshaw JJ, Brown MA, Jiang S, & Gan RZ. 3D Finite Element Model of Human Ear with 3-Chamber Spiral Cochlea for Blast Wave Transmission from the Ear Canal to Cochlea. *Annals of Biomedical Engineering* 2023; 51.

[106] Brown MA, Bradshaw JJ, & Gan RZ. Three-Dimensional Finite Element Modeling of Blast Wave Transmission From the External Ear to a Spiral Cochlea. *Journal of biomechanical engineering* 2022; 144.

[107] Manoussaki D, Chadwick RS, Ketten DR, Arruda J, Dimitriadis EK, & O'Malley JT. The influence of cochlear shape on low-frequency hearing. *Proceedings of the National Academy of Sciences of the United States of America* 2008; 105.16:6162–6166.

[108] Manoussaki D & Chadwick RS. Effects of geometry on fluid loading in a coiled cochlea. *SIAM Journal on Applied Mathematics* 2000; 61.

[109] Cho A. Physiology. Math clears up an inner-ear mystery: spiral shape pumps up the bass. *Science* 2006; 311.

[110] Cai H, Manoussaki D, & Chadwick R. Effects of coiling on the micromechanics of the mammalian cochlea. *Journal of the Royal Society Interface* 2005; 2.2:341–348.

[111] Huxley AF. Is resonance possible in the cochlea after all? *Nature* 1969; 221.

[112] De Paolis A, Watanabe H, Nelson JT, Bikson M, Packer M, & Cardoso L. Human cochlear hydrodynamics: A high-resolution μCT-based finite element study. *Journal of Biomechanics* 2017; 50:209–216.

[113] Wimmer W, Vandersteen C, Guevara N, Caversaccio M, & Delingette H. Robust cochlear modiolar axis detection in CT. International Conference on Medical Image Computing and Computer-Assisted Intervention. Springer. 2019:3–10.

[114] Bolinder CJ. Curvilinear coordinates and physical components: An application to the problem of viscous flow and heat transfer in smoothly curved ducts. *Journal of Applied Mechanics, Transactions ASME* 1996; 63.4:985–989.

[115] Nivedita N & Papautsky I. Continuous separation of blood cells in spiral microfluidic devices. *Biomicrofluidics* 2013; 7.

[116] Erdem K, Ahmadi VE, Kosar A, & Kuddusi L. Differential sorting of microparticles using spiral microchannels with elliptic configurations. *Micromachines* 2020; 11.

[117] Balasubramaniam L, Arayanarakool R, Marshall SD, Li B, Lee PS, & Chen PC. Impact of cross-sectional geometry on mixing performance of spiral microfluidic channels characterized by swirling strength of Dean-vortices. *Journal of Micromechanics and Microengineering* 2017; 27.

[118] Khoshvaght-Aliabadi M, Arani Z, & Rahimpour F. Influence of Al2O3–H2O nanofluid on performance of twisted minichannels. *Advanced Powder Technology* 2016; 27.

[119] Rösch Y. Efficiency of intracoronary drug infusion into myocardial microcirculation with microvascular obstruction: in vitro study with a multiscale flow model. Doctoral Thesis. University of Bern, 2023.

[120] Rösch Y, Eggenberger D, Kuster Y, et al. Enhanced Drug Delivery for Cardiac Microvascular Obstruction with an Occlusion-Infusion-Catheter. *Annals of Biomedical Engineering* 2023; 51.

[121] Detra RW. The secondary flow in curved pipes. Doctoral Thesis. ETH Zurich, 1953.

[122] Shaheed R, Mohammadian A, & Yan X. A review of numerical simulations of secondary flows in river bends. *Water* 2021; 13.

[123] Pedley TJ & Kamm RD. The effect of secondary motion on axial transport in oscillatory tube flow. *Journal of Fluid Mechanics* 1988; 193:347–367.

[124] Ghanbarzadeh-Dagheyan A, Groot Jebbink E, Reijnen M, & Versluis M. Skewedness as a Signature of Dean Flow Measured by Echo-PIV. Proceedings of IEEE International Ultrasonics Symposium 2022. 2022.

[125] Einstein A. The Cause of the Formation of Meanders in the Courses of Rivers and of the So-Called Baer's Law. *Die Naturwissenschaften* 1926; 14.

[126] Thomson J. Bakerian Lecture: On the Grand Currents of Atmospheric Circulation. *Philosophical Transactions of the Royal Society of London. A* 1892; 183:653–684.

[127] Jakubowski M, Stachnik M, Sterczyńska M, et al. CFD analysis of primary and secondary flows and PIV measurements in whirlpool and whirlpool kettle with pulsatile filling: Analysis of the flow in a swirl separator. *Journal of Food Engineering* 2019; 258.

[128] Murata S, Miyake Y, & Inaba T. Laminar flow in a curved pipe with varying curvature. *Journal of Fluid Mechanics* 1976; 73.

[129] Liu S & Masliyah JH. Axially invariant laminar flow in helical pipes with a finite pitch. *Journal of Fluid Mechanics* 1993; 251.sl:315–353.

[130] Zabielski L & Mestel AJ. Steady flow in a helically symmetric pipe. *Journal of Fluid Mechanics* 1998; 370:297–320.

[131] Masliyah JH & Nandakumar K. Steady laminar flow through twisted pipes: Fluid flow in square tubes. *Journal of Heat Transfer* 1981; 103.

[132] Kheshgi HS. Laminar flow in twisted ducts. *Physics of Fluids A: Fluid Dynamics* 1993; 5.11:2669–2681.

[133] Wimmer W, Anschuetz L, Weder S, Wagner F, Delingette H, & Caversaccio M. Human bony labyrinth dataset: Co-registered CT and micro-CT images, surface models and anatomical landmarks. *Data in brief* 2019; 27:104782.

[134] Womersley JR. Method for the calculation of velocity, rate of flow and viscous drag in arteries when the pressure gradient is known. *The Journal of Physiology* 1955; 127.

[135] Zabielski L & Mestel AJ. Unsteady blood flow in a helically symmetric pipe. *Journal of Fluid Mechanics* 1998; 370:321–345.

[136] Dean WR. Fluid motion in a curved channel. *Proceedings of the Royal Society of London* 1928; 121.787:402–420.

[137] Bolinder CJ. First- and higher-order effects of curvature and torsion on the flow in a helical rectangular duct. *Journal of Fluid Mechanics* 1996; 314:113–138.

[138] Germano M. The Dean equations extended to a helical pipe flow. *Journal of Fluid Mechanics* 1989; 203.7:289–305.

[139] Lyne W. Unsteady viscous flow in a curved pipe. *Journal of Fluid Mechanics* 1971; 45.1:13–31.

[140] Sudo K, Sumida M, & Yamane R. Secondary motion of fully developed oscillatory flow in a curved pipe. *Journal of Fluid mechanics* 1992; 237:189–208.

[141] Tsangaris S & Vlachakis NW. Exact solution of the Navier-Stokes equations for the fully developed, pulsating flow in a rectangular duct with a constant cross-sectional velocity. *Journal of Fluids Engineering, Transactions of the ASME* 2003; 125.2:382–384.

[142] Dean W. Note on the motion of fluid in a curved pipe. *The London, Edinburgh, and Dublin Philosophical Magazine and Journal of Science* 1927; 4.

[143] Dean W. The stream-line motion of fluid in a curved pipe. *The London, Edinburgh, and Dublin Philosophical Magazine and Journal of Science* 1928; 5.

[144] Berger SA, Talbot L, & Yao LS. Flow in Curved Pipes. *Annual Review of Fluid Mechanics* 1983; 15.1:461–512.

[145] Siggers JH & Waters SL. Unsteady flows in pipes with finite curvature. *Journal of Fluid Mechanics* 2008; 600:133–165.

[146] Norouzi M & Biglari N. An analytical solution for Dean flow in curved ducts with rectangular cross section. *Physics of Fluids* 2013; 25.

[147] Chang KS, Choi JS, & Kim JS. Laminar fluid flow in a twisted elliptic tube. *KSME Journal* 1988; 2.

[148] Tuttle ER. Laminar flow in twisted pipes. *Journal of Fluid Mechanics* 1990; 219:545–570.

[149] Wang CY. On the low-Reynolds-number flow in a helical pipe. *Journal of Fluid Mechanics* 1981; 108.7:185–194.

[150] Murata S, Miyake Y, Inaba T, & Ogawa H. Laminar flow in a helically coiled pipe. *Bulletin of the JSME* 1981; 24.

[151] Germano M. On the effect of torsion on a helical pipe flow. *Journal of Fluid Mechanics* 1982; 125.7:1–8.

[152] Gammack D & Hydon PE. Flow in pipes with non-uniform curvature and torsion. *Journal of Fluid Mechanics* 2001; 433.

[153] Chen WH & Jan R. The torsion effect on fully developed laminar flow in helical square ducts. *Journal of Fluids Engineering, Transactions of the ASME* 1993; 115.

[154] Thomson DL, Bayazitoglu Y, & Meade AJ. Series solution of low Dean and Germano number flows in helical rectangular ducts. *International Journal of Thermal Sciences* 2001; 40:937–948.

[155] Sakalis VD, Hatzikonstantinou PM, & Papadopoulos PK. Numerical procedure for the laminar developed flow in a helical square duct. *Journal of Fluids Engineering, Transactions of the ASME* 2005; 127.1:136–148.

[156] Morales RE & Rosa ES. Modeling fully developed laminar flow in a helical duct with rectangular cross section and finite pitch. *Applied Mathematical Modelling* 2012; 36.10:5059–5067.

[157] Cookson AN, Doorly DJ, & Sherwin SJ. Mixing through stirring of steady flow in small amplitude helical tubes. *Annals of Biomedical Engineering* 2009; 37:710–721.

[158] Finlay WH, Guo Y, & Olsen D. Inferring secondary flows from smoke or dye flow visualization: Two case studies. *Physics of Fluids A* 1992; 5.

[159] Boiron O, Deplano V, & Pelissier R. Experimental and numerical studies on the starting effect on the secondary flow in a bend. *Journal of Fluid Mechanics* 2007; 574.

[160] Timité B, Castelain C, & Peerhossaini H. Pulsatile viscous flow in a curved pipe: Effects of pulsation on the development of secondary flow. *International Journal of Heat and Fluid Flow* 2010; 31.

[161] Krishna CV, Gundiah N, & Arakeri JH. Separations and secondary structures due to unsteady flow in a curved pipe. *Journal of Fluid Mechanics* 2017; 815.

[162] Liou TM. Flow visualization and LDV measurement of fully developed laminar flow in helically coiled tubes. *Experiments in Fluids* 1992; 13.

[163] Bolinder CJ & Sundén B. Flow visualization and LDV measurements of laminar flow in a helical square duct with finite pitch. *Experimental Thermal and Fluid Science* 1995; 11.

[164] Pielhop K, Schmidt C, Zholtovski S, Klaas M, & Schröder W. Experimental investigation of the fluid–structure interaction in an elastic 180° curved vessel at laminar oscillating flow. *Experiments in Fluids* 2014; 55.

[165] Najjari MR & Plesniak MW. Evolution of vortical structures in a curved artery model with non-Newtonian blood-analog fluid under pulsatile inflow conditions. *Experiments in Fluids* 2016; 57.

[166] Najjari MR & Plesniak MW. Secondary flow vortical structures in a 180 elastic curved vessel with torsion under steady and pulsatile inflow conditions. *Physical Review Fluids* 2018; 3:013101.

[167] Najjari MR, Cox C, & Plesniak MW. Formation and interaction of multiple secondary flow vortical structures in a curved pipe: Transient and oscillatory flows. *Journal of Fluid Mechanics* 2019; 876.

[168] Cox C, Najjari MR, & Plesniak MW. Three-dimensional vortical structures and wall shear stress in a curved artery model. *Physics of Fluids* 2019; 31.12:121903.

[169] Brücker C. A time-recording DPIV-study of the swirl-switching effect in a 90° bend flow. Proceedings 8th International Symposium on Flow Visualization. 1998.

[170] Poelma C, Mari JM, Foin N, et al. 3D Flow reconstruction using ultrasound PIV. *Experiments in Fluids* 2011; 50.

[171] Ghanbarzadeh-Dagheyan A, van de Velde L, Reijnen M, Versluis M, & Groot Jebbink E. Comparing Flow in Helical and Straight Stents Using 2D Ultrasound Particle Image Velocimetry. Medical Imaging 2023. Progress in Biomedical Optics and Imaging - Proceedings of SPIE. 2023.

[172] Coutinho G, Moita A, Ribeiro A, Moreira A, & Rossi M. On the characterization of bias errors in defocusing-based 3D particle tracking velocimetry for microfluidics. *Experiments in Fluids* 2023; 64.

[173] Poelma C. Ultrasound Imaging Velocimetry: a review. *Experiments in Fluids* 2017; 58.

[174] Voorneveld J, Saaid H, Schinkel C, et al. 4-D Echo-Particle Image Velocimetry in a Left Ventricular Phantom. *Ultrasound in Medicine and Biology* 2020; 46.

[175] Barnkob R & Rossi M. General defocusing particle tracking: fundamentals and uncertainty assessment. *Experiments in Fluids* 2020; 61.

[176] Rossi M & Marin A. Single-Camera 3D PTV Methods for Evaporation-Driven Liquid Flows in Sessile Droplets. Droplet Interactions and Spray Processes. Cham: Springer International Publishing, 2020:225–236.

[177] Adrian RJ. Twenty years of particle image velocimetry. *Experiments in Fluids* 2005; 39.

[178] Raffel M, Willert CE, Scarano F, Kähler CJ, Wereley ST, & Kompenhans J. Particle Image Velocimetry: A Practical Guide. Springer Cham, 2018.

[179] Etminan A, Muzychka YS, Pope K, & Nyantekyi-Kwakye B. Flow visualization: state-of-the-art development of micro-particle image velocimetry. *Measurement Science and Technology* 2022; 33.

[180] Rohacs D, Yasar O, Kale U, et al. Past and current components-based detailing of particle image velocimetry: A comprehensive review. *Heliyon* 2023; 9.

[181] Hinsch KD. Holographic particle image velocimetry. *Measurement Science and Technology* 2002; 13.

[182] Soria J & Atkinson C. Towards 3C-3D digital holographic fluid velocity vector field measurement - Tomographic digital holographic PIV (Tomo-HPIV). *Measurement Science and Technology* 2008; 19.

[183] Elsinga GE, Scarano F, Wieneke B, & Oudheusden BWV. Tomographic particle image velocimetry. *Experiments in Fluids* 2006; 41.

[184] Pietrasanta L, Zheng S, Marinis DD, Hasler D, & Obrist D. Characterization of Turbulent Flow Behind a Transcatheter Aortic Valve in Different Implantation Positions. *Frontiers in Cardiovascular Medicine* 2022; 8.

[185] Hasler D & Obrist D. Three-dimensional flow structures past a bioprosthetic valve in an in-vitro model of the aortic root. *PLoS ONE* 2018; 13.

[186] Brücker C, Hess D, & Kitzhofer J. Single-view volumetric PIV via high-resolution scanning, isotropic voxel restructuring and 3D least-squares matching (3D-LSM). *Measurement Science and Technology* 2013; 24.

[187] Brücker C. Digital-Particle-Image-Velocimetry (DPIV) in a scanning light-sheet: 3D starting flow around a short cylinder. *Experiments in Fluids* 1995; 19.

[188] Discetti S & Coletti F. Volumetric velocimetry for fluid flows. *Measurement Science and Technology* 2018; 29.

[189] David L, Jardin T, Braud P, & Farcy A. Time-resolved scanning tomography PIV measurements around a flapping wing. *Experiments in Fluids* 2012; 52.

[190] Song CI, Pogson JM, Andresen NS, & Ward BK. MRI With Gadolinium as a Measure of Blood-Labyrinth Barrier Integrity in Patients With Inner Ear Symptoms: A Scoping Review. *Frontiers in Neurology* 2021; 12:662264.

[191] Alastruey J, Siggers JH, Peiffer V, Doorly DJ, & Sherwin SJ. Reducing the data: Analysis of the role of vascular geometry on blood flow patterns in curved vessels. *Physics of Fluids* 2012; 24:031902.

[192] Morbiducci U, Ponzini R, Rizzo G, et al. Mechanistic insight into the physiological relevance of helical blood flow in the human aorta: An in vivo study. *Biomechanics and Modeling in Mechanobiology* 2011; 10:339–355.

[193] Liu X, Sun A, Fan Y, & Deng X. Physiological Significance of Helical Flow in the Arterial System and its Potential Clinical Applications. *Annals of Biomedical Engineering* 2015; 43.

[194] Rask-Andersen H, Liu W, Erixon E, et al. Human cochlea: anatomical characteristics and their relevance for cochlear implantation. *The Anatomical Record: Advances in Integrative Anatomy and Evolutionary Biology* 2012; 295.11:1791–1811.

[195] Aebischer P, Caversaccio M, & Wimmer W. Fabrication of human anatomy-based scala tympani models with a hydrophilic coating for cochlear implant insertion experiments. *Hearing research* 2021; 404:108205.

[196] Reynolds O. XXIX. An experimental investigation of the circumstances which determine whether the motion of water shall be direct or sinuous, and of the law of resistance in parallel channels. *Philosophical Transactions of the Royal Society of London17* 1883; 174:935–982.

[197] Strouhal V. Ueber eine besondere Art der Tonerregung. *Annalen der Physik und Chemie* 1879; 241:216–251.

[198] Pantokratoras A. Steady laminar flow in a 90° bend. *Advances in Mechanical Engineering* 2016; 8.9:1–9.

[199] Cairelli AG, Chow RWY, Vermot J, & Yap CH. Fluid mechanics of the zebrafish embryonic heart trabeculation. *PLOS Computational Biology* 2022; 18.6:1–17.

[200] Harte N, Obrist D, Caversaccio M, Lajoinie GPR, & Wimmer W. Transverse flow under oscillating stimulation in helical square ducts with cochlea-like geometrical curvature and torsion. 2023.

[201] Felix H, Fraissinette AD, Johnsson LG, & Gleeson MJ. Morphological features of human Reissner's membrane. *Acta oto-laryngologica* 1993; 113.3:321–325.

[202] Kundu PK, Cohen IM, & Dowling DR. Chapter 3 - Kinematics. Fluid Mechanics. Ed. by Kundu PK, Cohen IM, & Dowling DR. Sixth Edition. Boston: Academic Press, 2016:77–108.

[203] Kamla Y, Ameur H, Karas A, & Arab MI. Performance of new designed anchor impellers in stirred tanks. *Chemical Papers* 2020; 74.

[204] Shepherd SJ, Issadore D, & Mitchell MJ. Microfluidic formulation of nanoparticles for biomedical applications. *Biomaterials* 2021; 274.

[205] Lopes C, Cristóvão J, Silvério V, Lino PR, & Fonte P. Microfluidic production of mRNA-loaded lipid nanoparticles for vaccine applications. *Expert Opinion on Drug Delivery* 2022; 19.

[206] Torotwa I & Ji C. A study of the mixing performance of different impeller designs in stirred vessels using computational fluid dynamics. *Designs* 2018; 2.

[207] Rijsbergen MV & Slot J. Bubble-induced sheet cavitation inception on an isolated roughness element. Journal of Physics: Conference Series. Vol. 656. 2015.

[208] Verschoof RA, Veen RCVD, Sun C, & Lohse D. Bubble Drag Reduction Requires Large Bubbles. *Physical Review Letters* 2016; 117.

[209] Groot Jebbink E, Engelhard S, Lajoinie G, de Vries JPP, Versluis M, & Reijnen MM. Influence of Iliac Stenotic Lesions on Blood Flow Patterns Near a Covered Endovascular Reconstruction of the Aortic Bifurcation (CERAB) Stent Configuration. *Journal of Endovascular Therapy* 2017; 24.

[210] Groot Jebbink E. Aortoiliac stenting, how blood flow and stents interact. PhD thesis. University of Twente, 2017.

[211] Engelhard S, van Helvert M, Voorneveld J, et al. Blood Flow Quantification with High-Frame-Rate, Contrast-Enhanced Ultrasound Velocimetry in Stented Aortoiliac Arteries: In Vivo Feasibility. *Ultrasound in Medicine and Biology* 2022; 48.

[212] Settles GS & Hargather MJ. A review of recent developments in schlieren and shadowgraph techniques. *Measurement Science and Technology* 2017; 28.4.

[213] Versluis M. High-speed imaging in fluids. *Experiments in Fluids* 2013; 54.

[214] Hori T & Sakakibara J. High-speed scanning stereoscopic PIV for 3D vorticity measurement in liquids. *Measurement Science and Technology* 2004; 15.

[215] Talapatra S & Katz J. Coherent structures in the inner part of a rough-wall channel flow resolved using holographic PIV. *Journal of Fluid Mechanics* 2012; 711.

[216] Sheng J, Malkiel E, & Katz J. Using digital holographic microscopy for simultaneous measurements of 3D near wall velocity and wall shear stress in a turbulent boundary layer. *Experiments in Fluids* 2008; 45.

[217] Kim H, Groe S, Elsinga GE, & Westerweel J. Full 3D-3C velocity measurement inside a liquid immersion droplet. *Experiments in Fluids* 2011; 51.

[218] Kim H, Westerweel J, & Elsinga GE. Comparison of Tomo-PIV and 3D-PTV for microfluidic flows. *Measurement Science and Technology* 2012; 24.

[219] Zhou G, Bintz L, Anderson DZ, & Bright KE. A life-sized physical model of the human cochlea with optical holographic readout. *Journal of the Acoustical Society of America* 1993; 93.

[220] Gamm UA, Huang BK, Syed MA, Zhang X, M.D. VB, & M.D. MAC. Quantifying hyperoxia-mediated damage to mammalian respiratory cilia-driven fluid flow using particle tracking velocimetry optical coherence tomography. *Journal of Biomedical Optics* 2015; 20.8:080505.

[221] Huang BK, Gamm UA, Bhandari V, Khokha MK, & Choma MA. Three-dimensional, three-vector-component velocimetry of cilia-driven fluid flow using correlation-based approaches in optical coherence tomography. *Biomed. Opt. Express* 2015; 6.9:3515–3538.

[222] Jonas S, Bhattacharya D, Khokha MK, & Choma MA. Microfluidic characterization of cilia-driven fluid flow using optical coherence tomography-based particle tracking velocimetry. *Biomedical Optics Express* 2011; 2.

[223] Boselli F, Jullien J, Lauga E, & Goldstein RE. Fluid Mechanics of Mosaic Ciliated Tissues. *Physical Review Letters* 2021; 127.

[224] Spurway J, Logan P, & Pak S. The development, structure and blood flow within the umbilical cord with particular reference to the venous system. *Australasian Journal of Ultrasound in Medicine* 2012; 15.

[225] Predanic M & Perni SC. Antenatal assessment of discordant umbilical arteries in singleton pregnancies. *Croatian Medical Journal* 2006; 47.

[226] Murray KD. Dimensions of the Circle of Willis and Dynamic Studies Using Electrical Analogy. *Journal of neurosurgery* 1964; 21.

[227] Harte NC, Obrist D, Caversaccio MD, Lajoinie GP, & Wimmer W. Wall Shear Stress and Pressure Fluctuations under Oscillating Stimulation in Helical Square Ducts with Cochlea-like Geometrical Curvature and Torsion. 2023 45th Annual International Conference of the IEEE Engineering in Medicine & Biology Society (EMBC). Sydney, Australia: IEEE, 2023:1–7.

[228] Alblas D, Brune C, Yeung KK, & Wolterink JM. Going Off-Grid: Continuous Implicit Neural Representations for 3D Vascular Modeling. Statistical Atlases and Computational Models of the Heart. Regular and CMRxMotion Challenge Papers. Cham: Springer Nature Switzerland, 2022:79–90.

[229] Brindise MC, Busse MM, & Vlachos PP. Density- and viscosity-matched Newtonian and non-Newtonian blood-analog solutions with PDMS refractive index. *Experiments in Fluids* 2018; 59.

[230] Halonen S, Kangas T, Haataja M, & Lassi U. Urea-Water-Solution Properties: Density, Viscosity, and Surface Tension in an Under-Saturated Solution. *Emission Control Science and Technology* 2017; 3.

[231] Thielicke W & Sonntag R. Particle Image Velocimetry for MATLAB: Accuracy and enhanced algorithms in PIVlab. *Journal of Open Research Software* 2021; 9.

[232] Thielicke W & Stamhuis EJ. PIVlab – Towards User-friendly, Affordable and Accurate Digital Particle Image Velocimetry in MATLAB. *Journal of Open Research Software* 2014; 2.

[233] Antiga L, Piccinelli M, Botti L, Ene-Iordache B, Remuzzi A, & Steinman DA. An image-based modeling framework for patient-specific computational hemodynamics. *Medical and Biological Engineering and Computing* 2008; 46.

[234] Salt AN & DeMott JE. Longitudinal endolymph movements and endocochlear potential changes induced by stimulation at infrasonic frequencies. *The Journal of the Acoustical Society of America* 1999; 106.

[235] Salt AN & Hullar TE. Responses of the ear to low frequency sounds, infrasound and wind turbines. *Hearing Research* 2010; 268.

[236] Renewed proliferation in adult mouse cochlea and regeneration of hair cells. *Nature Communications* 2019; 10.

[237] Taylor R & Forge A. Mammalian Hair Cell Regeneration. Hair Cell Regeneration. Ed. by Warchol ME, Stone JS, Coffin AB, Popper AN, & Fay RR. Cham: Springer International Publishing, 2023:73–104.

LIST OF PUBLICATIONS

Journal articles

Harte N.C., Obrist D., Caversaccio M.D., Lajoinie G.P.R. and Wimmer W. Transverse flow under oscillating stimulation in helical square ducts with cochlea-like geometrical curvature and torsion, *submitted*.

Harte N.C., Obrist D., Caversaccio M.D., Lajoinie G.P.R. and Wimmer W. Wall shear stress and pressure fluctuations under oscillating stimulation in helical square ducts with cochlea-like geometrical curvature and torsion. *45th Annual International Conference of the IEEE Engineering in Medicine & Biology Society (EMBC)*, 2023, Sydney, Australia. doi: 10.1109/EMBC40787.2023.10340844.

Harte N.C., Obrist D., Versluis M., Groot Jebbink E., Caversaccio M.D., Wimmer W. and Lajoinie G.P.R. Second order and transverse flow visualization through 3D PIV in complex millimetric ducts. *(manuscript in preparation).*

Conference presentations

Harte N.C., Obrist D., Caversaccio M.D., and Wimmer W. Secondary flow in helical square ducts with cochlea-like curvature and torsion. *European Congress on Computational Methods in Applied Sciences and Engineering (ECCOMAS) 2022*, Oslo, Norway, 2022, *(talk)*

Harte N.C., Obrist D., Lajoinie G.P.R., Versluis M., Caversaccio M.D., and Wimmer W. Transverse flow in helical square ducts with cochlea-like curvature and torsion. *Complex Motion in Fluids Summer School*, Boekelo, The Netherlands, 2022, *(talk)*

Harte N.C., Lajoinie G.P.R., Versluis M., Caversaccio M.D., Obrist D., and Wimmer W. Transverse flows in models of the cochlear duct validated by 3D micro particle image velocimetry. *18th International Symposium on Computer Methods in Biomechanics and Biomedical Engineering (CMBBE)*, Paris, France, 2023, *(talk)*

Harte N.C., Obrist D., Lajoinie G.P.R., Caversaccio M.D., and Wimmer W. Wall shear stress and pressure fluctuations under oscillating stimulation in helical square ducts with cochlea-like geometrical curvature and torsion. *IEEE Engineering in Medicine and Biology Society (EMBC) 2023*, Sydney, Australia, 2023, *(talk)*

Harte N.C., Obrist D., Versluis M., Caversaccio M.D., Lajoinie G.P.R., and Wimmer W. Transverse flow in helical square ducts with cochlea-like curvature and torsion. *HEARING: High-resolution structural and functional EAR imagING*, Monte Verità, Switzerland, 2023, *(poster)*

DECLARATION OF ORIGINALITY

Last name, first name: Harte, Noëlle Claudia

Matriculation number: 13-117-510

I hereby declare that this thesis represents my original work and that I have used no other sources except as noted by citations.

All data, tables, figures and text citations which have been reproduced from any other source, including the internet, have been explicitly acknowledged as such.

I am aware that in case of non-compliance, the Senate is entitled to withdraw the doctorate degree awarded to me on the basis of the present thesis, in accordance with the "Statut der Universität Bern (Universitätsstatut; UniSt)", Art. 69, of 7 June 2011.

Bern, November 28, 2023

Noëlle Claudia Harte